A FLUORESCENCE STUDY OF SINGLE TRAPPED YTTERBIUM IONS FOR QUANTUM INFORMATION APPLICATIONS.

by

Sara Ejtemaee

THESIS SUBMITTED IN PARTIAL FULFILLMENT
OF THE REQUIREMENTS FOR THE DEGREE OF
MASTER OF SCIENCE
IN THE DEPARTMENT
OF
PHYSICS

SIMON FRASER UNIVERSITY
Fall 2010

APPROVAL

Name:	Sara Ejtemaee
Degree:	Master of Science
Title of thesis:	A fluorescence study of single trapped Ytterbium ions for quantum information applications.
Examining Committee:	Dr.George Kirczenow , Professor (Chair)

Dr. Paul. C. Haljan, Assistant Professor,
Senior Supervisor

Dr. Malcolm Kennett, Assistant Professor,
Supervisor

Dr. Jeffrey McGuirk, Assistant Professor,
Supervisor

Dr. Michael Thewalt, Professor,
Internal Examiner

Date Approved: 13 Aug 2010

SFU SIMON FRASER UNIVERSITY
LIBRARY

Declaration of Partial Copyright Licence

The author, whose copyright is declared on the title page of this work, has granted to Simon Fraser University the right to lend this thesis, project or extended essay to users of the Simon Fraser University Library, and to make partial or single copies only for such users or in response to a request from the library of any other university, or other educational institution, on its own behalf or for one of its users.

The author has further granted permission to Simon Fraser University to keep or make a digital copy for use in its circulating collection (currently available to the public at the "Institutional Repository" link of the SFU Library website <www.lib.sfu.ca> at: <http://ir.lib.sfu.ca/handle/1892/112>) and, without changing the content, to translate the thesis/project or extended essays, if technically possible, to any medium or format for the purpose of preservation of the digital work.

The author has further agreed that permission for multiple copying of this work for scholarly purposes may be granted by either the author or the Dean of Graduate Studies.

It is understood that copying or publication of this work for financial gain shall not be allowed without the author's written permission.

Permission for public performance, or limited permission for private scholarly use, of any multimedia materials forming part of this work, may have been granted by the author. This information may be found on the separately catalogued multimedia material and in the signed Partial Copyright Licence.

While licensing SFU to permit the above uses, the author retains copyright in the thesis, project or extended essays, including the right to change the work for subsequent purposes, including editing and publishing the work in whole or in part, and licensing other parties, as the author may desire.

The original Partial Copyright Licence attesting to these terms, and signed by this author, may be found in the original bound copy of this work, retained in the Simon Fraser University Archive.

Simon Fraser University Library
Burnaby, BC, Canada

Last revision: Spring 09

Abstract

Trapped ions are one of the most promising candidates for quantum information applications. We describe an experimental setup using a linear rf Paul trap for confining $^{171}\mathrm{Yb}^{+}$ ions, in which quantum bits (qubits) are to be hosted in the ground-state hyperfine levels of the ions. In particular, the required lasers and lock setups are described in detail. One of the key requirements for qubit manipulation is achieving high fidelity state-selective detection. A well established means to accomplish this is through the use of laser fluorescence. The fluorescence theory of $^{171}\mathrm{Yb}^{+}$, including the effect of coherent population trapping which can suppress the fluorescence, is documented together with the counter-acting effect of a magnetic field. In addition, the fluorescence theory of $^{174}\mathrm{Yb}^{+}$, which has simpler atomic structure and behavior, is also described for comparison. The resonance fluorescence behaviour of both isotopes is studied experimentally as a function of magnetic field, laser polarization, power and detuning. The experimental results for both isotopes agree with theoretical models, including the effect of coherent population trapping. These results will be used to optimize laser cooling and qubit detection for $^{171}\mathrm{Yb}^{+}$ in future experiments.

To M.Ziyabari

Acknowledgments

I would like to thank all people who have helped and inspired me during my master.

This thesis would not have been possible without the help of my supervisor, Dr. Paul. C. Haljan who has supported me throughout my thesis with his patience and knowledge. He was always accessible and willing to help his students. I attribute the level of my Masters degree to his encouragement and effort. One simply could not wish for a better or friendlier supervisor.

Besides my supervisor, I would like to thank my committee members: Dr. Jeffrey McGuirk and Dr. Malcolm Kennett for their helpful comments and Dr. Mike Thewalt who accepted to read my thesis.

Next I need to thank my colleagues in the lab, Jixin Liang and Ryan Thomas for good companionship in the lab.

I would like to thank one of my physics teachers in high school, Ms. Mahboubeh Ziyabari who spent several hours out of class to teach me physics. It is thanks to her that I first became interested in physics and decided to become a physicist.

I wish to thank my friends, Laleh Samii, Azadeh Akhtari and Alireza Hojjati, for helping me get through the difficult times, and for all the support, entertainment, and caring they provided.

Lastly, and most importantly, I wish to thank my parents and my sister who have been a constant source of love and support throughout my life. They were always there whenever and wherever I needed them. Maman, Baba, Setareh thanks for everything you have done for me. I would not be where I am today without you.

Contents

List of Tables

List of Figures

Chapter 1

Introduction

The basic element of information in a quantum computer is the quantum bit (qubit). Unlike classical bits that are limited to a state of either 0 or 1, qubits can be in an arbitrary superposition of these two states. The quantum superposition principle is often pointed to as the advantage of a quantum computer over its classical counterparts because of the massive parallelism it implies [1]. In this regard, another important feature of qubits is quantum entanglement or quantum non-local connection. Entanglement leads to a correlation between qubits and allows for simultaneous operations on multiple states.

Large-scale quantum computers are believed to provide a speed-up over classical devices for certain information processing applications. Perhaps the most famous example is Shor's algorithm for factoring an n-digit number. Solving Shor's algorithm can be a threat for current encryption schemes, which are based on the inability of classical computers to factorize large numbers in a short amount of time. In addition, quantum computers are naturally adept at efficient modelling of quantum systems which is called "quantum simulation" [2].

A qubit can be any physical quantum two-level system such as the vertical and horizontal polarizations of a single photon or the two quantized spin states of a spin $1/2$ particle. To implement a quantum computer, there are five requirements that a physical system needs to fulfill. These requirements were introduced by David Divincenzo as follows [3]

- Well-defined qubits, scalable to a large number.
- The ability to initialize the qubits to a simple state.

- Long qubit decoherence times, much longer than the gate operation time.
- Universal set of gates.
- Qubit measurement capability.

Laser-cooled, trapped ions are widely considered to be a promising candidate to implement a quantum information processor. Our group, in particular, is working with trapped Ytterbium ions. Trapped $^{171}\mathrm{Yb}^+$ ions currently find application in precision spectroscopy for time and frequency metrology [4, 5, 6, 7], ion-trap quantum information processing [8, 9, 10, 11] and studies of interactions with ultracold atoms [12, 13]. In these applications, efficient fluorescence scattering is required as it forms the basis for the mechanical action of Doppler laser cooling [14] and permits high-fidelity state-selective detection [15, 16]. This thesis focuses on the fluorescence behaviour of single trapped Yb^+ ions, the optimization of which is a key step in the setup of new laboratory for ion trap quantum information technology.

Chapter 2 of the thesis introduces the $^{171}\mathrm{Yb}^+$ ion as a hyperfine qubit and gives a detailed theoretical description of fluorescence theory for two Yb^+ isotopes, $^{171}\mathrm{Yb}^+$ and, for comparison, $^{174}\mathrm{Yb}^+$ with simpler level structure and behaviour. One of the key complications that arises for $^{171}\mathrm{Yb}^+$ is coherent population trapping (CPT) on the main cooling and fluorescence transitions. This effect, which suppresses the fluorescence, is a key theme of this thesis.

Chapter 3, gives a general overview of the different parts of the experimental setup including the linear Paul trap used to confine ions, the imaging system, and lasers used for photo-ionization-loading, Doppler cooling, fluorescence detection and repumping.

Chapter 4 provides greater detail on three of the lasers: the 399 nm diode laser used for photo-ionization, the 369.5 nm frequency-doubled diode laser system used for detection/cooling and the 935 nm diode laser used for repumping. We also describe the lock setups for the 369.5-nm and 935-nm lasers and offline tests of the stability of those locks over hours using a stabilized wavemeter.

Finally, Chapter 5 begins with a description of basic experimental procedure and tests of laser stability with respect to the optical resonances of the ions themselves. We then show measurements of the fluorescence behaviour for both of the isotopes, $^{171}\mathrm{Yb}^+$ and $^{174}\mathrm{Yb}^+$, as a function of magnetic field, laser polarization, detuning and power. As part of our fluorescence studies, we have verified a model presented by Berkeland and Boshier [17] for suppressing the effect of CPT using a magnetic field of sufficient strength.

Although coherent population trapping is certainly a well known phenomenon in atomic physics and the issues we are addressing are well known amongst ion trapping groups, this thesis aims to provide a complete and quantitative experimental study and emphasizes the intuitive theoretical approach of Berkeland and Boshier. Moreover, understanding and avoiding fluorescence suppression due to coherent population trapping is critical to obtain good laser cooling and good qubit detection fidelity using laser fluorescence. We have already used the experience gained from this thesis work to optimize our detection of the $^{171}\mathrm{Yb}^{+}$ qubit and have achieved 97% fidelity [18], which is comparable to previously published results for $^{171}\mathrm{Yb}^{+}$ [11].

Chapter 2

Fluorescence theory

In this chapter we first describe the Ytterbium ion $^{171}\mathrm{Yb}^{+}$ as our qubit candidate in detail. A well-established means to achieve high fidelity state-selective detection of an ion-qubit is through the use of laser fluorescence. Based on this motivation, we describe the steady-state fluorescence theory for the $^{171}\mathrm{Yb}^{+}$ ion and extend the theory already presented by Berkeland and Boshier [17], to include repump effects. We also present approximate theoretical expressions for the fluorescence of the $^{174}\mathrm{Yb}^{+}$ isotope, which is used as a "control" ion with simpler level structure and behaviour to validate $^{171}\mathrm{Yb}^{+}$ experimental results. In Chapter 5, the steady-state fluorescence of both isotopes is measured experimentally and compared to the theory presented here.

2.1 Ytterbium ion

In 1995 Cirac and Zoller first introduced quantum information applications to ion trap systems by proposing a quantum entangling gate scheme [8]. Since the first demonstration of a quantum logic gate [19], trapped ions have evolved into a promising candidate for quantum information applications. There are generally two types of qubits implemented with ions: optical qubits where the two qubit levels are separated by an optical frequency (see for example [20]) and hyperfine qubits where the two qubit levels are stored in the ground-state hyperfine manifold and are separated by a microwave frequency [16]. Ions that are being used for quantum computing applications include Yb^{+}, Ba^{+}, Be^{+}, Ca^{+}, Cd^{+}, Mg^{+} and Sr^{+}. In this thesis, we use Yb^{+} ion as the hyperfine qubit.

Like the other ions, Yb^+ has a single active electron, which ensures the ion has a simple level structure. This allows, in particular, a relatively simple closed transition for laser cooling. Ytterbium has seven stable isotopes. The stable isotopes with their natural abundances are shown in Table 2.1 [21].

Isotope	Natural Abundance(%)	Atomic Nuclear Spin	Hyperfine Splitting [GHz]
^{168}Yb	0.13	0	-
^{170}Yb	3.04	0	-
^{171}Yb	14.28	1/2	12.6
^{172}Yb	21.83	0	-
^{173}Yb	16.13	5/2	10.5
^{174}Yb	31.83	0	-
^{176}Yb	12.76	0	-

Table 2.1: Ytterbium isotopes.

Of the isotopes listed in Table 2.1, only the odd numbered isotopes, $^{171}\mathrm{Yb}^+$ and $^{173}\mathrm{Yb}^+$ can be used as hyperfine qubits. The even-numbered isotopes of Ytterbium do not have any nuclear spin; hence, the interaction between nuclear spin (I) and electronic angular momentum ($\vec{J}$), which causes hyperfine splitting, vanishes. Of the two odd isotopes, $^{173}\mathrm{Yb}^+$ has a high nuclear spin ($I = 5/2$) which complicates the level structure and has disadvantages for quantum information applications; hence, $^{171}\mathrm{Yb}^+$ with a nuclear spin of $I = 1/2$, is used as the qubit due to its simple hyperfine structure. It is worth noting that the abundance of the ^{171}Yb isotope is 14.3%, which makes the loading process easy and fast.

Partial energy levels of $^{171}\mathrm{Yb}^+$ are shown in Fig 2.1. The ground-state $^2\mathrm{S}_{1/2}$ hyperfine levels $|F = 0, m_F = 0\rangle \equiv |\downarrow\rangle$ and $|F = 1, m_F = 0\rangle \equiv |\uparrow\rangle$ are the two qubit levels, separated by 12.64 GHz. These two qubit states, in addition to having long lifetimes, have a transition that is insensitive to magnetic field noise to first order at zero magnetic field. The residual second order Zeeman shift is $\delta = (310.8Hz/G^2) \cdot B^2$ for magnetic field, B, expressed in Gauss [22].

The primary transition for Doppler cooling and fluorescence detection is $^2S_{1/2}(F = 1) - {}^2P_{1/2}(F = 0)$ at 369.5 nm. High power diode or Ti-Sapphire lasers are available at a wavelength of 739 nm, which can easily be doubled to 369.5 nm. The natural linewidth of the

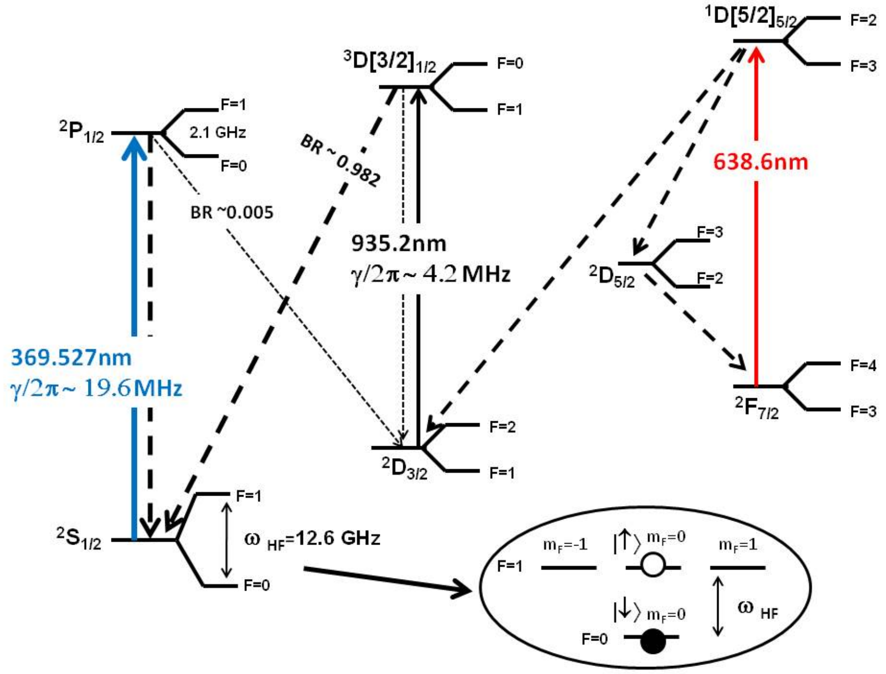

Figure 2.1: Yb^+ atomic structure involved in fluorescence detection and cooling. Hyperfine states for $^{171}Yb^+$ are shown, including $m_F = 0$ qubit states.

transition is 19.60(5) MHz, inferred from previous lifetime measurements [23, 24]. A small leak from the $^2P_{1/2}$ excited-state to the low lying $^2D_{3/2}$ state occurs with a branching ratio of $\alpha = 0.00501(15)$ [11] and requires the use of a repump laser to maintain fluorescence. Clear-out of the $^3D[3/2]_{1/2}$ state is achieved via a 935-nm transition to the $^3D[3/2]_{1/2}$ excited-state. The 935-nm transition has a linewidth of 4.22(6) MHz inferred from previous lifetime measurements [25] and the ion returns to the ground state with a calculated branching ratio $\beta = 0.982$ [26]. We assume the remainder of the branching ratio is back to the $^2D_{3/2}$ state. There is also a low lying and long-lived metastable $^2F_{7/2}$ state that can be populated via collisional processes [27, 28, 29]. An additional repump laser at 638 nm is necessary to depopulate the $^2F_{7/2}$ state to a $^1D[5/2]_{5/2}$ state from which the ion can return to the cooling cycle.

2.2 Fluorescence theory

2.2.1 Coherent population trapping

In this section we study the fluorescence of single trapped ions for the case of two Yb^+ isotopes, $^{174}\mathrm{Yb}^+$ and $^{171}\mathrm{Yb}^+$. Due to the multilevel nature of atomic systems in general, efficient fluorescence can be compromised by optical pumping to dark states. In most cases, this is simply countered through additional laser repump frequencies or by appropriate choice of laser polarizations to ensure a closed fluorescence cycle. However, if two or more lower states share an excited-state, interference effects can arise such that, even though all couplings are present, the fluorescence will be suppressed through coherent population trapping (CPT) [30, 31]. A commonly discussed example of coherent population trapping is a Λ-type three level system (see Fig 2.2) where two laser frequencies are used to couple two different lower states ($|1\rangle$ and $|2\rangle$) to a common upper state ($|3\rangle$) [31]. If the lasers' detunings are matched, the interaction of the atom with the two laser beams optically pumps the atom into a dark state composed of a superposition of two lower states. The dark state is decoupled from the lasers because the transition amplitudes from the two lower states to the upper state interfere destructively.

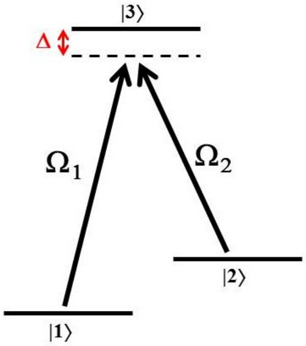

Figure 2.2: A Λ-type three-level system in which coherent population trapping can occur.

Coherent population trapping and its related physics [32] can be exploited for useful applications including novel cooling schemes such as velocity selective coherent population trapping (VSCPT) [33] and electromagnetically-induced-transparency (EIT) cooling [34]. However, coherent population trapping can also arise in a Zeeman degenerate transition driven by a single laser field and leads to a detrimental suppression of fluorescence. In this case, the Λ-systems correspond to polarization couplings between different Zeeman levels. One of the particular cases of Zeeman degenerate transitions that exhibit coherent population trapping is a transition between two states with equal integer angular momentums. The second case is a transition with higher multiplicity in the ground-state where the angular momentum can be either half-integer or integer [17]. The second case occurs for the hyperfine $^2S_{1/2}(F=1) \rightarrow ^2 P_{1/2}(F=0)$ cooling transition of ^{171}Yb$^+$ (see Fig 2.2) and also for its repump transition $^2D_{3/2}(F=1) \rightarrow ^3 D[3/2]_{1/2}(F=0)$. In the case of ^{174}Yb$^+$, CPT is absent on the main UV transition $^2S_{1/2} \rightarrow ^2 P_{1/2}$ but arises for the repump transition $^2D_{3/2} \rightarrow ^3 D[3/2]_{1/2}$.

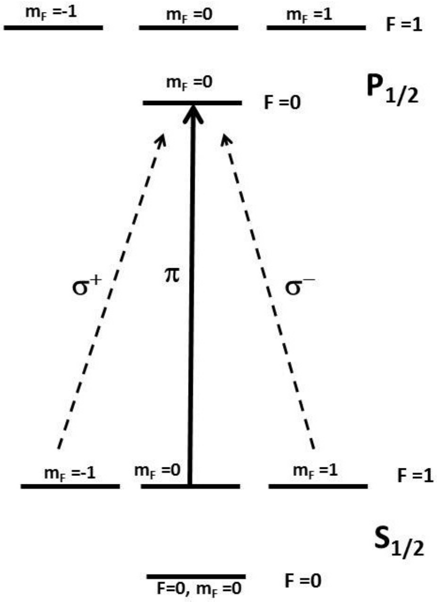

Figure 2.3: The main UV transition of ^{171}Yb$^+$ which exhibits coherent population trapping.

Another way of interpreting CPT in these cases is in terms of optical pumping to polarization dark states in the absence of a well-defined quantization axis [35]. For example, consider a linearly polarized laser that is incident on a ^{171}Yb$^+$ ion and tuned close to the $^2S_{1/2}(F=1) - ^2 P_{1/2}(F=0)$ resonance. If we insert a magnetic field along the $\hat{z}$-axis, it will define a quantization axis. The $\vec{E}$ field of the incident laser should then make an angle with respect to the quantization axis to ensure that all Zeeman states are coupled. If instead the laser's $\vec{E}$ lies along the $\hat{z}$ direction, the presence of π polarization and absence of circular polarizations will optically pump the ion out of the $|F=1,m_F=0\rangle$ sublevel and into the $|F=1,m_F=\pm1\rangle$ polarization dark states that have no coupling to the excited-state. Now, in the limit of no magnetic field, the lack of a well-defined quantization axis implies that the ion's Zeeman states can always be rotated into a basis where the $\hat{z}$-axis overlaps with the $\vec{E}$ field of the laser. Physically this means that the atom's ground-state spin will be optically pumped to the two polarization dark states in this new rotated basis. The dark states are, in general, a superposition of the Zeeman levels in the original $\hat{z}$-axis basis. Although this discussion has focused on zero magnetic field, the CPT effect persists at finite magnetic fields for sufficiently strong laser powers because the dressed atom will adiabatically follow the Larmor precession of ground-state spin, and remain dark.

Berkeland and Boshier [17] have provided a detailed theory of dark state formation in Zeeman degenerate systems and have described the two common experimental methods for dark-state destabilization. The first method involves modulating the polarization of the laser at a rate sufficiently fast that the ground-state populations and coherences cannot follow, effectively projecting out of the dark state [35, 36]. The second method uses a magnetic field to rotate the ground-state spin-polarization out of the dark state by magnetic field precession [37, 38, 39]. The laser modulation scheme has the advantage that it works near zero magnetic field where, for example, clock-state hyperfine qubits [16] of the type in $^{171}\mathrm{Yb}^+$ are first-order insensitive to field fluctuations. The advantage of the magnetic field method is that it is simple to implement. In this thesis, we study in detail the magnetic field method of dark-state destabilization for single, trapped Yb^+ ions.

2.2.2 Liouville equation

In this section, we derive the internal state populations and coherences for Yb^+ by solving for the steady-state density matrix using the quantum Liouville equation [40]. The ion's UV fluorescence rate $\eta\gamma\mathcal{P}_p$ that we measure experimentally is proportional to the photon collection efficiency η of our imaging system, the linewidth γ of the 369.5-nm transition and the total $^2P_{1/2}$ excited-state population $\mathcal{P}_p$.

The time evolution of the density matrix, ρ describing the internal state of the ion governed by Liouville's equation as follows:

$$i\hbar\frac{d\rho_{kl}}{dt} = [H,\rho]_{kl} + i\hbar\langle k|\Gamma|l\rangle \tag{2.1}$$

Diagonal terms in the density matrix, ρ_{kk}, represent the population of the k^{th} state, and each off-diagonal term, ρ_{kl}, is the coherence between the k^{th} and l^{th} states. The total Hamiltonian H includes the interactions of the ion with laser fields and an external magnetic field, while $\langle k|\Gamma|l\rangle$ represents the damping effects. In our case, damping terms are exclusively due to spontaneous emission processes. We ignore the effect of ion motion in the trap and assume a laser spectral-width much narrower than the linewidth.

It is long but straight forward to account for the complete set of levels involved in fluorescence (shown in Fig 2.1); however, the problem can be solved in a piecewise way. Since the leakage rate to the $^2D_{3/2}$ state is weak, the essential steady-state fluorescence behaviour is accounted for by the $^2S_{1/2}-{}^2P_{1/2}$ transition, with only a small correction required for the $^2D_{3/2}$ repump as long as the 935-nm laser parameters are properly optimized. We ignore the small repump correction in first order but consider its effect at the end. Lastly, there is also the low-lying and long-lived metastable $^2F_{7/2}$ state, shown in Fig 2.1, that is not strongly linked to the $^2D_{3/2}$ state because of selection rules but nevertheless can be populated via collisional processes [27, 28, 29]. While an additional repump laser at 638 nm is necessary to depopulate the $^2F_{7/2}$ state, collisional de-excitation events are relatively rare in practice and so we ignore the $^2F_{7/2}$ state in our model of fluorescence.

We start by considering the ^{174}Yb$^+$ since it has no hyperfine structure and continue with the ^{171}Yb$^+$ isotope afterwards.

2.2.3 ^{174}Yb$^+$ fluorescence theory

Figure 2.4 shows the Zeeman-resolved structure of the $^2S_{1/2}(J=1/2)-{}^2P_{1/2}(J=1/2)$ transition for ^{174} Yb$^+$, which is used for the cooling and fluorescence detection. The ^{174} Yb$^+$ ion has no nuclear spin and so no hyperfine structure. Both the ground and excited-states have the same half-integer angular momentum $J=1/2$. While it is possible to optically pump dark if we only provide σ^+ or σ^- polarization, there is no CPT effect for this transition. We represent the four $^2S_{1/2}$ and $^2P_{1/2}$ Zeeman states in the following vector format:

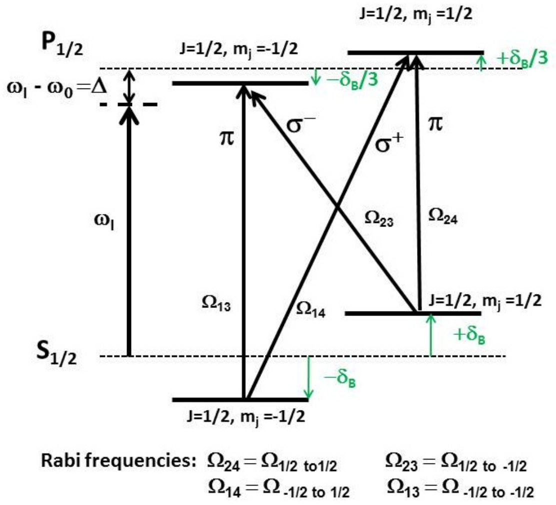

Figure 2.4: Zeeman resolved structure of the main 369.5-nm ${}^2S_{1/2} - {}^2P_{1/2}$ transition for ^{174}Yb$^+$. In the figure, ω_l is the frequency of laser, ω_0 is the frequency of the ${}^2S_{1/2} - {}^2P_{1/2}$ atomic transition and Δ is the laser detuning. The magnetic field splittings are shown in units of δ_B (see text).

$$\left|S_{1/2}, J=1/2, m_J=-1/2\right\rangle = \begin{pmatrix}1\\0\\0\\0\end{pmatrix}, \qquad \left|S_{1/2}, J=1/2, m_J=1/2\right\rangle = \begin{pmatrix}0\\1\\0\\0\end{pmatrix},$$

$$\left|P_{1/2}, J=1/2, m_J=-1/2\right\rangle = \begin{pmatrix}0\\0\\1\\0\end{pmatrix}, \qquad \left|P_{1/2}, J=1/2, m_J=1/2\right\rangle = \begin{pmatrix}0\\0\\0\\1\end{pmatrix}. \tag{2.2}$$

The total Hamiltonian of the ion consists of three parts:

$$\hat{H} = \hat{H}_0 + \hat{H}_B + \hat{V}(t). \tag{2.3}$$

The unperturbed Hamiltonian $\hat{H}_0$ of the ion is

$$\hat{H}_0 = \hbar \begin{bmatrix} 0 & 0 & 0 & 0 \\ 0 & 0 & 0 & 0 \\ 0 & 0 & \omega_0 & 0 \\ 0 & 0 & 0 & \omega_0 \end{bmatrix} \tag{2.4}$$

where ω_0 corresponds to the angular frequency of the $^2S_{1/2}(J = 1/2) -^2 P_{1/2}(J = 1/2)$ transition (see Fig 2.4).

An external magnetic field B shifts the energy of Zeeman sublevels. At low fields, the energy shift is linearly proportional to the magnetic field strength as follows [41]:

$$\Delta E_B(J, m_J) = g_J m_J \cdot \mu_B B = g_J m_J \cdot (\hbar\delta_B) = 1.4\frac{MHz}{G} \cdot B[G] \tag{2.5}$$

where μ_B is the Bohr magneton and $\delta_B = \mu_B B/\hbar$ is the Zeeman frequency-shift. The Lande g-factor, g_J, for a total angular momentum J, orbital angular momentum L, and spin angular momentum S is as follows:

$$g_J = 1 + \frac{J(J+1) + S(S+1) - L(L+1)}{2J(J+1)}. \tag{2.6}$$

Using the above equation, the g-factor is $g_J = 2$ for $^2S_{1/2}(J = 1/2)$ and $g_J = 2/3$ for $^2P_{1/2}(J = 1/2)$; thus, the Hamiltonian H_B describing the magnetic field interaction becomes

$$\hat{H}_B = \hbar \begin{bmatrix} -\delta_B & 0 & 0 & 0 \\ 0 & \delta_B & 0 & 0 \\ 0 & 0 & -\delta_B/3 & 0 \\ 0 & 0 & 0 & \delta_B/3 \end{bmatrix}. \tag{2.7}$$

The last remaining term to be discussed in Eq. (2.3) is the interaction of the ion with the laser field. In general, the Hamiltonian for dipole coupling is:

$$\hat{V}(t) = -e\vec{E}(\vec{r}, t) \cdot \hat{\vec{r}} \tag{2.8}$$

where $e\hat{\vec{r}}$ is the dipole operator and $\vec{E}$, the laser's electric field, is:

$$\vec{E}(\vec{r}, t) = E_0 \hat{\varepsilon} \cos(\vec{k} \cdot \vec{r} - \omega_l \cdot t). \tag{2.9}$$

In the above equation, E_0 is the amplitude of electric field; $\hat{\varepsilon}$ is the unit polarization; and ω_l is the angular frequency of the laser field. The coupling matrix elements of the interaction Hamiltonian between an arbitrary ground-state $|g\rangle$ and excited-state $|e\rangle$ can be written in terms of a Rabi frequency Ω as

$$V = \hbar\Omega\cos(\vec{k}\cdot\vec{r} - \omega_l\cdot t), \tag{2.10}$$

where the laser Rabi frequency is defined by

$$\Omega \equiv \frac{-eE_0}{\hbar}\langle e|\hat{\varepsilon}\cdot\vec{r}|g\rangle = \frac{-\mu_{eg}\cdot E_0}{\hbar}. \tag{2.11}$$

The electric-dipole moment μ_{eg} of the transition depends on the wavefunctions of the ground and excited-states and can be complicated to calculate. However, this is unnecessary as all information can be obtained from the transition frequency ω_0, and the measured linewidth. The remainder of the behaviour is the angular momentum dependence which is easily extracted using the Wigner-Eckart theorem. For $^{174}\mathrm{Yb}^+$, the coupling Rabi frequency between angular momentum states $|J',M'\rangle$ and $|J,M\rangle$ is as follows:

$$\Omega_{J'M'JM} = \frac{-e\cdot E_0}{\hbar}\left\langle\alpha'J'M'\,|\hat{\varepsilon}\cdot\vec{r}|\,\alpha JM\right\rangle \tag{2.12}$$

where α represents all the other quantum properties besides the angular momentum J. Using the Wigner-Eckart theorem, the coupling Rabi frequency can be simplified to

$$\Omega_{J'M'JM} = (-1)^{J-M'}\sqrt{2J'+1}\,\Omega_{JJ'}\sum_q(-1)^q\varepsilon_{-q}\begin{pmatrix} J & 1 & J' \\ M & q & M' \end{pmatrix} \tag{2.13}$$

where the Wigner 3-j symbol in parentheses determines the polarization selection rules and the reduced Rabi frequency $\Omega_{JJ'} = \frac{-e_0\cdot E_0}{\hbar}\langle\alpha'J'\|r\|\alpha J\rangle$ can be rewritten in terms of experimentally measured parameters of wavelength λ, linewidth γ, and intensity I as follows:

$$\Omega_{JJ'} = \sqrt{\frac{s_0(JJ')}{2}}\cdot\gamma, \qquad S_0(JJ') = \frac{I}{I_{sat}(JJ')}, \qquad I_{sat}(JJ') = \frac{\pi hc}{3\lambda^3}\cdot\gamma. \tag{2.14}$$

The Rabi frequency and associated on-resonance saturation parameter S_0 are defined in terms of the bare $^2S_{1/2} - {}^2P_{1/2}$ fine-structure transition to make comparison between $^{174}\mathrm{Yb}^+$ and $^{171}\mathrm{Yb}^+$ explicit. Since the total angular momentum of the ground and excited-states of the studied transition ($^2S_{1/2} - {}^2P_{1/2}$) is fixed for both isotopes, we denote $\Omega_{JJ'}$ by Ω_0 for simplicity from now on.

The Rabi frequencies between the various ground and excited Zeeman states for the $^2S_{1/2} \rightarrow {}^2P_{1/2}$ transition in ^{174}Yb$^+$, are evaluated according to Eq 2.13 and displayed in the Table 2.2.

Ω	M_J	q	$M_{J'}$	3j	$\Omega_{J'M'JM}$
Ω_{24}	1/2	0	1/2	$\sqrt{1/6}$	$\sqrt{1/3}\varepsilon_0\Omega_0$
Ω_{13}	-1/2	0	-1/2	$\sqrt{1/6}$	$-\sqrt{1/3}\varepsilon_0\Omega_0$
Ω_{14}	-1/2	+1	1/2	$-\sqrt{1/3}$	$\sqrt{2/3}\varepsilon_{-1}\Omega_0$
Ω_{23}	1/2	-1	-1/2	$-\sqrt{1/3}$	$-\sqrt{2/3}\varepsilon_{+1}\Omega_0$

Table 2.2: The Zeeman-resolved Rabi frequencies for the main UV transition of ^{174}Yb$^+$.

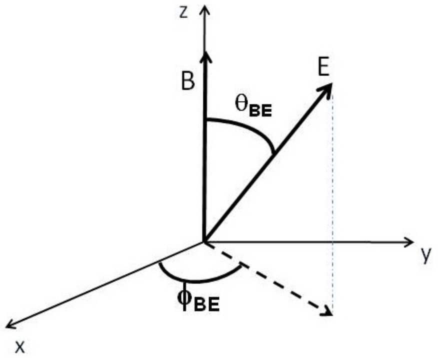

Figure 2.5: External magnetic field and laser's electric field orientation

We consider exclusively the special case of a linearly polarized laser. For a magnetic field along the $\hat{z}$ direction, the spherical components of the linear polarization may be expressed as:

$$\varepsilon_0 = \varepsilon_z = \cos(\theta_{BE}), \tag{2.15}$$

$$\varepsilon_{+1} = -\frac{1}{\sqrt{2}}(\varepsilon_x - i\varepsilon_y) = -\frac{1}{\sqrt{2}}\sin(\theta_{BE})e^{+i\phi_{BE}}, \tag{2.16}$$

$$\varepsilon_{-1} = \frac{1}{\sqrt{2}}(\varepsilon_x + i\varepsilon_y) = \frac{1}{\sqrt{2}}\sin(\theta_{BE})e^{-i\phi_{BE}}, \tag{2.17}$$

where θ_{BE} and ϕ_{BE}, describe the polarization in terms of polar coordinates as illustrated in Fig 2.5. Substituting polarization values into the Rabi frequency equations we get

$$\Omega_{42} = \sqrt{1/3}\Omega_0\cos(\theta_{BE}), \tag{2.18}$$

$$\Omega_{31} = -\sqrt{1/3}\Omega_0\cos(\theta_{BE}), \tag{2.19}$$

$$\Omega_{41} = \sqrt{1/3}\Omega_0 e^{i\phi_{BE}}\sin(\theta_{BE}), \tag{2.20}$$

$$\Omega_{32} = \sqrt{1/3}\Omega_0 e^{-i\phi_{BE}}\sin(\theta_{BE}). \tag{2.21}$$

Now that we have calculated the Rabi frequencies between the ground and excited-states of the ${}^2S_{1/2} - {}^2P_{1/2}$ transition, we can rewrite the laser-atom interaction described in Eq 2.10 as:

$$\hat{V} = \hbar \cdot \cos(\vec{k}\cdot\vec{r} + \omega_l t)\begin{bmatrix} 0 & 0 & \Omega_{13} & \Omega_{14} \\ 0 & 0 & \Omega_{23} & \Omega_{24} \\ \Omega_{31} & \Omega_{32} & 0 & 0 \\ \Omega_{41} & \Omega_{42} & 0 & 0 \end{bmatrix}. \tag{2.22}$$

To simplify the Hamiltonian, we first apply the dipole approximation ($e^{i\vec{k}\cdot\vec{r}} \approx 1$). We then transform to the laser rotating basis and apply the rotating-wave approximation to remove fast-oscillating terms in the density matrix components. The remaining interaction terms are constant, as follows:

$$\hat{V}_{RWA} = \hbar \cdot \begin{bmatrix} 0 & 0 & \Omega_{13}/2 & \Omega_{14}/2 \\ 0 & 0 & \Omega_{23}/2 & \Omega_{24}/2 \\ \Omega_{31}/2 & \Omega_{32}/2 & 0 & 0 \\ \Omega_{41}/2 & \Omega_{42}/2 & 0 & 0 \end{bmatrix}. \tag{2.23}$$

Using Hamiltonians in Eqs.(2.4), (2.7), and (2.23), and assuming that the laser detuning is Δ, we combine the results as follows:

$$\hat{H}_{RWA} = \hbar \cdot \begin{bmatrix} -\delta_B & 0 & \Omega_{13}/2 & \Omega_{14}/2 \\ 0 & \delta_B & \Omega_{23}/2 & \Omega_{24}/2 \\ \Omega_{31}/2 & \Omega_{32}/2 & -\Delta - \delta_B/3 & 0 \\ \Omega_{41}/2 & \Omega_{42}/2 & 0 & -\Delta + \delta_B \end{bmatrix}. \tag{2.24}$$

Finally, the damping terms due to spontaneous emission need to be calculated to be able to solve Liouville's equation (Eq. (2.1)). The damping terms for density matrix elements involving excited-states only are quoted in general form ([42, 43]) as follows:

$$\left\langle \alpha_{e1} J_{e1} M_{e1} | \Gamma_\rho | \alpha_{e2} J_{e2} M_{e2} \right\rangle = -\frac{1}{2}(\gamma_{\alpha_{e1}J_{e1}} + \gamma_{\alpha_{e2}J_{e2}}) \left\langle \alpha_{e1} J_{e1} M_{e1} | \rho | \alpha_{e2} J_{e2} M_{e2} \right\rangle, \tag{2.25}$$

where $\gamma_{\alpha_{ei}J_{ei}}$ is the spontaneous decay rate from a given excited-state. Note that the diagonal elements correspond to the population decay of the associated excited-state. In the specific case of $^{174}\mathrm{Yb}^+$, all of excited-states are simply Zeeman sublevels that have the same decay rate, γ, and so the damping term simplifies to

$$\langle \alpha_e J_e M_e | \Gamma | \alpha_e J_e M_e \rangle = -\gamma \langle \alpha_e J_e M_e | \rho | \alpha_e J_e M_e \rangle. \tag{2.26}$$

The damping terms for the optical-coherence elements of the density matrix, which involve cross terms between ground and excited-states, are in general:

$$\left\langle \alpha_e J_e M_e | \Gamma_\rho | \alpha_g J_g M_g \right\rangle = -\frac{1}{2}(\gamma_{\alpha_e J_e}) \left\langle \alpha_e J_e M_e | \rho | \alpha_g J_g M_g \right\rangle, \tag{2.27}$$

where the decay rate is half of the excited-state population decay rate.

The damping terms for density matrix elements involving the ground-states are as follows:

$$\begin{aligned} \left\langle \alpha_{g1} J_{g1} M_{g1} | \Gamma_\rho | \alpha_{g2} J_{g2} M_{g2} \right\rangle &= \sum_{\alpha_{e1}\alpha_{e2}J_{e1}J_{e2}M_{e1}M_{e2}} (J_{g1} J_{g2} M_{g1} M_{g2} | A | J_{e1} J_{e2} M_{e1} M_{e2}) \\ &\quad \times \langle \alpha_{e2} J_{e2} M_{e2} | \rho | \alpha_{e1} J_{e1} M_{e1} \rangle. \end{aligned} \tag{2.28}$$

This includes both source terms for the ground-state populations arising from the excited-states' population decay and source terms for the off-diagonal coherences between ground states arising from joint relaxation of Zeeman excited-states. The coefficient $\left\langle J_{g1} J_{g2} M_{g1} M_{g2} | A | J_{e1} J_{e2} M_{e1} M_{e2} \right\rangle$ is a generalized Einstein A-coefficient for spontaneous emission that defines the joint relaxation of two states. Rewriting the Einstein A-coefficient in terms of Clebsch-Gordan coefficients, the decay terms for the ground-states can be simplified to:

$$\begin{aligned}\langle \alpha_g J_g M_g' | \Gamma_\rho | \alpha_g J_g M_g \rangle &= (-1)^{M_g'-M_g}(2J_e-1)\gamma_{J_eJ_g}\sum_q \begin{pmatrix} J_g & 1 & J_e \\ M_g' & q & -M_e' \end{pmatrix} \\ &\quad\times \begin{pmatrix} J_g & 1 & J_e \\ M_g & q & -M_e \end{pmatrix} \langle J_e M_e' | \rho | J_e M_e \rangle . \end{aligned} \tag{2.29}$$

Using Eqs. (2.26-2.29) and identifying $\gamma_{\alpha_e J_e}$ as γ, the damping matrix is as follows:

$$\langle k|\Gamma_\rho|l\rangle = \begin{bmatrix} \frac{\gamma}{3}\rho_{33}+\frac{2\gamma}{3}\rho_{44} & \frac{-\gamma}{3}\rho_{34} & \frac{-\gamma}{2}\rho_{13} & \frac{-\gamma}{2}\rho_{14} \\ \frac{-\gamma}{3}\rho_{43} & \frac{2\gamma}{3}\rho_{33}+\frac{\gamma}{3}\rho_{44} & \frac{-\gamma}{2}\rho_{23} & \frac{-\gamma}{2}\rho_{24} \\ \frac{-\gamma}{2}\rho_{31} & \frac{-\gamma}{2}\rho_{32} & -\gamma\rho_{33} & -\gamma\rho_{34} \\ \frac{-\gamma}{2}\rho_{41} & \frac{-\gamma}{2}\rho_{42} & -\gamma\rho_{43} & -\gamma\rho_{44} \end{bmatrix} . \tag{2.30}$$

Finally, we substitute Eq. (2.30) and Eq. (2.24) into Liouville's equation. The equation is easy to solve numerically, but we prefer to have an analytical solution to study the dependences more easily. We use Maple Software to solve for the steady-state both numerically and analytically. Solving for the steady-state solution for $^{174}\mathrm{Yb}^+$ analytically is complicated by the appearance of the decay terms from excited-state to ground-state coherences in the Liouville equation. Numerical simulations, however, indicate that the coherences between ground-state Zeeman levels and those between excited-state levels are zero or close to it over a wide range of parameters, so we set them to zero in our equations and proceed with an approximate solution for the steady-state. This approximation amounts to a rate-equation approach. Analytical solutions for the rate equations, in particular the total $^2P_{1/2}$ population $\mathcal{P}_p$, can then be obtained easily but are still too involved to be convenient. To a very good approximation theoretically, as long as δ_B is not too large ($\delta_B \lesssim \gamma/2$), we find that the excited-state population can be simplified, as follows, to a saturation form analogous to a two level system with an effective linewidth extracted from the $\Delta \to \infty$ limit:

$$\mathcal{P}_p = \sum_{M_J=-1/2}^{1/2} \mathcal{P}_p(M_J) = \frac{1}{2}\cdot\frac{\frac{\Omega_0^2}{6}}{\Delta^2+\left(\frac{\Gamma_{174}}{2}\right)^2}, \tag{2.31}$$

$$\left(\frac{\Gamma_{174}}{2}\right)^2 = \frac{\Omega_0^2}{6}+\frac{\gamma^2}{4}\cdot\frac{\left(1+\frac{16\delta_B^2}{9\gamma^2}\right)\left(1+\frac{64\delta_B^2}{9\gamma^2}\right)}{1+\frac{16\delta_B^2}{9\gamma^2}\cdot(3\cos^2\theta_{BE}+1)} . \tag{2.32}$$

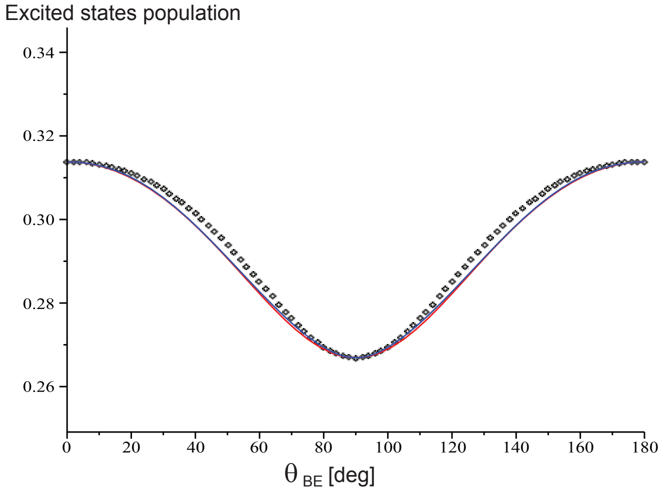

Figure 2.6: Total excited-state population in $^{174}\mathrm{Yb}^+$ versus laser-polarization angle θ_{BE} when $\Delta/2\pi = -8$ MHz, $\delta_B/2\pi = 8.2$ MHz, $\gamma/2\pi = 19.6$ MHz and $S_0 = 10$. Points are the numerical solution. The approximate solution for the steady-states where we set coherences between ground-state Zeeman levels and those between excited-states level to zero is shown as a blue line. The approximate function in Eq. (2.31) is shown in red. The maximum excited-state population occurs at $\theta_{BE} = 0°$, and the minimum occurs at $\theta_{BE} = 90°$.

These equations apply only to the special case of a linearly polarized laser field. The effective linewidth Γ_{174} includes both power- and Zeeman-broadening and approaches the natural linewidth γ in the limit of vanishing magnetic field ($\delta_B \to 0$) and laser power ($\Omega \to 0$).

The excited-state population according to Eq. (2.31) is plotted versus θ_{BE} in Fig 2.6 for detuning $\Delta/2\pi = -8$ MHz, Zeeman shift $\delta_B/2\pi = 8.2$ MHz, linewidth $\gamma/2\pi = 19.6$ MHz, and on-resonance saturation parameter $S_0 = 10$. These values are close to typical experimental values used in Chapter 5. As can be seen, there is no polarization dark state. The peak fluorescence occurs at $\theta_{BE} = 0°$, which is equivalent to a π-polarized laser field, and the minimum fluorescence occurs at $\theta_{BE} = 90°$, which is equivalent to a perpendicular polarization.

To demonstrate that our approximations do not significantly affect the results, we show the full numerical steady-state solution without approximation in Fig 2.6 (black points).

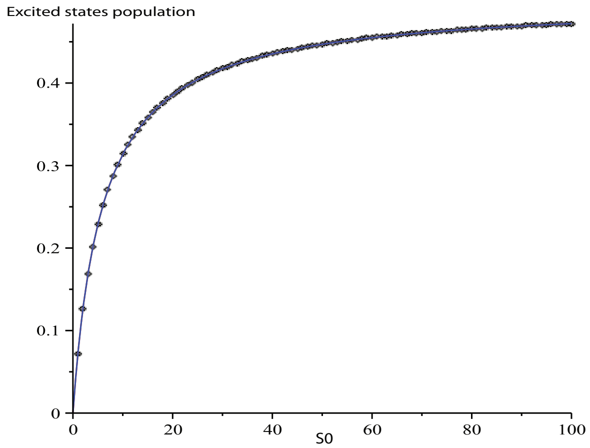

Figure 2.7: Total ${}^2\mathrm{P}_{1/2}$ excited-state population for ${}^{174}\mathrm{Yb}^+$ versus saturation parameter S_0 when $\Delta/2\pi = -8$ MHz, $\delta_B/2\pi = 8.2$ MHz, $\gamma/2\pi = 19.6$ MHz and $\theta_{BE} = 0°$. Points are the full numerical solution without approximation to Eq. (2.31) . The approximate solution for the steady-states where we set coherences between ground-state Zeeman levels and those between excited-states levels to zero is shown in blue and the approximate function according to Eq. (2.31) is shown in red. The population saturates at high powers to 0.5 as for a 2-level system.

Also included in the plot is the approximate analytical solution for the steady-state where we set coherences between ground-state Zeeman levels and those between excited-states levels to zero (blue line). As can be seen, both approximate solutions matches the full numerical one reasonably well, with the largest discrepancy of a few percent near 15°. It is important to note that the discrepancy vanishes at the special points of $\theta_{BE} = 90°$ and $\theta_{BE} = 90°$.

The plot of excited-state population versus saturation parameter is shown in Fig 2.7. The detuning is $\Delta/2\pi = -8$ MHz, Zeeman shift $\delta_B/2\pi = 8.2$ MHz, linewidth $\gamma/2\pi = 19.6$ MHz and polarization angle is optimal, $\theta_{BE} = 0°$. Clearly, increasing the power, or equivalently the saturation parameter, increases the fluorescence until saturation is reached. The maximum achievable population is 0.5, in which case the population is distributed equally between the ground and excited-states. In the absence of Zeeman broadening, the population of the excited-state reaches half its maximum value at $S_0 = 3$. The power required is three times higher than that for a two-level cycling transition because of Zeeman sublevel branching ratios.

2.7.

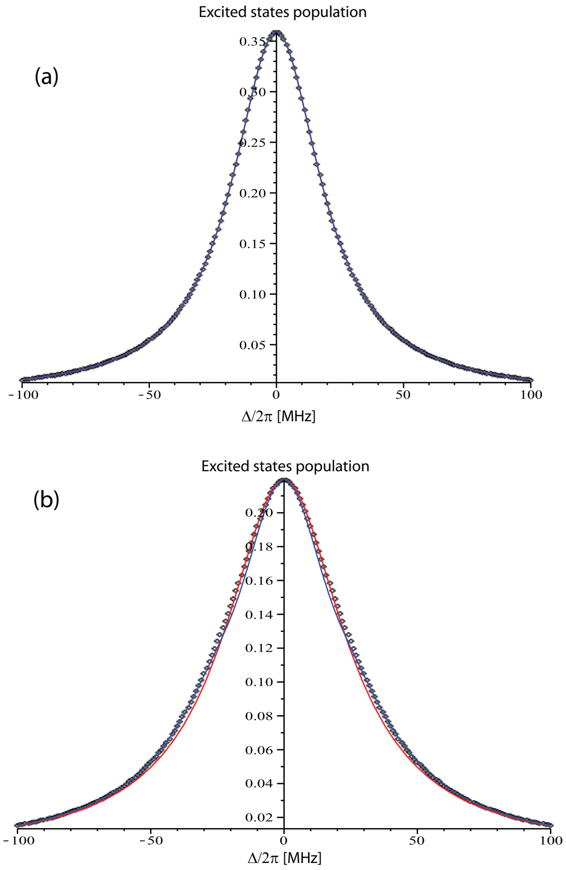

Figure 2.8: $^{174}\mathrm{Yb}^{+}$ excited-states population versus detuning for $\delta_B/2\pi = 8.2$ MHz, $\gamma/2\pi = 19.6$ MHz, $\theta_{BE} = 0^\circ$ and $S_0 = 10$. b) $\delta_B/2\pi = 20$ MHz and $\theta_{BE} = 45^\circ$ while other parameters are the same as (a). Points are the full numerical solution. The approximate analytical solution for the steady-states where we set coherences between ground-state Zeeman levels and those between excited-states levels to zero is shown as a blue line. The further approximated function in Eq. (2.31) is shown as a red line.

Two plots of excited-state population versus laser detuning are shown in Fig 2.8. In Fig 2.8(a), the parameters are a Zeeman shift of $\delta_B/2\pi = 8.2$ MHz, a linewidth of $\gamma/2\pi = 19.6$ MHz, an on-resonance saturation parameter of $S_0 = 10$, and a polarization angle $\theta_{BE} = 0^\circ$.

As in the previous plots, the numerical solution without approximation is plotted as black points. The approximate analytical solution for the steady-state where we set coherences between ground-state Zeeman levels and excited-state levels to zero is shown in blue, and the further approximated function in Eq. (2.31) is shown in red. As can be seen all the solutions match each other. In fact, although Eq. (2.31) is derived as an approximation in general at finite magnetic field, the functional form is correct for the special case of π-polarization ($\theta_{BE} \approx 0°$), as has already been shown in Fig 2.6.

For the experimental results in Chapter 5, we increase the magnetic field up to an equivalent maximum Zeeman splitting of $\delta_B/2\pi = 11.2$ MHz. At these larger magnetic fields, we expect the maximum deviation from the approximate expression in Eq. (2.31). In Fig 2.8(b), the Zeeman shift is set to an even larger value of $\delta_B/2\pi = 20$ MHz, and the polarization angle is set to $\theta_{BE} = 45°$ in order to elicit a worst-case deviation. It can be seen that even at this high magnetic field, Eq. (2.31) still describes the full numerical solution reasonably well.

The excited-state's population in Eq. (2.31), can be generalized to the following form to account for the decay from ${}^2P_{1/2}$ state to the low-lying ${}^2D_{3/2}$ state, as well as the counter-effect of a 935-nm laser repumping via the ${}^3D[3/2]_{1/2}$ state:

$$P_p^{(r)} = \frac{\mathcal{P}_p(\alpha=0)}{1+\xi\mathcal{P}_p(\alpha=0)}, \tag{2.33}$$

where the repump factor ξ is defined as

$$\xi = \frac{\alpha\gamma}{\beta\gamma_{IR}} \frac{1}{\mathcal{P}_{[3/2]}(\beta=0)}. \tag{2.34}$$

The linewidth γ of the 369.5-nm transition, the linewidth γ_{IR} of the 935-nm transition, and branching ratios α and β have already defined (Fig 2.1). $\mathcal{P}_p(\alpha=0)$ is the ${}^2P_{1/2}$ population assuming no leakage to the ${}^2D_{3/2}$ state and is given by Eq. (2.31), while $\mathcal{P}_{[3/2]}(\beta=0)$ is the total population of the ${}^3D[3/2]_{1/2}$ excited-state assuming a closed 935-nm transition. A small value of ξ corresponds to good repumping and a small effect on the UV fluorescence.

The ${}^2D_{3/2} \to {}^3D[3/2]_{1/2}$ repump transition has a larger Zeeman multiplicity in the lower state and is susceptible to coherent population trapping, but calculating the repump factor analytically is challenging since the number of Zeeman levels involved is large, and no obvious approximations present. Therefore, we use numerical simulation to estimate the value of $\mathcal{P}_{[3/2]}(\beta = 0)$ as a function of magnetic field and the 935-nm laser polarization and power, and obtain a repump factor of about $\xi = 0.1$ for the magnetic field range 3.4-8.1 G and near-optimal 935-nm laser parameters considered in this experiment. When the UV transition is saturated ($\mathcal{P}_p = 0.5$), the repump effects are expected to comprise approximately at most a 5% correction to the fluorescence.

2.2.4 ^{171}Yb$^+$ fluorescence theory

The Zeeman-resolved hyperfine structure of the $^2S_{1/2} - ^2P_{1/2}$ transition for ^{171}Yb$^+$ is shown in Fig 2.9. Doppler cooling and fluorescence detection works on the $^2S_{1/2}(F = 1) \rightarrow$ $^2P_{1/2}(F = 0)$ transition, which is closed to the $^2S_{1/2}(F = 0)$ ground-state according to angular momentum selection rules.

The same procedure used to calculate the steady-state fluorescence of ^{174}Yb $^+$ can be applied to ^{171}Yb$^+$. An analytical solution has already been presented elsewhere [17]; however, we show the calculation for completeness and include the effect of the 935-nm repump transition.

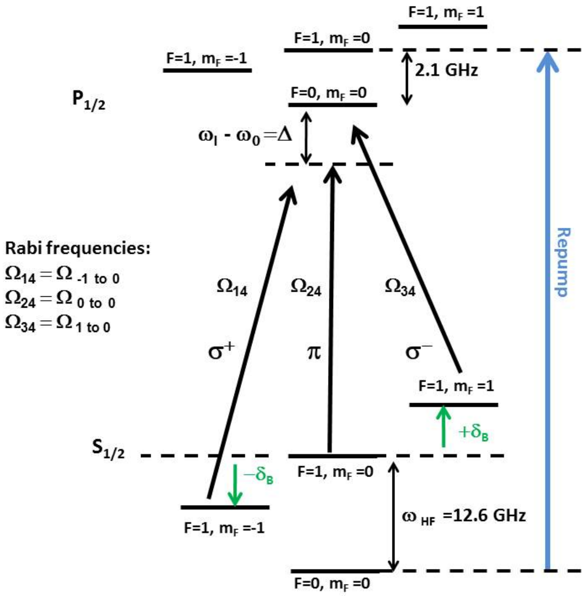

Figure 2.9: Zeeman-resolved hyperfine structure of the main 369.5-nm $^2S_{1/2} - ^2P_{1/2}$ transition for ^{171}Yb$^+$. The UV hyperfine repump transition is also shown.

We represent the four $^2S_{1/2}$ and $^2P_{1/2}$ states in vector format as follows:

$$\left|S_{1/2}, F=1, m_F=-1\right\rangle = \begin{pmatrix}1\\0\\0\\0\end{pmatrix}, \qquad \left|S_{1/2}, F=1, m_F=0\right\rangle = \begin{pmatrix}0\\1\\0\\0\end{pmatrix},$$
$$\left|S_{1/2}, F=1, m_F=1\right\rangle = \begin{pmatrix}0\\0\\1\\0\end{pmatrix}, \qquad \left|P_{1/2}, F=0, m_F=0\right\rangle = \begin{pmatrix}0\\0\\0\\1\end{pmatrix}. \tag{2.35}$$

Similar to $^{174}\mathrm{Yb}^+$, we evaluate the different parts of the total Hamiltonian H, including the magnetic-field and laser interactions. The unperturbed Hamiltonian is:

$$\hat{H}_0 = \hbar \begin{bmatrix} 0 & 0 & 0 & 0 \\ 0 & 0 & 0 & 0 \\ 0 & 0 & 0 & 0 \\ 0 & 0 & 0 & \omega_0 \end{bmatrix} \tag{2.36}$$

where ω_0 corresponds to the frequency of the $^2S_{1/2}(F=1) -^2P_{1/2}(F=0)$ transition. The Zeeman shift of a hyperfine level $|F, m_F\rangle$ is, as follows, in the low magnetic field limit:

$$\Delta E_B(F, m_F) = g_F m_F \cdot \mu_B B = g_F m_F \cdot \hbar\delta_B. \tag{2.37}$$

In the above expression, g_F is the Lande-g factor of an atom with total angular momentum F according to:

$$g_F = g_J \frac{F(F+1)+J(J+1)-I(I+1)}{2F(F+1)} \tag{2.38}$$

where J is the quantum number for angular momentum including spin and orbital contributions, I is the nuclear spin, and F is the total angular momentum quantum number. With g_J from Eq. (2.6) and the value of $g_F = 1$ for the $^2S_{1/2}(F=1)$ sublevels, the Hamiltonian of the ion in the presence of the magnetic field is:

$$\hat{H}_B = \hbar \begin{bmatrix} -\delta_B & 0 & 0 & 0 \\ 0 & 0 & 0 & 0 \\ 0 & 0 & \delta_B & 0 \\ 0 & 0 & 0 & 0 \end{bmatrix} . \tag{2.39}$$

Note that there is no Zeeman shift for the excited-state since it has $m_F = 0$.

Using Eq. (2.11), the Rabi frequency between $|F', M'\rangle$ and $|F, M\rangle$ is defined as

$$\begin{aligned} \Omega_{F'M'FM} &= (-1)^{J'+I-M'_F+1} \sqrt{(2J'+1)(2F'+1)(2F+1)} \begin{Bmatrix} J' & F' & I \\ F & J & 1 \end{Bmatrix} \Omega_0 \\ &\times \sum_q (-1)^q \varepsilon_{-q} \begin{pmatrix} F & 1 & F' \\ M & q & M' \end{pmatrix} . \end{aligned} \tag{2.40}$$

The expression in curly braces, $\begin{Bmatrix} J' & F' & I \\ F & J & 1 \end{Bmatrix}$, is a 6-$j$ symbol that describes recoupling of the angular momenta, and the expression in standard braces, $\begin{pmatrix} F & 1 & F' \\ M & q & M' \end{pmatrix}$, is a 3-$j$ symbol as in the previous section. The Rabi frequencies between ground and excited-states are calculated explicitly in the Table 2.3 as a function of Ω_0, which has previously been defined for the ${}^2S_{1/2}$-${}^2P_{1/2}$ transition of ^{174}Yb$^+$ in Eq. (2.14).

Ω	M_F	q	$M_{F'}$	3-j	$\Omega_{F'M'FM}$
Ω_{14}	-1	+1	0	$\sqrt{1/3}$	$-\sqrt{2/3}\varepsilon_{-1}\Omega_0$
Ω_{24}	0	0	0	$-\sqrt{1/3}$	$-\sqrt{2/3}\varepsilon_0\Omega_0$
Ω_{34}	+1	-1	0	$\sqrt{1/3}$	$-\sqrt{2/3}\varepsilon_{+1}\Omega_0$

Table 2.3: The Rabi frequencies for the main UV transition of ^{171}Yb$^+$.

$$\Omega_{41} = -\sqrt{1/3} \cdot \Omega_0 \cdot e^{i\phi_{BE}} \cdot \sin(\theta_{BE}), \tag{2.41}$$

$$\Omega_{42} = -\sqrt{2/3} \cdot \Omega_0 \cdot \cos(\theta_{BE}), \tag{2.42}$$

$$\Omega_{43} = -\sqrt{1/3} \cdot \Omega_0 \cdot e^{-i\phi_{BE}} \cdot \sin(\theta_{BE}). \tag{2.43}$$

As was done for $^{174}\text{Yb}^+$, we apply the dipole approximation and the rotating wave approximation in the laser rotating basis to obtain the laser-atom interaction Hamiltonian:

$$\hat{V}_{RWA} = \hbar \cdot \begin{bmatrix} -\delta_B & 0 & 0 & \Omega_{14}/2 \\ 0 & 0 & 0 & \Omega_{24}/2 \\ 0 & 0 & \delta_B & \Omega_{34}/2 \\ \Omega_{41}/2 & \Omega_{42}/2 & \Omega_{43}/2 & 0 \end{bmatrix}. \tag{2.44}$$

The damping terms for $^{171}\text{Yb}^+$ are simpler than $^{174}\text{Yb}^+$, since there are no excited-state coherences. Similar to the fine structure case of $^{174}\text{Yb}^+$, the spontaneous damping terms for matrix elements involving only hyperfine excited-states are, in general, as follows [42, 43]:

$$\left\langle \alpha_{e1} F_{e1} M_{e1} | \Gamma_\rho | \alpha_{e2} F_{e2} M_{e2} \right\rangle = -\frac{1}{2}(\gamma_{\alpha_{e1}F_{e1}} + \gamma_{\alpha_{e2}F_{e2}}) \left\langle \alpha_{e1} F_{e1} M_{e1} | \rho | \alpha_{e2} F_{e2} M_{e2} \right\rangle. \tag{2.45}$$

Since there is only one excited-state, this term simplifies to the population decay of the excited-state:

$$\begin{aligned} &\left\langle P_{1/2}, F=0, M_F=0 | \Gamma_\rho | P_{1/2}, F=0, M_F=0 \right\rangle = \\ &\gamma \left\langle P_{1/2}, F=0, M_F=0 | \rho | P_{1/2}, F=0, M_F=0 \right\rangle, \end{aligned} \tag{2.46}$$

where we have identified $\gamma_{\alpha_e F_e}$ as γ. The damping terms for optical coherence elements of the density matrix that involve cross terms between ground and excited-states are:

$$\begin{aligned} &\left\langle P_{1/2}, F=0, M_F=0 | \Gamma_\rho | S_{1/2}, F=1, M_g \right\rangle = \\ &-\frac{\gamma}{2} \left\langle P_{1/2}, F=0, M_F=0 | \rho | S_{1/2}, F=1, M_g \right\rangle. \end{aligned} \tag{2.47}$$

Finally the damping terms for ground-state elements are in general as follows [42, 43]:

$$\begin{aligned} \left\langle \alpha_{g1} F_{g1} M_{g1} | \Gamma_\rho | \alpha_{g2} F_{g2} M_{g2} \right\rangle = &\sum_{\alpha_{e1},\alpha_{e2},F_{e1},F_{e2},M_{e1},M_{e2}} (F_{g1} F_{g2} M_{g1} M_{g2} | A | F_{e1} F_{e2} M_{e1} M_{e2}) \\ &\times \left\langle \alpha_{e2} F_{e2} M_{e2} | \rho | \alpha_{e1} F_{e1} M_{e1} \right\rangle. \end{aligned} \tag{2.48}$$

This is exactly the same as Eq. (2.29) where J is replaced by F.

Using Eqs. (2.45-2.48) for different states, the damping matrix is:

$$\left\langle k | \Gamma_\rho | l \right\rangle = \begin{bmatrix} \frac{\gamma}{3}\rho_{11} & 0 & 0 & \frac{-\gamma}{2}\rho_{14} \\ 0 & \frac{\gamma}{3}\rho_{22} & 0 & \frac{-\gamma}{2}\rho_{24} \\ 0 & 0 & \frac{\gamma}{3}\rho_{33} & \frac{-\gamma}{2}\rho_{34} \\ \frac{-\gamma}{2}\rho_{41} & \frac{-\gamma}{2}\rho_{42} & \frac{-\gamma}{2}\rho_{43} & -\gamma\rho_{44} \end{bmatrix}. \tag{2.49}$$

Note how Eq. (2.48) reduces to the expected three diagonal source-terms for the ground Zeeman states ($+\gamma/3\rho_{kk}$, $k = 1,2,3$). There are no decay source terms for the ground-state coherences since there is a single excited-state and so no excited-state coherences. Substituting Eq. (2.44) and Eq. (2.49) into the Liouville equation (Eq. (2.1)), the steady-state density matrix can be obtained. Unlike $^{174}\mathrm{Yb}^+$, the solution is straightforward, and can be obtained analytically. The steady-state population in the $P_{1/2}(F = 0, m_F = 0)$ excited-state is:

$$\mathcal{P}_p = \frac{3}{4} \cdot \frac{\cos^2\theta_{BE}\sin^2\theta_{BE}}{1+3\cos^2\theta_{BE}} \frac{\frac{\Omega^2}{3}}{\Delta^2 + \left(\frac{\Gamma_{171}}{2}\right)^2}, \tag{2.50}$$

$$\begin{aligned}\left(\frac{\Gamma_{171}}{2}\right)^2 &= \left(\frac{\gamma}{2}\right)^2 + \frac{\Omega_0^2}{3}\cos^2\theta_{BE}\frac{1-3\cos^2\theta_{BE}}{1+3\cos^2\theta_{BE}} \\ &\quad + \frac{\cos^2\theta_{BE}}{1+3\cos^2\theta_{BE}}\left(\frac{\Omega^4}{36\delta_B^2} + 4\delta_B^2\right).\end{aligned} \tag{2.51}$$

This is the same expression with minor modifications to that already presented by Berkeland and Boshier [17]. From the θ_{BE} dependence, it can be seen that $^{171}\mathrm{Yb}^+$ has polarization dark states for $\theta_{BE} = 0^\circ$ and $\theta_{BE} = 90^\circ$, which correspond to situations where at least one of the three polarization couplings vanishes. Since all the couplings have the same Clebsch-Gordon coefficient, the optimum excited-state population at fixed δ_B is achieved when the Rabi frequencies for the three polarization components are all equal. This occurs at a linear laser polarization given by $\theta_{BE} \approx \theta_o \equiv \arccos(\frac{1}{\sqrt{3}}) = 54.7^\circ$. The excited-state population is plotted versus polarization angle in Fig 2.10. Parameters used for the figure are a detuning of $\Delta/2\pi = -8$ MHz, a Zeeman shift of $\delta_B/2\pi = 8.2$ MHz, a linewidth of $\gamma/2\pi = 19.6$ MHz, and a saturation parameter of $S_0 = 10$. Even when all couplings are present, the higher multiplicity in the $F = 1$ ground-state can still lead to suppressed fluorescence through coherent population trapping. The ion is pumped into a ground-state spin coherence that is decoupled from the laser field. A sufficiently strong magnetic field destabilizes the spin coherence by introducing rapid time-dependent phases to the Zeeman levels. As discussed in Ref. [17], the Ω^4/δ_B^2 term in the effective linewidth (Eq. (2.49)) describes the competition between the magnetic-field induced evolution of the dark states and the ability of the dressed atom to follow.

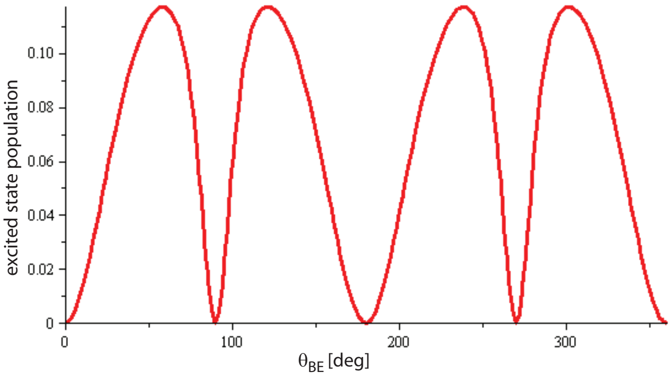

Figure 2.10: ^{171}Yb$^+$ excited-state population versus polarization angle when $\Delta/2\pi = -8$ MHz, $\delta_B/2\pi = 8.2$ MHz, $\gamma/2\pi = 19.6$ MHz and $S_0 = 10$. There is a polarization dark state for $\theta_{BE} = 0°$ and for $\theta_{BE} = 90°$.

The plot of excited-state population versus saturation parameter is shown in Fig 2.11. Parameters assumed for the figure are a detuning of $\Delta/2\pi = -8$ MHz, a Zeeman shift of $\delta_B/2\pi = 8.2$ MHz, a linewidth of $\gamma/2\pi = 19.6$ MHz and a polarization angle at the optimum value $\theta_{BE} = 54.7°$. At low laser powers, the linewidth is roughly constant and the excited-state population grows as $\mathcal{P}_{p0} \sim \Omega^2 \sim S_0$ while at high powers ($\Omega \gg \gamma, \delta_B$)the effective linewidth broadens rapidly and the population drops off as $\mathcal{P}_{p0} \sim 1/\Omega^2 \sim 1/S_0$. With the approximation $\theta = \theta_0$, at fixed δ_B the fluorescence peaks at the following Rabi frequency:

$$\Omega_{pk} \approx \left[\frac{9\delta_B^2}{2}(3\gamma^2 + 12\Delta^2 + 8\delta_B^2)\right]^{1/4} \tag{2.52}$$

where the peak excited-state population is

$$Max(\mathcal{P}_{p0}) \approx \frac{1}{\sqrt{2}} \frac{\delta_B}{\sqrt{3\gamma^2 + 12\Delta^2 + 8\delta_B^2}}. \tag{2.53}$$

In the limit of large magnetic field and laser power, the excited-state fraction can reach 1/4, half of the standard saturation value.

Similarly to ^{174}Yb$^+$, repump effects associated with leakage to the $^2D_{3/2}$ state can be considered for ^{171}Yb$^+$. The repump corrected Eqs. (2.33) and (2.34) also apply to ^{171}Yb$^+$

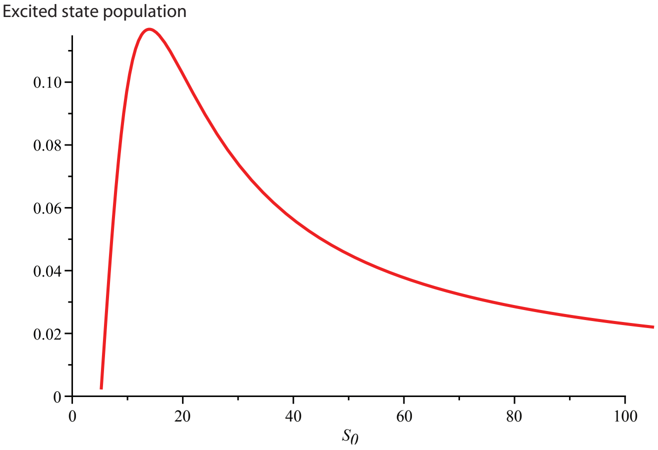

Figure 2.11: ^{171}Yb$^+$ excited-state population versus saturation power when $\Delta/2\pi = -8$ MHz, $\delta_B/2\pi = 8.2$ MHz, $\gamma/2\pi = 19.6$ MHz and $\theta_{BE} = 54.7°$. The CPT effect can be seen for high power, where the fluorescence is suppressed.

with $\mathcal{P}_p$ taken from Eq. (2.50) and $\mathcal{P}_{[3/2]}(\beta = 0)$ is the $^3D[3/2]_{1/2}(F = 0)$ excited-state population assuming a closed 935-nm transition. The 935nm repump transition $^2D_{3/2}(F = 1) \rightarrow {^3D}[3/2]_{1/2}(F = 0)$ itself is susceptible to coherent population trapping. Since the hyperfine structure is the same as the UV transition, Eq (2.50) can also be applied to calculate $\mathcal{P}_{[3/2]}(\beta = 0)$. Over the range of magnetic field 3.4-8.1 G where most of data for this experiment is taken, optimal values of the polarization and power of the 935-nm laser give a value of ξ of about 0.1, which corresponds to a maximum correction to the UV fluorescence of below 2%. For the low side of the magnetic field range the optimization is more sensitive; however, since the peak population in the $^2P_{1/2}(F = 0)$ state is also reduced in low magnetic fields, the values of ξ can be as large as 0.5 but still contribute only 2% correction to the fluorescence. This correction is relatively small; however, the effect of the repump transition is experimentally significant for the ^{174}Yb$^+$ ion, which reaches much higher $^2P_{1/2}$ excitation values, and so we include the correction for both isotopes.

As a final note, the $^2D_{3/2}(F = 2)$ state in ^{171}Yb$^+$ has been ignored since it is approximately closed to the fluorescence cycle and is only populated weakly. The state is cleared out in the experiment using another repump laser frequency but this does not constitute a significant correction to the fluorescence theory for our purposes.

Chapter 3

Experimental Setup

In this chapter, we give an overview of the different parts of the experimental setup used to obtain the data in this thesis. We start with the linear rf Paul trap, that is mounted in a vacuum chamber, and discuss the ion's behaviour in the trap. Then we proceed to the techniques of photo-ionization loading, Doppler laser cooling, and laser fluorescence. At the end of the chapter the imaging system of the experiment is discussed. In Chapter 4, all of the components of the lasers are described in more detail and the basic experimental procedure is left to Chapter 5.

3.1 Trap System

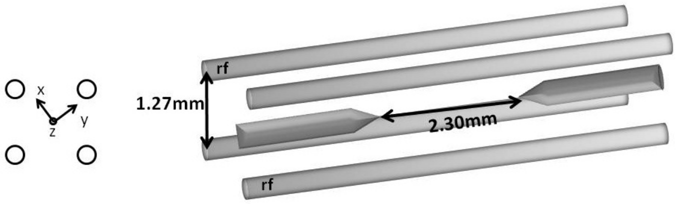

Figure 3.1: Linear rf Paul trap consisting of four rods in a square configuration to confine the ion radially via an rf pseudopotential and two endcap needles to confine the ion axially via dc potentials.

According to Earnshaw's Theorem [44], a collection of point charges cannot be confined in three directions solely by static electric fields. To overcome this problem, there are two common solutions to achieve trapping of ions [45]. The first is a Penning trap which uses a homogeneous static magnetic field and a spatially inhomogeneous static electric field together. The second solution is an rf Paul trap which uses an inhomogeneous electric field oscillating at radio frequency. The concept of the rf Paul trap was invented by Wolfgang Paul, who shared half of the Nobel prize with Hans Dehmelt in 1989 for the development of ion-trap techniques.

We use a linear rf Paul trap [46] consisting of four rods held in a square configuration and two endcap needles parallel to the rods (see Fig 3.1). This style of trap is convenient for quantum computing and quantum simulation where two or more ions are simultaneously confined in the same trap. Two of the opposing rods of the trap are rf-grounded, and the other two are connected to a radio-frequency source ($V_0 \cos \Omega t$) that generates an oscillating quadrupolar potential in the radial direction. The needles are connected to a dc voltage U_0 to confine the ion axially. Near the center of the trap, the electric field due to both rf and dc potentials is as follows [47, 45]:

$$\vec{E}(x,y,z,t) = -V_0 \left(\frac{x\hat{\vec{x}} - y\hat{\vec{y}}}{R'^2} \right) \cos(\Omega t) - \frac{\kappa U_0}{Z_0^2} [2z\hat{\vec{z}} - x\hat{\vec{x}} - y\hat{\vec{y}}]. \tag{3.1}$$

The $\hat{z}$-axis corresponds to the axial direction of the trap (Fig 3.1). The first term in Eq. (3.1) is due to the rf potential from the rods, and the second term is due to the potential from the end-caps. For simplicity, we have neglected the small component of alternating electric field that occurs in practice along the $\hat{z}$ direction. In the above equation, $2Z_0$ is the distance between the two needles and R' is approximately the distance from the trap axis to each of the electrodes, and κ is a geometrical factor. From Newton's Second Law of motion, the equation of motion for a single ion with mass m and charge Q in the above electric field obeys a Mathieu equation in each direction as follows:

$$\ddot{x}_i + [a_i + 2q_i \cos(\Omega t)] \frac{\Omega^2}{4} x_i = 0. \tag{3.2}$$

In this equation,

$$a_x = a_y = -\frac{1}{2} a_z = -\frac{4Q\kappa U_0}{m Z_0^2 \Omega^2}, \tag{3.3}$$

and

$$q_x = -q_y = \frac{2QV_0}{mR'^2\Omega^2}, \quad q_z \cong 0. \tag{3.4}$$

The position of the ion as function of time can be derived by solving the Mathieu equations in each direction assuming a_i«1 and q_i«1. The solution is as follows:

$$x_i(t) \approx x_{0i}\cos(\omega_i t + \phi_{Si})[1 + \frac{q_i}{2}\cos(\Omega t)] \tag{3.5}$$

where the phase, ϕ_{Si}, is determined by the initial conditions of the ion, and the secular trap frequency is:

$$\omega_i \cong \frac{1}{2}\Omega\sqrt{a_i + \frac{1}{2}q_i^2}. \tag{3.6}$$

As can be seen in Eq. (3.5), the motion of the ion in each direction consists of two oscillatory components: a low-frequency motion called secular motion and a high-frequency motion of relatively small amplitude, known as micro-motion. In the radial direction, the secular motion is associated with simple harmonic oscillation in a time-averaged pseudo-potential while, in the axial direction, a harmonic oscillator potential is generated directly by the dc endcap voltages U_0. The secular motion oscillates with the frequency of ω_i, and its amplitude x_{0i} can be reduced by cooling. Micromotion occurs at the same frequency as the rf trap frequency, Ω, and since it is assumed q «1, the micromotion's amplitude is much smaller than that of secular motion. The size of the micromotion is proportional to the displacement of the ion from the rf null and is minimized at the null rf point. The motion of the ion is shown in Fig 3.2.

As already mentioned above, the linear rf Paul trap is convenient for applications where two or more ions need to be simultaneously held in the trap. One advantage of the linear Paul trap is the ability to place several ions along the 1-D rf null, thus minimizing the effect of micro-motion on laser cooling and laser-based quantum operations on the system.

Our realization of a linear rf trap is shown in Fig 3.3. The four rods are made of tungsten and are held in place with precision ceramic spacers. The diameter of the rods is 0.48 mm, and their center-to-center distance is 1.27 mm. The two needles are also made of tungsten with tip-to-tip separation of 2.30 mm.

The rf frequency of $\Omega/2\pi \approx$ 30 MHz is inserted on two opposing rods via a bifilar quarter-wave resonator and the other two rods are rf-grounded. The simplified sketch of the potential connections to the four rods is shown in Fig 3.4. About 6 W of power is

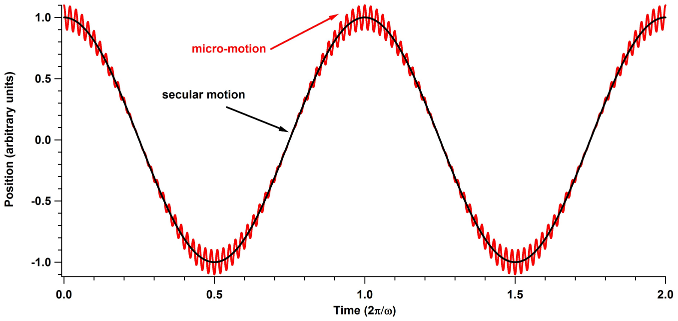

Figure 3.2: Motion of an ion in the radial direction of a linear rf Paul trap consists of two parts: secular motion with low frequency ω and large amplitude, and micro-motion with high frequency Ω and small amplitude. Secular motion alone is shown in black while the combined motion is shown in red. In the axial direction, there is nominally no micro-motion.

applied to the rf resonator, which has a quality factor of 100-200. The endcaps use ∼26 V. Four π-filters allow us to apply a separate dc voltage to each rod through an rf ground in order to move the ion onto the rf null. The secular trap frequencies are measured by ac-coupling an oscillating voltage onto the electrodes, and the result from direct excitation is $\{\omega_{r1}, \omega_{r2}, \omega_{axial}\} = \{2\pi \cdot 0.41, 2\pi \cdot 0.43, 2\pi \cdot 0.18\}$MHz for the trap used in this thesis.

The ion trap setup needs to be kept in an ultra-high vacuum system to achieve long ion-trap lifetimes. We achieve lifetimes from several hours to several days. Inelastic collisions with the background gas lead to population of the long-lived $^2F_{7/2}$ state about every 10-30 mins, and a 638-nm laser is required to repump the ion out of this state. More rarely, inelastic collisions also lead to molecular-ion formation [48], although we are often able to recover the Ytterbium ion through the use of a strong (12 mW) UV beam. Presumably, other occasions when the ion truly leaves the trap are due to charge-exchange collisions with background gas atoms or heating out of the trap.

An ion pump in combination with a titanium sublimation pump is used to keep the pressure of the vacuum chamber low. An ion gauge which is somewhat remote from the trap location (see Fig 3.5) normally has the pressure of $< 10^{-11}$ torr. When the pressure at the ion gauge exceeds this value, we flash titanium sublimation pump. This is typically done once a month. The titanium sublimation pump consists of a titanium filament through

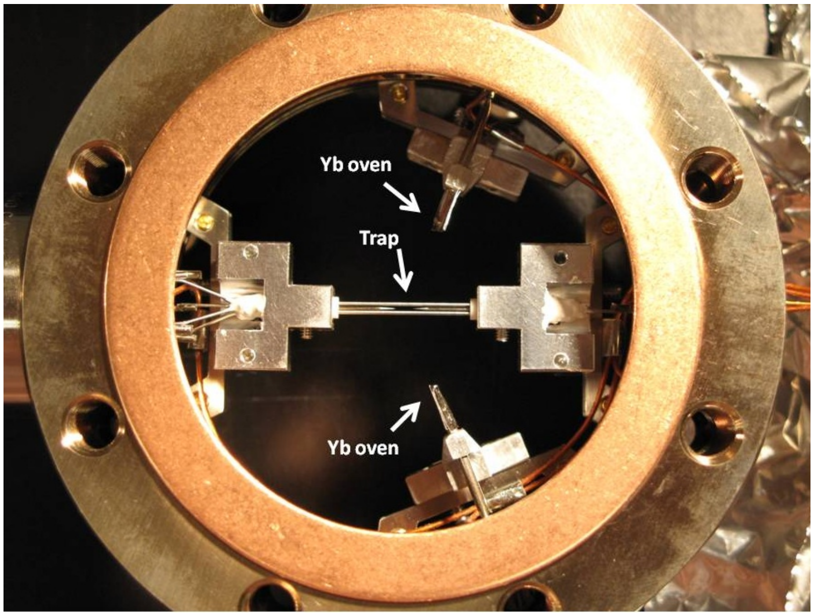

Figure 3.3: Top view of SFU linear rf Paul trap in the vacuum chamber.

which a high current of about 43 A is passed for ∼5 min. This current makes the titanium filament reach sublimation temperature. The surrounding walls become coated with a fresh, thin film of titanium. Fresh titanium reacts readily with background gases in the trap and forms a stable, solid product; hence, the pressure in the trap reduces significantly.

3.2 Photo-ionization loading of ions

Once the trap is assembled and the chamber has reached ultra-high vacuum pressure, the next step is loading Ytterbium ions into the trap. This process begins with an effusive atomic beam of neutral Ytterbium produced by an oven. The oven located near the trap consists of solid Ytterbium metal in a stainless steel tube that is heated resistively with a current around 5 A. The increased temperature evaporates the Ytterbium, which travels to the trap in a reasonably collimated beam. We use a photo-ionization method to ionize the Ytterbium atoms coming from the oven. The other possible method is electron bombardment, which uses an electron beam with kinetic energy higher than the ionization threshold of the neutral atom. Photo-ionization is known to be more advantageous compared to elec-

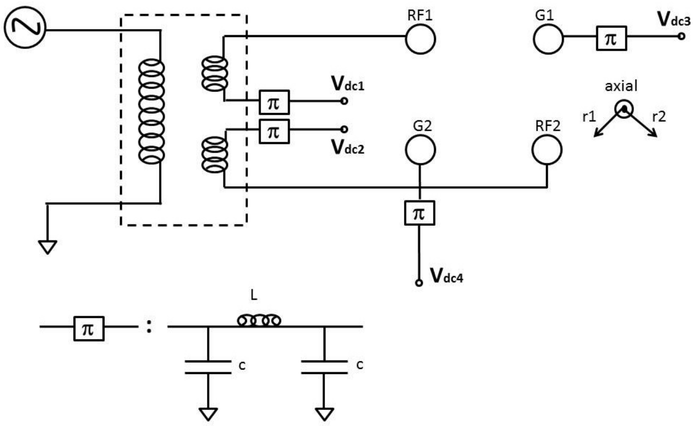

Figure 3.4: Trap rf-voltage circuit diagram. All four rods are connected to π-filters that allow us to dc bias each rod independently. The RF frequency is inserted via a bifilar quarter-wave resonator, indicated by the dashed boundary.

tron bombardment ionization [49, 50, 51, 10], because an electron gun's hot filament spoils the ion-trap pressure. Furthermore, the electron beam can also charge the insulators near the ion trap and impact its performance. By comparison, photo-ionization does not effect the pressure and is less likely to lead to charging effects as long as material work-functions are sufficiently high. Photo-ionization is also isotopically selective and significantly more efficient [49, 50, 51, 10].

In the photo-ionization process, a 398.9-nm external-cavity diode laser is used to resonantly excite neutral Yb atoms from the $^1S_0$ to $^1P_1$ state. There are two possibilities for ionizing the atom in the $^1P_1$ state [10]. The atom can absorb another photon at 399 nm and reach a high-lying Rydberg level, which can then be ionized by the trap electric fields. Alternatively, a 369.5 nm photon from the laser used for ion cooling has sufficient energy to remove the electron in the $^1P_1$ state directly to the continuum (see Fig 3.6). During loading, the 398.9-nm laser is overlapped with a relatively high power 2 mW 369.5-nm laser beam. The 398.9-nm laser beam has a waist diameter of $60-100\mu$m and is maintained at a reduced power of about 100 μW to limit saturation broadening of the $^1S_0$ – $^1P_1$ transition and thereby improve the isotopic selectivity of the photo-ionization. The high power 369.5-nm beam is presumed to dominate the second step of photo-ionization [10]. The photo-ionization beam is also perpendicular to the atomic beam coming from the oven to

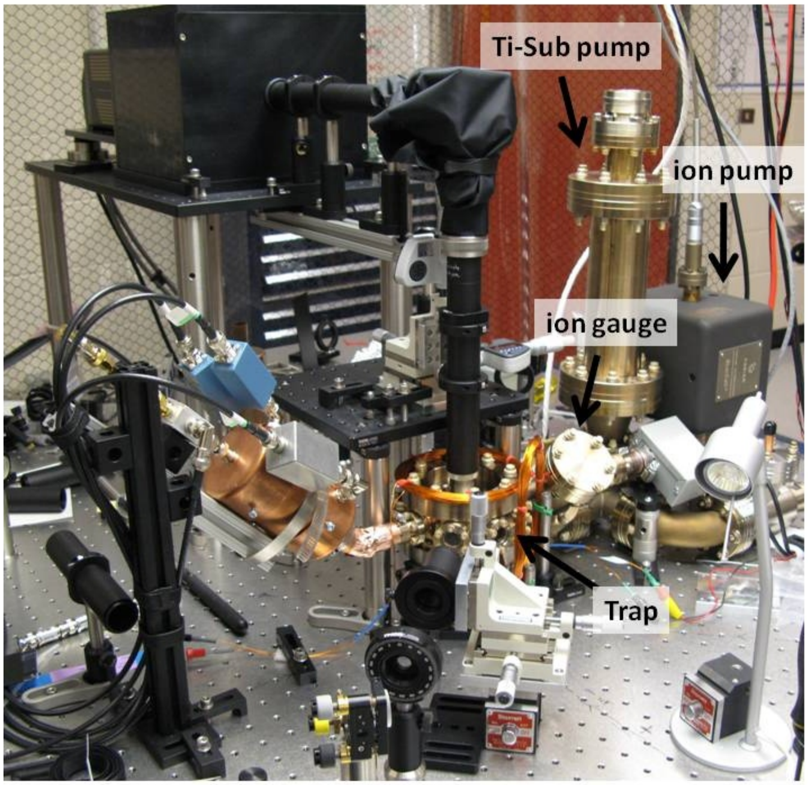

Figure 3.5: Location of ion pump and Titanium-Sublimation pump

minimize Doppler broadening (see Fig 3.7).

Finally, it worth noting that the energies of the 399 nm and 369.5 nm photons are approximately 3 eV, which is below the work function of the tungsten trap electrodes (4.5 eV). Hence, photo-electric charging is expected to be minimized during the photo-ionization process. In Chapter 5, some of our early photo-ionization studies will be presented as part of the basic trapping procedure of Yb^+.

3.3 Doppler cooling

After photo-ionization loading, the trapped Yb^+ ion is Doppler cooled by a 369.5-nm beam on the $^2S_{1/2}$ to $^2P_{1/2}$ transition. The beam is produced by a frequency-doubled and amplified diode laser system at 739.05 nm. A lithium triborate (LBO) crystal in a bow-tie res-

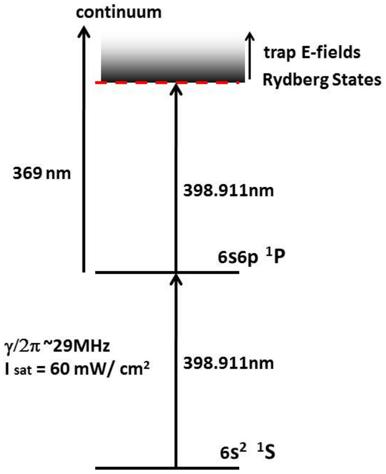

Figure 3.6: One- and two-color photo-ionization processes for neutral Ytterbium.

onant cavity produces about 5 mW of UV power from 250 mW of fundamental power. A single-mode, polarization-maintaining fibre is used to transfer the UV beam from the laser to the experiment path. The fibre gives a positionally stable beam going to the trap that is not affected by the frequent alignments of the doubling cavity. The fibre output also gives a high quality beam. The fibre input-coupler is a PAF-X-5-A fibre port from THORLABS, which allows micro-positioning alignment, and in practice, gives stable alignment. The UV beam's path to the trap is shown in Fig 3.8. There is a polarized beam-splitter (PBS), right after the fibre's output to convert the polarization noise, which arises from residual thermal drifts, to amplitude noise. The beam out of the PBS goes to a variable power divider composed of a half-wave plate (HWP) and another PBS. The HWP is set to ∼95°, which makes the ratio of power in the two output paths 90/10. A power of 2 mW goes to a path used for loading and 200 μW goes to the other path used for detection/cooling.

The detection/cooling beam, after passing through the dividing PBS, reaches a 200 mm lens that focuses the beam into a 7.37 GHz free-space resonant electro-optic modulator (EOM) used to impose frequency sidebands on the laser beam for hyperfine repumping. The second sideband is used to drive the $^2S_{1/2}(F=0) \rightarrow ^2 P_{1/2}(F=1)$ transition in $^{171}\mathrm{Yb}^+$ (see Fig 3.10) and pump the ion from the $^2S_{1/2}(F=0)$ state back to the fluorescence cycle. The beam out of the 7.37 GHz EOM goes to a HWP to change the polarization to vertical,

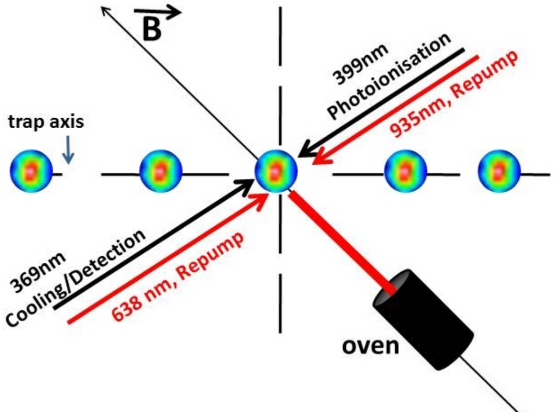

Figure 3.7: Top view of the laser beam paths to the trap along with the location of the oven and the direction of the magnetic field

which is needed for the next EOM at 2.1 GHz. The first sideband imposed by the 2.1 GHz EOM is resonant with the $^2S_{1/2}(F=1) \rightarrow^2 P_{1/2}(F=1)$ transition. This transition is used to initialize the ion to the $\left|F=0, m_f=0\right\rangle$=$|\downarrow\rangle$ state via optical pumping at the start of quantum information experiments. Further information on hyperfine repump and optical pumping is provided in Chapter 5. The two EOMs together reduce the beam's power approximately by half due to absorptions by the crystals inside the EOMs. We keep the power of the beam in the cooling/detection path low to prevent any crystal damage due to photo-refractive effects. The beam from the 2.1 GHz EOM is collimated and sent to an 80 MHz acousto-optic modulator (AOM) from IntraAction Corp. The first order diffracted beam is picked off for use in the experiment and its frequency is up-shifted by the AOM frequency. In our experiment AOMs are used primarily to switch and to vary the power of the laser but may be used also to tune its frequency. The beam out of the AOM reaches a PBS, which reflects the pure vertically polarized beam to a final HWP, which sets the polarization of the beam to the trap. Finally, the beam goes through a 10 cm focal-length lens mounted on an XYZ translation stage, which controls the beam's focus and position at the trap. The power of the beam going into the vacuum chamber is around 60-70 μW.

The high-power 369.5 nm loading path is used primarily during the loading procedure and it goes through a separate 80 MHz AOM for power switching. The diffracted beam from the AOM passes through two 20 cm lenses used for beam collimation and independent

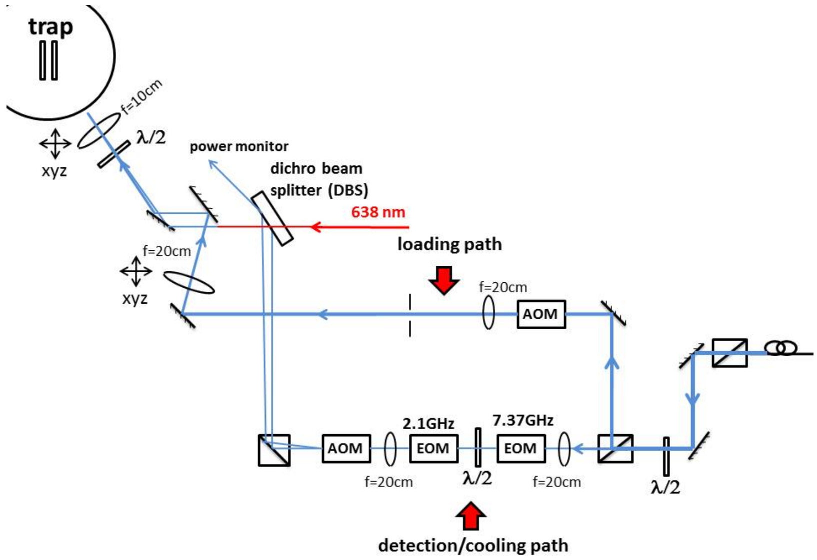

Figure 3.8: The path of the 369.5-nm laser beam to the trap. The path is divided into two parts, the loading path with a high power and the detection/cooling path with lower power.

alignment adjustment and combines with the cooling and detection beam before the final HWP (see Fig 3.8).

In order to keep the ion in the cooling/detection cycle, 935-nm and 638-nm lasers are needed for repumping. The 935-nm laser is used to drive the ion from the metastable $^2D_{3/2}$ state back to the $^2S_{1/2}$ state and the 638-nm laser is used to depopulate the $^2F_{7/2}$ state (see Fig 2.1). The 935-nm beam's path to the trap is shown in Fig 3.8. The 935-nm beam is fibre coupled from the laser and has a power of about 2-3 mW at the trap. The beam is also modulated by a broad-band fibre modulator at 3.07 GHz to depopulate the $^2D_{3/2}(F = 2)$ state of $^{171}\mathrm{Yb}^+$. The 935-nm beam and modulation sidebands are continuously on during the experiment. The 638-nm laser is overlapped with the 369.5-nm beam via a dichroic beam-splitter (see Fig 3.8) and is also continuously on during the experiment. All four lasers are coupled to a wavemeter to monitor their wavelength. Details of the laser paths to the wavemeter are provided in the following chapter.

To ensure a stable detuning and narrow linewidth, the 369.5-nm and 935-nm lasers need to be stabilized. The 369.5-nm laser's fundamental wavelength at 739 nm is stabilized before frequency doubling. The 739 nm ECDL 's linewidth is narrowed using a

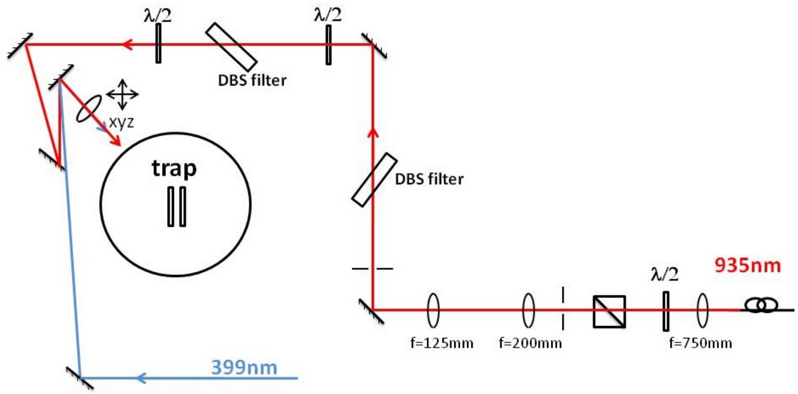

Figure 3.9: The path of the 935-nm laser beam to the trap.

Pound-Drever-Hall lock to the doubling resonator cavity. Long-term drifts are prevented by locking the laser to a hyperfine absorption line of molecular iodine using a saturated absorption technique. The 935-nm laser is stabilized at long times with a transfer-lock setup which is based on a Fabry-Perot cavity locked to the stabilized 739-nm laser. The 935-nm laser linewidth is also narrowed by using the cavity error signal and fast current feedback. The details of the lock setups are given in Chapter 4.

In addition to all of the lasers, an external magnetic field is needed to provide a quantization axis and to overcome coherent population trapping in $^{171}\mathrm{Yb}^{+}$. The magnetic field in the trap is generated by a single Helmholtz coil with 100 turns. The coil is located approximately 75 mm from the trap center. Inhomogeneity of the magnetic field is not an issue for our primarily single-ion experiments since the ion position is stable. The magnetic field is arranged to be nominally perpendicular to the 369.5-nm laser beam path (see Fig 3.11). The magnetic field in the trap center can be varied by changing the current of the coil.

3.4 Imaging System

Scattered photons from the ions are collected with an anti-reflection-coated UV microscope objective lens with a focal length of 20 mm and a high numerical aperture (NA $\approx$ 0.23). For efficient light gathering, reentrant windows are used to accommodate the 13 mm working distance of the objective. An intermediate image of the ion(s) is focused about 20-30 cm

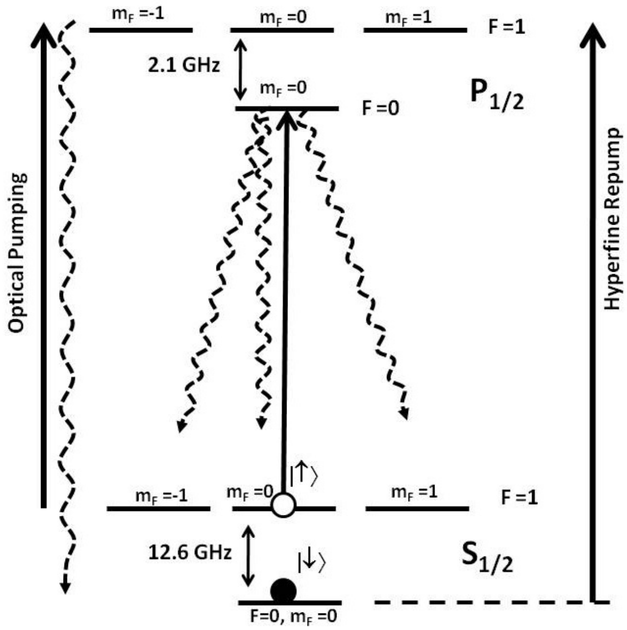

Figure 3.10: Zeeman resolved structure of ^{171}Yb$^+$ with the qubit's $|\downarrow\rangle$ and $|\uparrow\rangle$ states. Optical pumping is used to initialize the ion in the $|\downarrow\rangle$ state and a hyperfine repumping beam is used to repump the $|\downarrow\rangle$ state to the bright state

behind the objective where a 600 μm pinhole is used to block scattered light. A back-to-back pair of 75 mm lenses re-images the ion(s) into an intensified CCD camera for diagnostic purposes or onto a photo-multiplier-tube (PMT) for measurement of the ion fluorescence by photon counting. The total magnification of the imaging system is about 140.

The net photon collection efficiency of the PMT-based imaging system is about $3 \cdot 10^{-3}$. The PMT's detection efficiency is not spatially uniform. To suppress drifts in photon count rates, we check the position of the ion's image on the CCD camera consistently during the experiment and adjust the imaging system as needed. A dichroic mirror is also added to the imaging optical path to suppress all except UV photons from reaching the camera and PMT. The 638-nm and 935-nm lasers do not appreciably contribute to the PMT background count rate. An image of three ions is shown in Fig 3.12.

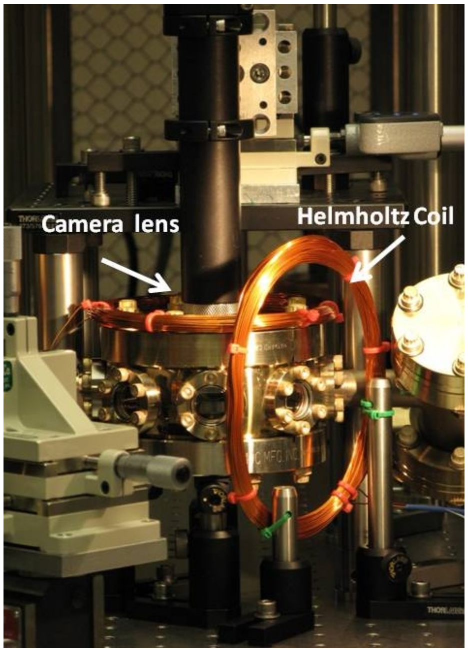

Figure 3.11: Side view of the trap showing the position of imaging objective lens and Helmholtz coil. The 369.5-nm laser enters from the left and the coil generates a field nominally perpendicular wavevector of the laser.

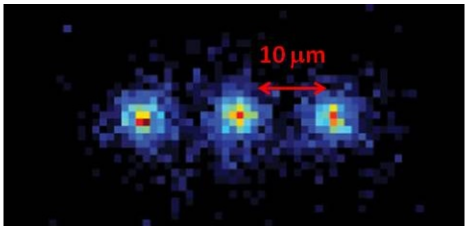

Figure 3.12: A picture of three ^{171}Yb^{+}ions taken with the intensified CCD camera. each pixel is binned eight-fold in both directions. The separation between ions is 10 μm.

Chapter 4

Lasers and Lock Setups

In this chapter we explain in detail three of the lasers used in the experiment: the 399-nm laser used for photo-ionization, the 369.5-nm frequency-doubled laser used for Doppler cooling and detection, and the 935-nm laser used to repump the ion from the ${}^2D_{3/2}$ state. In particular we describe the lock setups for 369.5-nm and 935-nm lasers, including a check on the stability of the lasers using a wavemeter. This gives a simple diagnostic but, in the next chapter, we ultimately compare the stability of the lasers with respect to the optical resonances of the ions themselves. Note that a discussion of the 638-nm laser required for depopulating the metastable ${}^2F_{7/2}$ state is left to a future thesis.

4.1 The 399-nm laser

We use a tunable, grating-stabilized external-cavity diode laser (ECDL) from TOPTICA (model DL100) for photo-ionization at 399 nm. A simplified mechanical schematic of the DL100 is shown in Fig 4.1. As can be seen in the figure, external optical feedback is produced by a grating set to the Littrow configuration, which gives considerably higher output power than other possible configurations. The zero-order reflection of the grating forms the output beam, while the first-order diffraction goes back to the laser diode as optical feedback, and creates a resonator between the diode's back facet and the grating (see Fig 4.1). This external cavity has a higher finesse compared to the cavity formed by the laser diode's facets; hence, the laser's linewidth is significantly smaller (a few MHz) compared to the free-running diode. The laser's wavelength can be changed by rotating

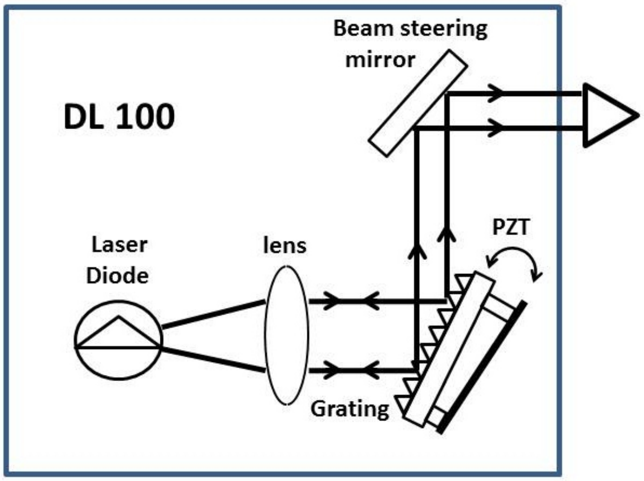

Figure 4.1: Schematic sketch of the tunable, grating-stabilized, external-cavity diode laser from TOPTICA. The beam-steering mirror is mechanically attached to the grating (not shown).

the grating about the vertical axis with a piezo actuator. The Littrow configuration has the side effect that moving the piezo tilts the output beam's direction slightly, which can lead to large beam-walk downstream. A beam-steering mirror is fixed to the grating holder to limit the effect of the tilt to a small lateral displacement. To get a wide mode-hop-free tuning range, a feed-forward mechanism is used to add a compensating laser current as the grating is tuned. There are three electronic modules in the Toptica control rack for precise control of the diode laser's current, temperature and piezo. Typical values of current and temperature we use for this laser are I_{LD} = 47 mA and T_{LD}=23.6°C.

The beam from the laser passes through a 30 dB optical isolator from Optics for Research, and is separated into two parts. One part, with a power of $\sim$8 mW, goes to the ion trap through free space, and the other part, with a power of $\sim$2 mW, is sent to a fibre-coupled Bristol wavelength meter for wavelength determination and also to a Fabry-Perot cavity for ensuring single- mode operation. A schematic of the 399-nm beam's optical path out of the laser is shown in Fig 4.2.

The 399 nm ECDL has been the most robust of our lasers during the last five years and has required no significant maintenance. On a daily basis, we adjust the current to get a

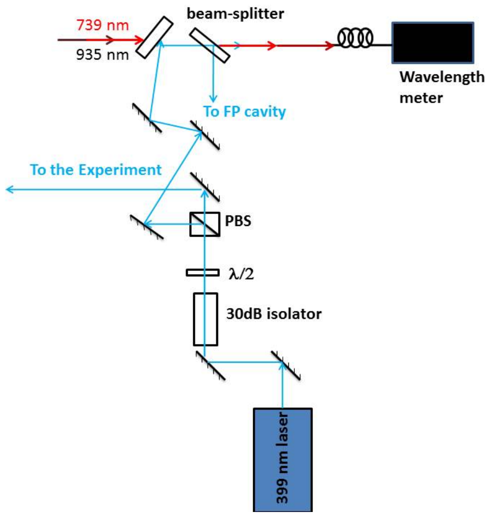

Figure 4.2: The optical path of the 399-nm laser beam to the experiment and to the diagnostic path consisting of a wavemeter and Fabry-Perot cavity.

single longitudinal mode and then adjust the piezo to get the desired wavelength. The 399-nm laser's passive linewidth is good enough for isotope-selective photo-ionization, during which we are power broadening the resonance somewhat anyway. Moreover, the loading process takes less than one hour and the long-term passive stability of the 399-nm laser seems to be adequate. In the future, it may be useful to stabilize the laser to remove the long-term drifts.

4.2 The 369.5-nm laser

4.2.1 Laser description

Doppler cooling and detection on the $^2S_{1/2}$-$^2P_{1/2}$ transition at 369.5 nm are accomplished with an amplified, frequency-doubled diode laser system from TOPTICA. A schematic sketch of the laser setup is shown in Fig 4.3. As can be seen in the figure, the 739-nm beam out of the DL100 master oscillator (the same design used for the 399-nm laser) goes to a single-pass, tapered semiconductor-amplifier (TA100). There is a 60 dB Faraday optical isolator between master oscillator and tapered amplifier to prevent feedback reflections back to the master oscillator. Because of the elliptical polarization out of the master ECDL, about half of the power is lost through the isolator with only about 4.5 mW transmitted. This is enough for reasonable operation of the tapered amplifier. Following the amplifier there is another 60 dB isolator to inhibit feedback from the doubling cavity to the amplifier. We get ∼300 mW out of the amplifier after the isolator with ∼4.5 mW input power. The amplified beam is separated immediately after the isolator into two parts with a 90-10 beam-splitter. About 10%, or 25 mW, is transmitted out of the laser enclosure and is used for locking and diagnostics, while 90% is reflected towards the frequency-doubler.

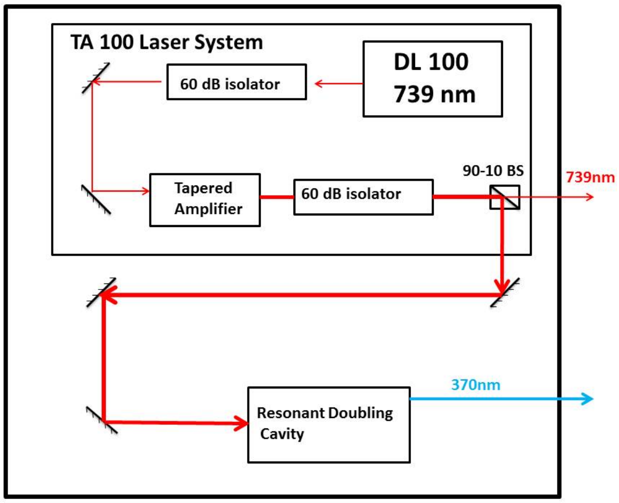

Figure 4.3: Schematic sketch of the Toptica 369.5-nm laser which consists of a 739-nm DL100 master oscillator, amplifier, and resonant doubling cavity. Two 60 dB isolators prevent master-amplifier and amplifier-cavity feedback.

The frequency-doubling cavity has a bow-tie design (see Fig 4.4) with two plane mirrors and two concave mirrors. The doubling crystal is placed in the tight beam waist between the two concave mirrors. The doubling crystal is lithium triborate (LBO), which is used at normal incidence with an AR coating to minimize reflections. The UV beam out of the doubling cavity first passes through a plano-concave cylindrical lens, which reduces astigmatism, and then a collimation lens before exiting the laser enclosure with a power of about 5 mW. This output beam is transferred to the experiment via a PM fibre with a coupling efficiency of 40%.

The bow-tie cavity is used to improve the UV power of the laser by resonant enhancement of the doubling process and needs to be stabilized to the input fundamental. At the same time the cavity is used as a reference to narrow the linewidth of the 739-nm master. The error signal for both these purposes is obtained from a Pound-Drever-Hall lock signal as follows. The master is frequency modulated at $\sim$20 MHz via its current. As can be seen in Fig 4.4, the input-reflection port of the cavity is sent to a fast photo-diode, which is connected to the input of a Thorlab's PDD module (Pound-Drever-Hall demodulator). The dispersive error-output of the PDD is split and fed back to the cavity via a PID module (proportional integral derivative) and to the laser via its current. The output of the PID module is connected to a piezo mounted on one of the plane mirrors of the resonator cavity and acts to maintain the cavity on resonance with the input fundamental. The lock of the resonator cavity to the laser is a slow loop with a bandwidth of few kilohertz and can regulate slow thermal and acoustic noise affecting the cavity. The lock of the laser to the cavity is a fast lock that feeds back to the diode current using a FET (field effect transistor) current control. This fast feedback is a pure proportional regulator with a bandwidth of 5 MHz, but it has a small locking range. With all the locks in place, the laser frequency can still drift over hours. To remove slow drifts for the 739-nm master laser, a molecular iodine absorption line is used as a long-term reference, as described in the following section.

4.2.2 Lock setup for the 739-nm laser

To avoid long-term drifts of the 369.5-nm laser, caused by factors like temperature fluctuations in the lab, a saturated absorption lock is implemented to stabilize the 739-nm fundamental to molecular iodine. Molecular iodine has a rovibrational $B0u^+ \leftarrow X0g^+$ electronic transition that provides a dense comb of narrow hyperfine absorption lines from green to near-infrared wavelengths (500 nm-900 nm). Ytterbium's cooling/detection wavelength corresponds to about one-half of 739.05-nm, which lies in the IR region where iodine absorption lines start from high vibrational levels [52]. These high levels need to be populated thermally by heating the iodine cell [53]. We heat the cell to 420°C . Iodine's boiling point is 184.3°C; therefore, at 420°C there would be a high vapour pressure in the cell, which would lead to pressure broadening and shifts in the absorption lines. To overcome this problem, a cold finger near room temperature is added to the cell to regulate its vapour

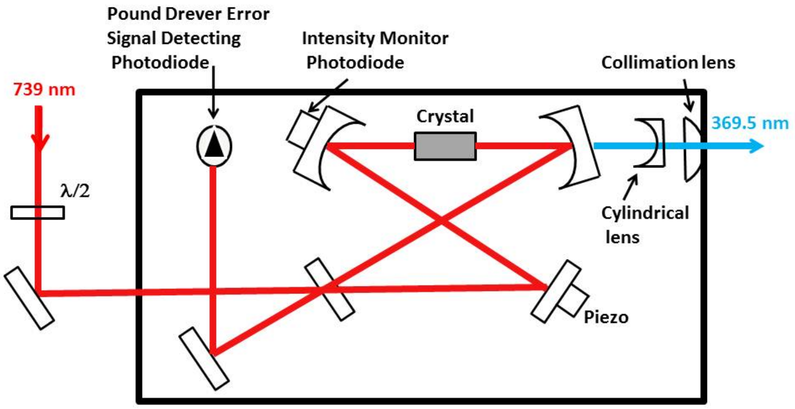

Figure 4.4: The resonator doubling cavity in the 369.5-nm laser. The cavity is a bow-tie design and uses an LBO crystal for frequency-doubling.

pressure (see Fig 4.5). The iodine cell is 15 cm long and 2.5 cm diameter with 2 degree wedged mirrors to prevent reflection fringes. The cold finger extends 75 mm from the cell's body. The cell is insulated with ceramic wool and aluminium foil to reduce temperature variation on the optical table. At the high temperatures in the cell, Doppler broadening increases the natural linewidth of absorption from a few MHz to a few GHz, which is unsuitable for locking purposes. To eliminate Doppler broadening, the saturated absorption technique is used.

The schematic of our iodine lock setup, which has been constructed prior to this thesis as part of several undergraduate projects, is shown in Fig 4.6 and is similar to pump-modulation saturated absorption setups presented in Refs. [53, 11]. The iodine setup is located on a separate table in part to keep the hot iodine cell from affecting other optical setups of the experiment. The 739-nm beam is transferred to the iodine table by a PM fibre. The iodine absorption line we have chosen to use has a wavelength of 739.0337-nm which is several gigahertz different from the wavelengths associated with the different Yb^+ isotopes (For example the wavelength of the UV transition for $^{171}\mathrm{Yb}^+$ corresponds to 739.0521 nm before doubling, which is around 10 GHz away). Hence, the fibre-coupled

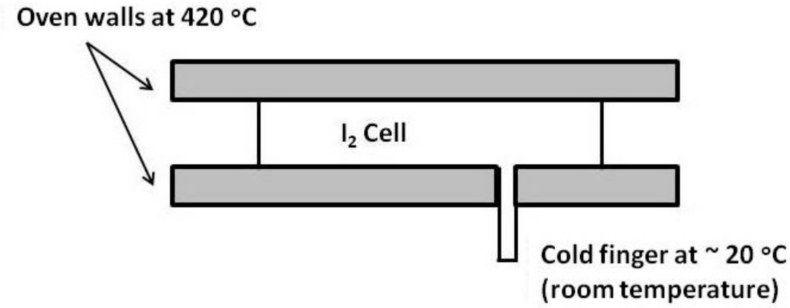

Figure 4.5: Iodine cell with the cold finger

beam is sent to a fibre EOM to provide an offset sideband that bridges the gap. The EOM is directly driven by an HP 8672 synthesizer at full power. The frequency synthesizer provides 3 kHz adjustment from the front panel or remotely via GPIB. The beam out of the fibre EOM has a power of 4.5 mW and reflects from a PBS that cleans the polarization and then goes through a thick plate beam-splitter, which separates the beam into three parts. Two reflections from the surfaces of the splitter provide the "probe" and "reference" beams and have a power of 100-200 μW. Most of the beam passes through the splitter to provide the "pump" beam. The strong pump and weak probe beams enter the cell in opposite directions.

The pump beam first passes through an AOM before entering the cell, and its frequency is shifted and modulated by $\nu_{AO} = 80$ MHz$+\Delta\nu \sin(\omega_{mod} \cdot t)$, where $\Delta\nu \sim$4 MHz and $\omega_{mod}/2\pi$ =20 kHz in our setup. The $\sin(\omega_{mod} \cdot t)$ term leads to a dispersive signal after demodulation with a robust zero-crossing that is suitable for locking [54, 53]. The probe and reference beams go to an autobalance detector that subtracts the two signals to ensure a zero baseline for the signal. Since the absorption and, specifically, saturated absorption signals are not very strong, a lock-in technique is used to increase the signal-to-noise ratio.

The iodine saturated-absorption spectrum near 739.0337 nm has many hyperfine lines available for locking. In Fig 4.7, we show the line used for locking. The feature is a relatively strong, isolated line that avoids the ambiguity of several closely spaced zero-crossings (compare other features in Fig 4.7). In Fig 4.8(a), the magnified picture of the same signal is shown for two output time constants of the lock-in amplifier. In Fig 4.8(b), the error with the 739-nm laser locked to the zero-crossing is shown for the same two time

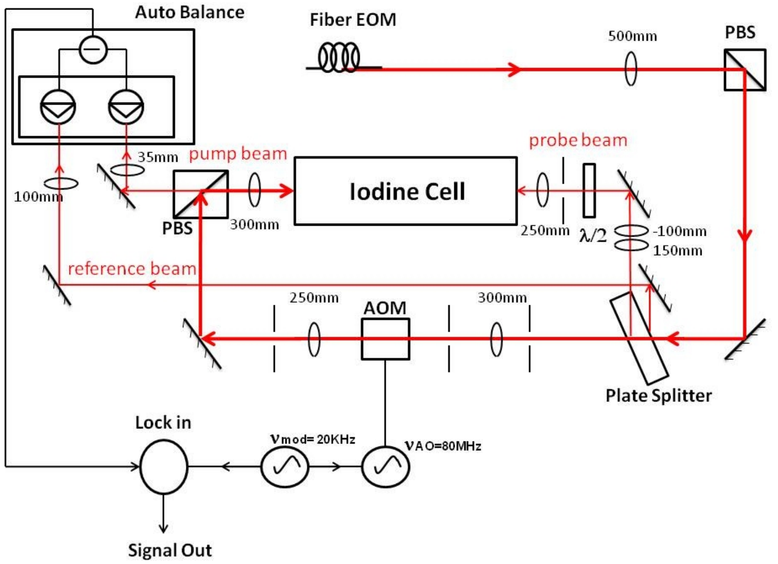

Figure 4.6: Schematic of the iodine setup used for locking the 739-nm laser.

constants. It can be seen that, for τ =10 ms, the noise amplitude is 100 mV_{pp}, which is 17% of the signal and corresponds to a 1.4 MHz frequency excursion while, for τ=1 ms, the noise amplitude is 300 mV_{pp} which is 43% of the signal and corresponds to a 0.47 MHz frequency excursion. The frequency of the noise is 60 Hz and 120 Hz, that is, line noise. Since we only intend the iodine lock to account for slow drifts, we use a large lock-in time constant to filter out the 60/120 Hz noise. Even further filtering is applied before the signal is fed back to the laser. In the future, we intend to identify the source of line noise in the lock path and eliminate it.

4.3 The 935-nm laser

4.3.1 Laser description

The 935-nm laser, used for repumping the ion from the ${}^2D_{3/2}$ state, is another DL100 from Toptica with similar design to the 399-nm laser and with similar control modules for temperature, current and piezo. Typical current and temperature values are I_{LD} = 125 mA and T_{LD}=19°C. The beam out of laser passes through a 30 dB isolator from Optics

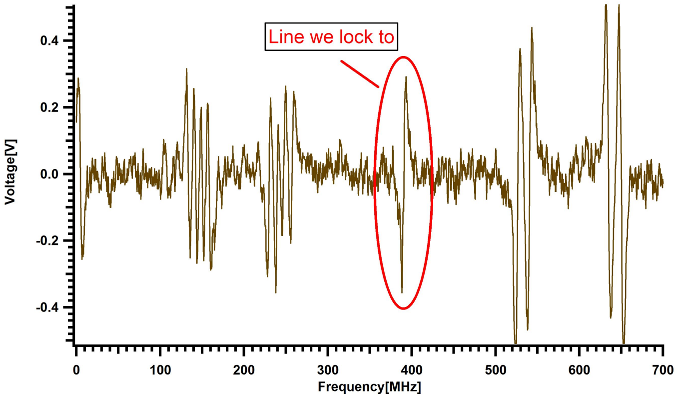

Figure 4.7: Saturated absorption spectrum of iodine near 739.0337 nm showing resolved hyperfine structure. The dispersive line shapes are due to pump-frequency modulation. The line used for locking is also identified.

for Research, and separates into three parts. About 20 mW of the power is sent to a fibre coupler for use in the experiment, 2 mW goes to the Bristol Wavelength meter through free space, and the remaining 6 mW is sent to the lock setup through another fibre.

The performance of the original 935-nm laser deteriorated over the years, leading it to go multimode on a regular basis. Some of the lock-setup data that is presented in later sections used this laser; however, the laser diode has since been replaced to improve performance.

The 935-nm laser needs to be locked to remain stable over several hours of the experiment. The lock setup for this laser is explained in the following section.

4.3.2 Lock setup for the 935-nm laser

To prevent long term drifts of the 935-nm laser, we reference it to the 739-nm laser, which in turn is stabilized to iodine. A Fabry-Perot cavity is used to transfer the stability of the 739-nm laser to the 935-nm laser. Additionally, the short-term stability of the cavity is used as a reference to narrow the linewidth of the 935-nm laser using fast diode-current feedback.

In the following sections the transfer-cavity lock setup is explained in detail. Before we provide more information on the lock setup, it is useful to study the properties of the

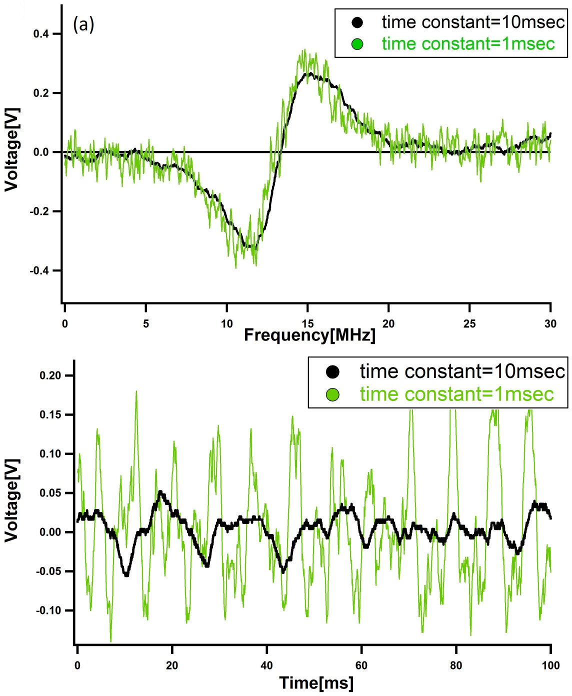

Figure 4.8: (a): Demodulated iodine signal out of the lock-in amplifier for output time-constants of 1 ms and 10 ms. To obtain the plot, the frequency of the laser is scanned slowly to avoid suppression of the peak amplitude. The scan-range is calibrated by using the lock-offset synthesizer. (b): In-loop lock errors corresponding to each of the time constants in (a).

Fabry-Perot cavity as it forms the main part of the transfer lock.

4.3.3 Fabry-Perot cavity

A Fabry-Perot cavity is an optical resonator consisting of two mirrors displaced by a distance L. For a cavity with the length of L, a laser field with wavelength λ_N can be on resonance with the cavity if

$$\lambda_N = \frac{2L}{N \cdot n} \qquad N \in \{1,2,3,...\}. \tag{4.1}$$

In the above equation, N labels the resonance mode, and n is the refractive index of air inside the cavity.

The free-spectral range (FSR) of a non-confocal resonator cavity is defined as the frequency spacing of cavity's successive resonator modes [55]:

$$FSR = \frac{c}{2L}. \tag{4.2}$$

Our cavity design consists of two concave mirrors set to a confocal configuration. In a confocal configuration the separation between the two mirrors is equal to their radius of curvature, and has the benefit that it makes the transverse spatial modes degenerate in frequency. We follow the definition of the FSR in Eq. (4.2) for the case of our confocal cavity as well. In that case, the even and odd modes are separated by FSR/2 (see Fig 4.9(a)).

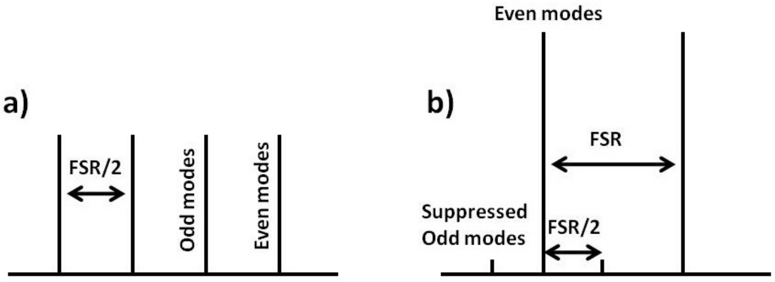

Figure 4.9: a) The odd and even resonant modes in a confocal cavity separated by FSR/2 (see text). b) Suppressed odd modes and enhanced even modes for symmetric input-coupling.

The finesse of the cavity resonance is defined as the FSR of the cavity divided by the bandwidth of its resonance (full width at half maximum) [55]:

$$Finesse = \frac{FSR}{FWHM} = \frac{\pi\sqrt{r}}{1-r}. \tag{4.3}$$

In the above equation, r is the amplitude reflectivity of the cavity's mirrors. All values of the finesse quoted here will be calculated using the non-confocal FSR. A higher signal and finesse can be achieved by mode-matching to the single lowest mode of the cavity. We do this partially by obtaining a well-centered alignment for the input beam so that the odd modes are suppressed. This gives a factor of 2 increase in peak transmission-signal without perfect coupling (see Fig 4.9(b))

Since our cavity is to be used as a transfer cavity, it needs to be on resonance with both of the 739-nm and 935-nm input beams. However, in general, the cavity will not be simultaneously resonant with the 935-nm and 739-nm wavelengths required for a given Yb^+ isotope, except for very specific lengths of the cavity. The effect of a change in cavity length can be understood as follows. Suppose the $(2N')^{th}$ even mode is on resonance with the 739-nm laser and, at the same time, the $2N^{th}$ even mode is on resonance with the 935-nm laser for a given length of the cavity (see Fig 4.10(a)). If the length of the cavity is changed slightly to bring the next mode – the $2(N'+1)^{th}$ mode – on resonance with the 739-nm laser, the cavity resonance for the 935-nm laser will not move to its next mode, that is, the $2(N+1)^{th}$ mode. For a given cavity length change that leads the 739-nm laser to move by one FSR, the cavity resonance will move relative to the 935-nm laser by a frequency as follows:

$$\Delta\nu_{935} = n_{935}\frac{\Delta\nu_{739}}{n_{739}} = \frac{\lambda_{935}}{\lambda_{739}}FSR. \tag{4.4}$$

For our setup, the cavity has a length of $L = 75$ mm, and its free spectral range is 2 GHz (see Eq.4.2); hence, the "mismatch" is $\Delta\nu_{935}$ =1.58GHz or, equivalently, FSR- $\Delta\nu_{935}$= 420 MHz.

On a daily basis the cavity is not expected to maintain a fixed length. However, the mismatch calculation shows that, at worst, if we move the cavity by 5 FSR 's at 739 nm, then we reach another similar point of operation.

To account for residual relative offsets and to allow for the tuning of the 935-nm laser while locked, we use a fibre frequency-modulator to modulate the laser, and lock the cavity

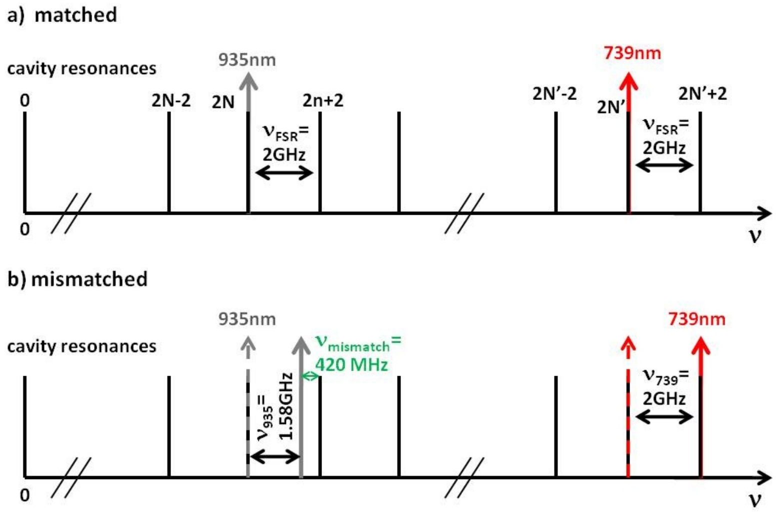

Figure 4.10: a) The even-mode resonances of the cavity are shown with 935-nm and 739-nm laser frequencies simultaneously resonant (the "matched" case). b) The length of the cavity is changed so that the 739-nm laser resonates with the next even mode. However, the 935-nm laser will no longer match with a cavity resonance (the "mismatched" case).

to the first sideband. The sideband's frequency is changed by an HP8640 signal generator. The signal generator is connected to a rf frequency-doubler (Minicircuits FK-3000), allowing easy access to the frequency range of 0-2 GHz.

4.3.4 Cavity, lock optical setup

The picture of our Fabry-Perot cavity is shown in Fig 4.11. All mechanical components other than rods are part of a Thorlab cage kit, except the stainless steel rods were replaced by 6 mm diameter Invar rods to improve thermal stability. The two plano-concave mirrors M1 and M2 are made of fused silica with a 75 mm radius of curvature. The mirrors are triple HR coated for 399 nm, 740 nm and 935 nm, and the reflectivity is 99.7% for these wavelengths. The back mirror (M2) is glued to a piezo-electric tube with stress coefficient of about 5 μm/kV. The cavity is supported by a single 2.5 cm post attached to point P4 in Fig 4.11.

To set the cavity on a confocal configuration, we used the 739 nm laser. The transmitted

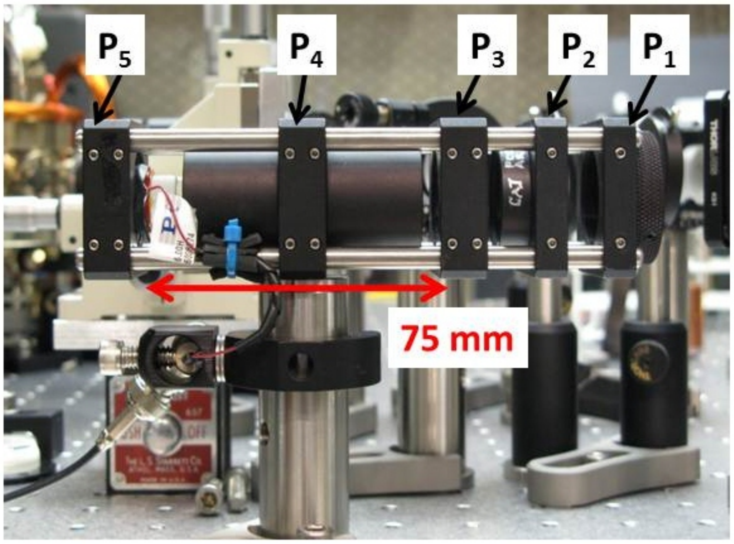

Figure 4.11: The confocal Fabry-Perot cavity used in the transfer lock setup. The support structure consists of four invar rods passing through Thorlabs thick cage plates (P_3, P_4 and P_5) with a 2.5 cm support post mounted on P_4. The cavity mirrors (R=75 mm) are located at P_3 and P_4. The mirror at P_5 is mounted on a ring PZT. Aperture (P_1) and lens (P_2) aid with in-coupling. An aluminum housing (not shown) reduces air currents.

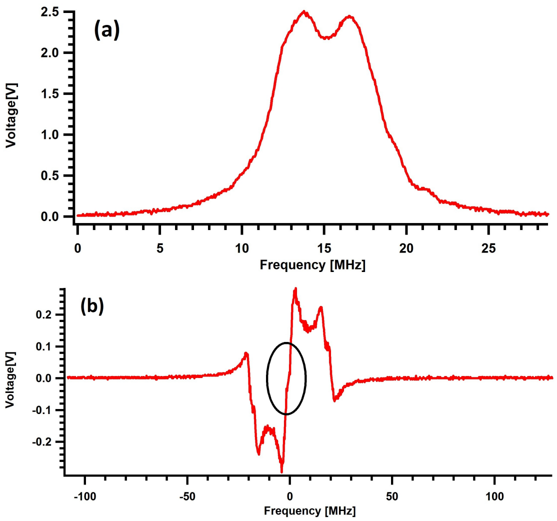

Figure 4.12: a) Double-peak transmission signal of the Fabry-perot cavity due to birefringence from the cavity mirrors. b) The effect of birefringence on the PDH error signal is visible as a reduced slope near the zero-crossing. Note that the horizontal scales are different in the two graphs.

beam through the cavity could be detected with a photo-diode. We moved the front mirror (M1) horizontally to change the length of the cavity until we could see some transmission peaks. We then tightened the mirror while making fine adjustments to the mirror position in order to obtain as close to a confocal condition as possible. While setting the cavity, we saw it was impossible to get a clean transmission peak. The problem was traced to birefringence from the mirrors, which caused two individual peaks separated by about 2.9 MHz to appear in place of a single transmitted peak (see Fig. 4.12). The double peaks that appear in both transmitted and reflected beams from the cavity distort the Pound-Drever-Hall error signal, as can be seen in Fig. 4.12(b).

The relative angular orientation and phase anisotropy of the two Fabry-Perot mirrors give rise to two different eigenstates of polarization in the cavity with non-degenerate frequencies [56]. The birefringence effect in the Fabry-Perot cavity is amplified by multiple reflections inside the cavity and enhances the frequency splitting between the two polarization eigenstates. The Fabry-Perot cavity effectively behaves like a waveplate. To measure the ellipticity of the light induced by the Fabry-Perot cavity, a half-wave plate is placed be-

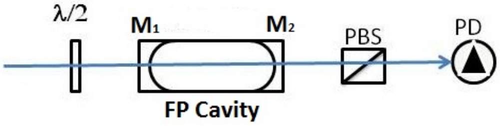

Figure 4.13: Setup for measuring the birefringence of the cavity mirrors.

fore the Fabry-Perot cavity to allow for different input polarization and a polarized beamsplitter with a photo-diode is placed after the cavity to analyze the output polarization (see Fig 4.13). We also mounted one of the mirrors of the cavity on a rotating mount to be able to change the relative angle orientation between the two mirrors. We varied the relative angle between the mirrors in 10° intervals from -170° to 170°. For each angle, the half-wave plate is changed to get the maximum and minimum transmitted intensities in one of PBS ports. From this we determine a contrast factor $\frac{I_{max}-I_{min}}{I_{max}+I_{min}}$.

The contrast factor versus the angle between the mirrors is plotted in Fig 4.14. It can be seen that the parameter takes values between 0.4 and 1. For the angles where $\frac{I_{max}-I_{min}}{I_{max}+I_{min}} \sim 1$, we get $I_{min} \sim 0$, meaning the birefringences of the two mirrors cancel each other (and they are close in magnitude). When the cavity 's birefringence is active, the polarization becomes elliptical and the contrast is spoiled.

From this data, we decided to set the cavity's mirror angle to 30° where $\frac{I_{max}-I_{min}}{I_{max}+I_{min}}$ is 0.99 and the birefringence effects of the mirrors nearly cancel. We changed the mirror's rotating mount to a fixed one while trying to keep the angular orientation between the mirrors constant, and then set the cavity to the confocal configuration to complete its construction.

To see the cavity transmission peaks, a high voltage needs to be applied on the cavity's piezo. An HP signal generator provides a triangular voltage signal with a frequency of 100 Hz and an amplitude of 10 V, which is converted to high voltage in a PID regulator module installed in the control rack of the 369.5-nm laser. The high voltage output is connected to the Fabry-Perot's piezo. The transmission peaks for the 739-nm beam are shown in Fig 4.15, where the coupling has been optimized to suppress the odd modes and to give a factor of 2 higher signal for the even ones. The ratio of even modes to odd modes is 94% to 6 %.

The transmission peaks for the 935-nm laser can be seen in Fig 4.16. The amplitude of the odd mode is so tiny that it cannot be seen in Fig 4.16(a). In Fig 4.16(b) the peaks

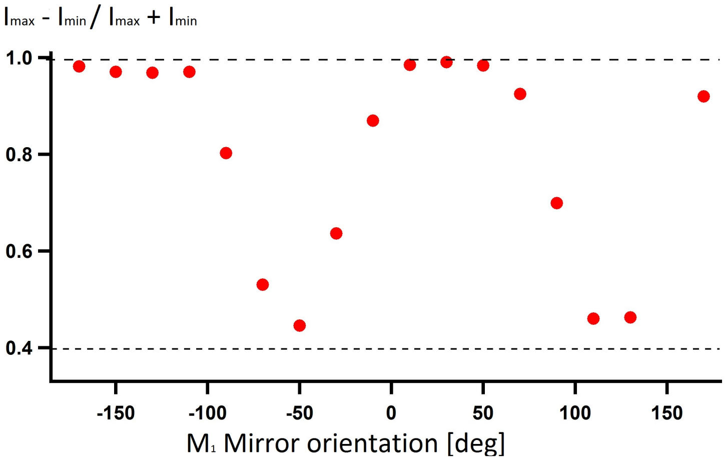

Figure 4.14: Transmission contrast factor versus Fabry-Perot's front mirror orientation. The parameter changes between 0.4 and 1. When the parameter is equal to 1, birefringence vanishes.

are magnified with an oscilloscope to be able to see suppressed odd modes. The amplitude ratio of even to odd modes is 99.5% to 0.5%, which is better than the transmission peaks for the 739-nm beam.

The transmission peaks can be used to measure the finesse of the cavity for each beam. Using Eq. (4.3), the theoretical non-confocal finesse of our cavity is $F_R = 1000$, which is the highest possible value assuming perfect mode matching. The maximum finesse that is achieved in practice with our Fabry-Perot cavity is 300, which was measured during the primary setup of the cavity for the 739 nm s TEM_{00} mode in a non-confocal configuration. This value is far less than the theoretical value, which can be explained by mis-alignment, absorption in the mirror, and diffractive losses.

The width of the 739-nm transmission peak in the confocal configuration is 8.1 MHz (see Fig. 4.17), and the finesse is calculated to be 250, using 2 GHz for the cavity's FSR.

In Fig. 4.17, we had magnified the signal with the oscilloscope, and it can be seen that the signal appears to be asymmetric. To find out if the asymmetry is due to the photodiode's time constant or to the cavity itself, we took another picture and decreased the ramp's amplitude applied on the cavity's piezo to zoom in on the signal. The transmission peak is plotted in Fig. 4.18. Although the signal looks less asymmetric compared to the one

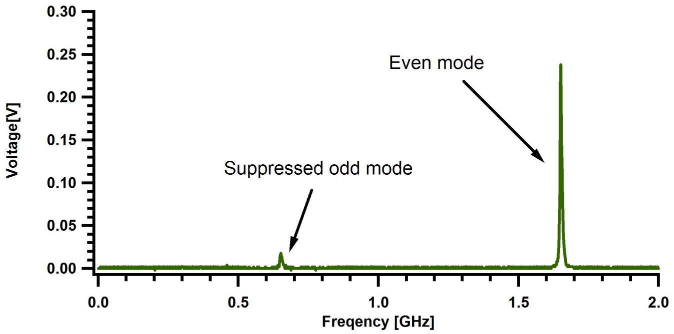

Figure 4.15: Even and odd transmission modes for the 739-nm beam where the odd modes are deliberately suppressed through optimization of the in-coupling. The amplitude ratio of the even to odd modes is 94% to 6%.

in Fig. 4.17, it is still slightly asymmetric, which is likely due to a slight deviation of the cavity from confocal in combination with poor mode matching. In any case, the transmission peak is sufficient for locking purposes. We also measured the finesse and transmission width of the Fabry-Perot cavity for the 935-nm laser. As can be seen in Fig 4.19, the width of the 935-nm laser's transmission peak is 6.3 MHz and the finesse is calculated to be 320. The finesse of the cavity at 935 nm is more than that at 739 nm, which shows that the 935-nm beam's alignment and mode matching are presumably slightly better. Also the transmitted peak does not have any asymmetry problem, which supports this conclusion.

4.3.5 Transfer-lock

The transfer-lock is made to prevent long-term drifts of the 935-nm laser. A sketch of the optical setup in Fig 4.20 shows the paths for both the 739-nm and 935-nm lasers into the Fabry-Perot transfer cavity. The 739-nm diagnostic beam out of the 369.5-nm laser is first split with the majority of power ($\sim$20 mW) sent to the iodine setup. The remainder of the power passes through a 50:50 beam-splitter that divides the power equally between the wavemeter and the transfer-lock setup . There is about 1 mW of 739-nm light sent to the lock setup. This beam, after some reflections, passes through a half-wave plate before going through a polarized beam-splitter (PBS) and quarter-wave plate (QWP). The combination of PBS and quarter-wave plate acts as an isolator to separate the reflected light from the cavity and to send it to a photo-diode. The quarter-wave plate is set to 52° to optimize the

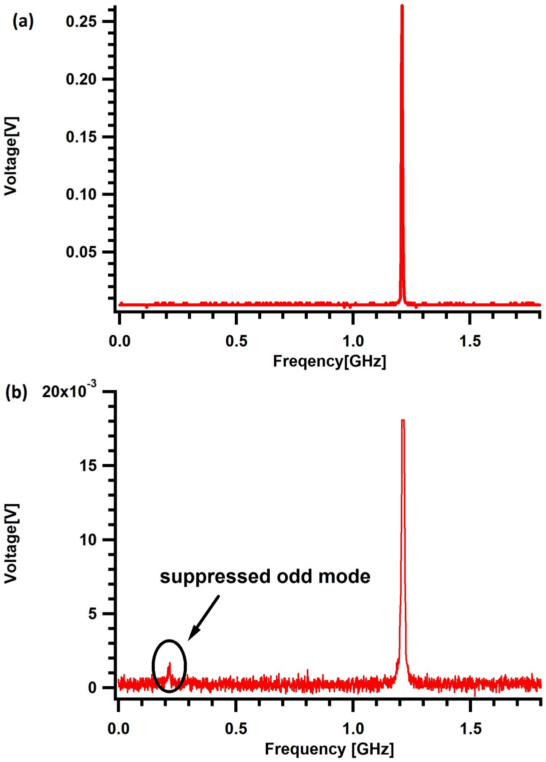

Figure 4.16: a) Even and odd transmission modes for the 935-nm beam. The odd mode is too small to be seen. The ratio of the even to odd modes is 99.5% to 0.5%. b) Zoom in with oscilloscope on the top picture to see the suppressed odd mode.

isolation. The beam out of the QWP reflects from a dichroic beam-splitter (DBS) and enters the cavity. The DBS coating is designed to reflect the 739-nm beam at 45° and transmit the 935-nm beam. The back side is AR coated for the 935-nm beam.

The 935-nm beam enters the transfer-lock setup through a PM fibre. The power of the beam out of the fibre is 2.5 mW. After a couple of reflections, the beam passes through a PBS and QWP in combination, designed to separate out the reflected beam from the cavity. There is no need for any HWP before the PBS because the fibre is oriented to obtain maximum transmission. The QWP is set to 55° to optimize the isolation. The beam out of the QWP is combined with the 739-nm beam at the DBS and enters the cavity.

We make use of both the transmitted and reflected beams from the Fabry-Perot cavity. Fast photo-diodes for the reflection are used to obtain the Pound-Drever-Hall signal while

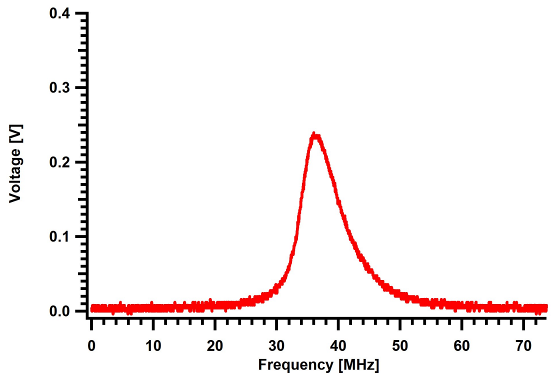

Figure 4.17: The even transmission mode of the 739-nm beam. We have magnified the peak with the oscilloscope. The peak's width is 8 MHz.

the transmitted beams are used for alignment and for re-lock circuits. The transmitted 739-nm and 935-nm beams out of the Fabry-Perot cavity need to be separated before they can be sent to separate monitor photo-diodes. The separation is done with a blazed diffraction grating with blaze wavelength of 750 nm. The grating has 1200 line/mm, so the distance between successive grooves is 833 nm. The grating is designed to have best efficiency when it is set at the Littrow angle (26°). At the Littrow angle, the incident and first order diffracted beams lie on top of each other. We measured 70% efficiency for the diffracted 739-nm beam when the grating was set to the Littrow angle (26°). However, the primary requirement is to obtain a clear separation between the two diffracted beams in order to send them to separate photo-diodes. The separation between the two diffracted beams is higher at lower incident angles, θ_i; therefore, we set the grating to $\theta_i = 15^\circ$ where we get 20° separation between the 739-nm and 935-nm diffracted beams. We still have 50% efficiency for the diffracted 739-nm beam, which is equivalent to around 300 μW power at the photo-diode, and 20% efficiency for the 935-nm beam, which gives 200 μW power at its photo-diode.

The separation of the 739-nm and 935-nm beams reflected from the cavity is performed by the DBS mentioned above. The 739-nm beam reflects from the beam-splitter. However, there is a small fraction of the 935-nm beam's reflection on the 739-nm's beam path; therefore, we use two BB1-EO2 mirrors from Thorlabs in the path that have a reduced reflectivity for the 935-nm beam. Almost all of the 935-nm reflected beam's power is

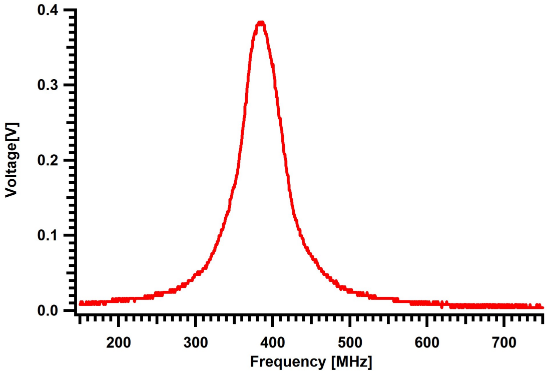

Figure 4.18: The even transmission mode of the 739-nm beam. The voltage of the ramp's amplitude on the piezo of the cavity is decreased to magnify the signal. We also have zoomed in on the peak with the IGOR software. The signal is less asymmetric compared to Fig 4.17.

dumped after these reflections, which suppresses the 935-nm light travelling back to the 739-nm laser. The reflected 739-nm beam, after reflection from the PBS, reaches another blazed diffraction grating, and the diffracted beam enters a photo-diode. We have used another grating here to suppress any leakage of the 935-nm beam to the photo-diode, which might cause cross talk between the lock signals.

The 935 nm power that is reflected from the cavity transmits through the DBS, is separated from the input path by a QWP-PBS isolator and reaches the photo-diode. There is no need for any diffraction grating before this photo-diode because the DBS strongly suppresses the transmission of any 739-nm beam into the 935-nm beam path.

The reflected 739-nm beam is used to lock the Fabry-Perot cavity to the 739-nm laser, and the reflected 935-nm beam is used to lock the 935-nm laser to the locked cavity. The signal from the fast photo-diode in the 739-nm reflected path goes to the input of a Pound-Drever-Hall demodulator (Toptica PDD110 module) installed in the electronic control rack of the 369.5-nm laser. The demodulator's output is a dispersive Pound-Drever-Hall lock signal, which is fed to a PID110 servo module for feedback to the transfer cavity's piezo-electric transducer. The PID110 module provides proportional-integral-differential control to optimize the lock of the cavity to the 739-nm laser. A separate input of the PID 110 comes from an external ramp-offset control circuit shown in Fig 4.21. The ramp-offset

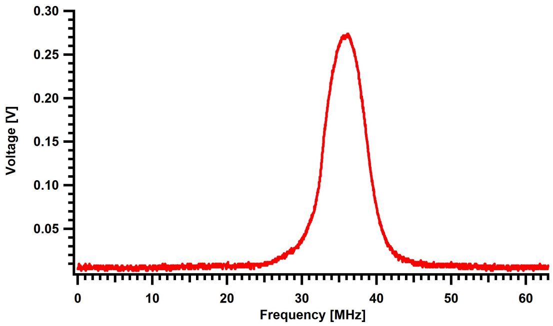

Figure 4.19: The even transmission mode for the 935-nm beam. The Fabry-Perot cavity's transmission width is 6.3 MHz

control gives the ability to scan and adjust the length of the transfer cavity via the PZT during locking. The maximum voltage output is 150 V, high enough to scan across ∼2-3 FSR's.

In Fig 4.22(a), the Pound-Drever-Hall lock signal is shown and has signal-to-noise ratio of 26. The horizontal axis is converted to frequency by using the fact that the zero crossings are separated by the PDH modulation frequency, which is 20 MHz. In Fig 4.22(b), the in-loop error signal is shown for the lock. The noise amplitude corresponds to a fractional 9% RMS noise, which corresponds to 0.5 MHz frequency excursion.

The signal from the photo-diode in the 935-nm reflection path goes to a PDD110 module installed in the electronic rack of the 935-nm laser, and the output error signal is sent to a PID110 module for feedback to the laser's piezo and to a FET control for laser-current feedback of the 935-nm laser. The 935-nm beam 's reflected power right before the fast photo-diode is 1.3 mW. In Fig 4.23(a), the Pound-Drever-Hall lock signal is shown and has a signal-to-noise ratio of 32. In Fig 4.23(b), the in-loop error signal is shown. The noise amplitude corresponds to a fractional 14% RMS noise, which corresponds to 1 MHz frequency excursion. Note that this noise is high-frequency and, in part, due to the PDH modulation.

Having discussed the lock setups in detail, the next step is to check how much locking improves the stability of the lasers.

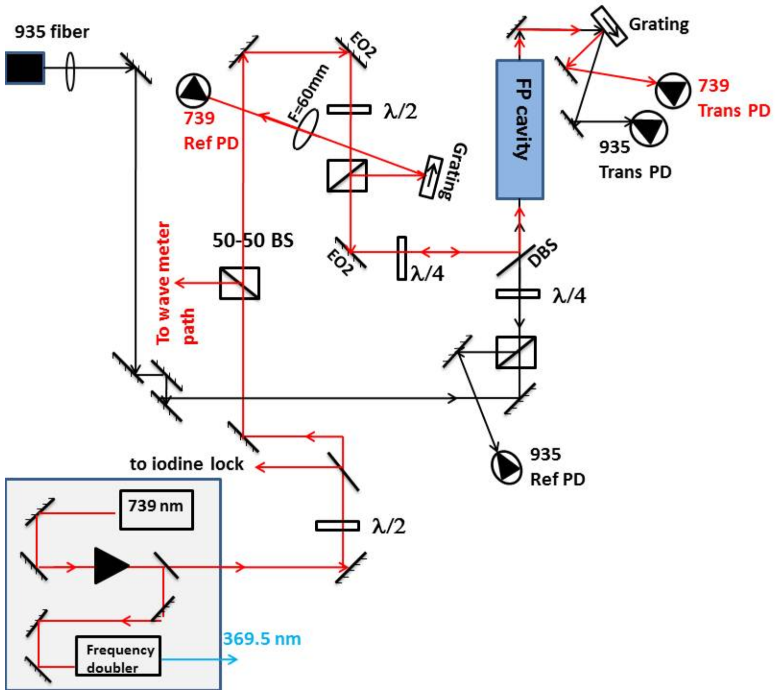

Figure 4.20: The paths of the 739-nm and 935-nm laser beams to the transfer cavity setup.

4.4 Tests of lock stability using a wavemeter

The simplest method for testing the stability of the lasers and laser locks described above uses our Bristol model-621 laser wavelength meter. Although this method has accuracy and precision limitations due to the wavelength meter, it still helps to study laser drifts over long times easily. The experiment is set up such that we can send any of the 399-nm, 739-nm and 935-nm lasers to the wavelength meter, as is shown in Fig 4.24. For each laser, we record the wavelength over a few hours with the Bristol control software to see how the wavelength drifts over time. The measurement rate is about 4 Hz and, according to the data sheet, the absolute accuracy of the wavemeter is 0.0002 nm at 1000 nm.

4.4.1 Wavelength drift of the 399-nm laser

The wavelength of the *unlocked* 399-nm laser was monitored over 2 hrs and the behavior is shown in Fig 4.25. The laser shows a drift of approximately 25 MHz/hr. For comparison,

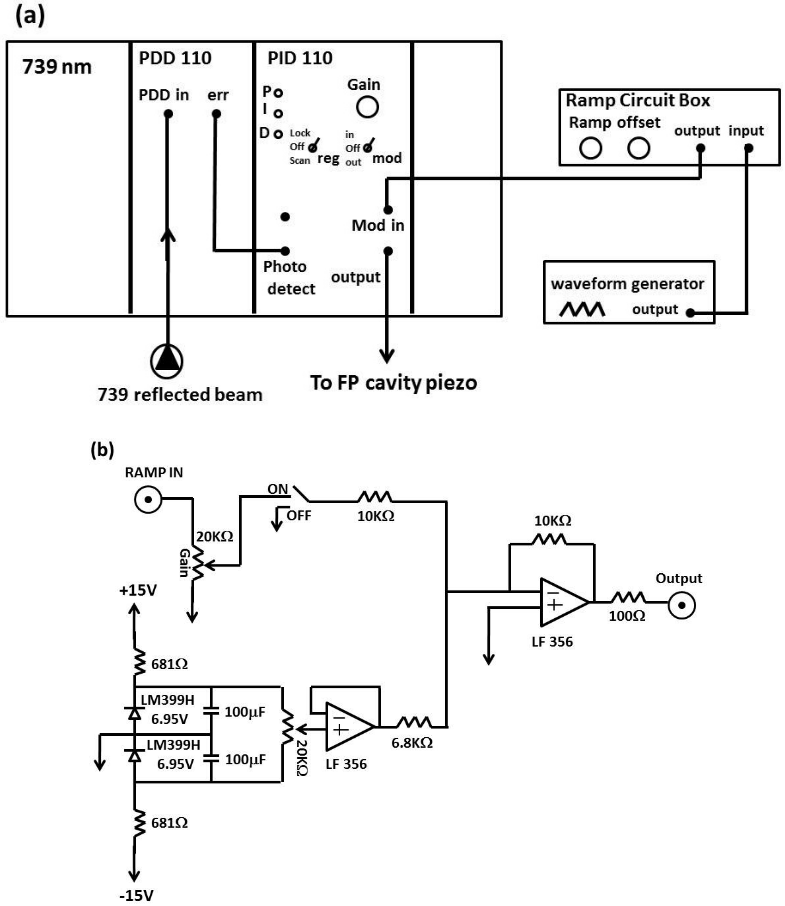

Figure 4.21: a) transfer-lock electrical setup. b) The circuit for the ramp circuit box, shown in (a).

the loading process, during which the photo-ionization beam is used, takes less than 10 min, and the resonances for different Yb isotopes are separated by a few hundred MHz [10]; hence, we so far have found no need to lock this laser. It is stable enough to obtain the selective photo-ionization we require.

4.4.2 Wavelength drift of the 739-nm laser

The wavelength of the 739-nm laser was monitored over 4 h, both when unlocked and when locked to iodine (see Fig 4.26). For both cases, the lock for the doubling cavity is

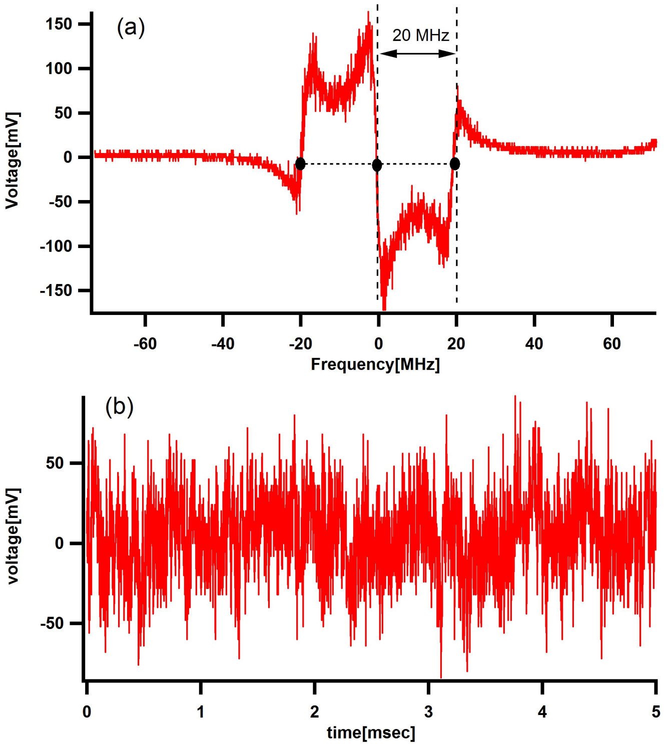

Figure 4.22: a) Pound-Drever-Hall lock signal versus frequency. The scan is performed by ramping the cavity length with a PZT and converting the ramp time to frequency using the known Pound-Drever-Hall modulation frequency. b) In-loop error signal versus time for the 935-nm laser locked to the Fabry-Perot cavity. The vertical axis has the same scaling as in (a).

also engaged to mimic actual experiment conditions. In the plots shown in Fig 4.26, there are 50 MHz point-to-point fluctuations and sudden changes in the fluctuations, but these are attributed to the wavelength meter itself. (The wavelength meter was repaired later, and the point-to-point fluctuations were improved). In any case, we are only concerned with long-term behaviour. As can be seen in Fig 4.26, the unlocked beam's drift is 0.0007 nm over 4 h, or 110 MHz/h. The case where the laser is locked to iodine is much more stable with a drift of at most 8.5 MHz over 4 h. This represents only an upper limit on the drift.

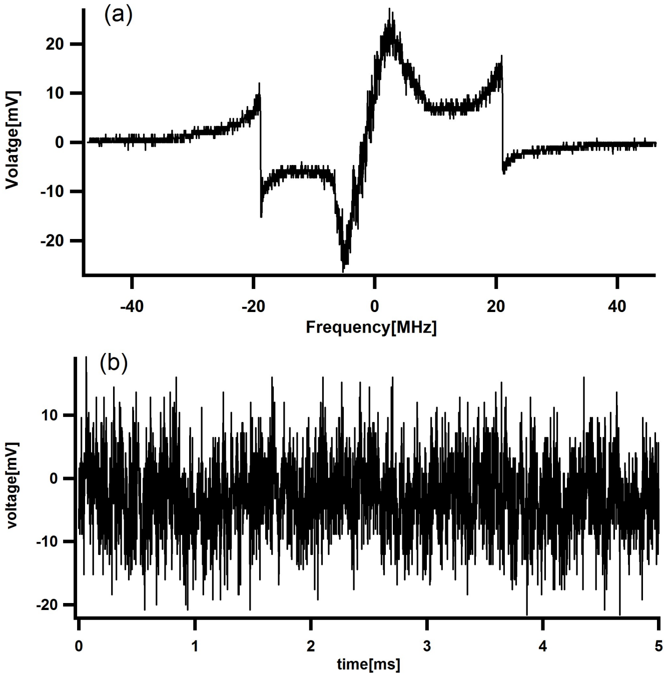

Figure 4.23: a) Frequency scan of the Pound-Drever-Hall lock signal for the 935-nm laser. The horizontal frequency scale is obtained by converting the cavity's length scan to frequency using the known FSR. b) In-loop error signal versus time. The vertical axis uses the same scale as (a)

4.4.3 Wavelength drift of the 935-nm laser

The wavelength of the 935-nm laser was monitored both when the laser was indirectly stabilized to iodine via the transfer-lock and when it was unlocked (see Fig 4.27). Because of laser-performance issues, the wavelength used for these tests is not the same as the ones required for Yb^+, but the general behaviour of the laser is expected to be the same. We also had problems maintaining the laser in single-mode operation for a long time during the measurements; hence, the unlocked case was only studied over about 1.5 h. The laser survived in a single mode for about 2.5 h for the locked case. In Fig 4.27, the locked case, with a drift of less than 10 MHz/h, is clearly more stable compared to the unlocked case, with a drift of about 95 MHz/h. There is a slight jump in the locked case after 1 h, which may be due to the wavemeter.

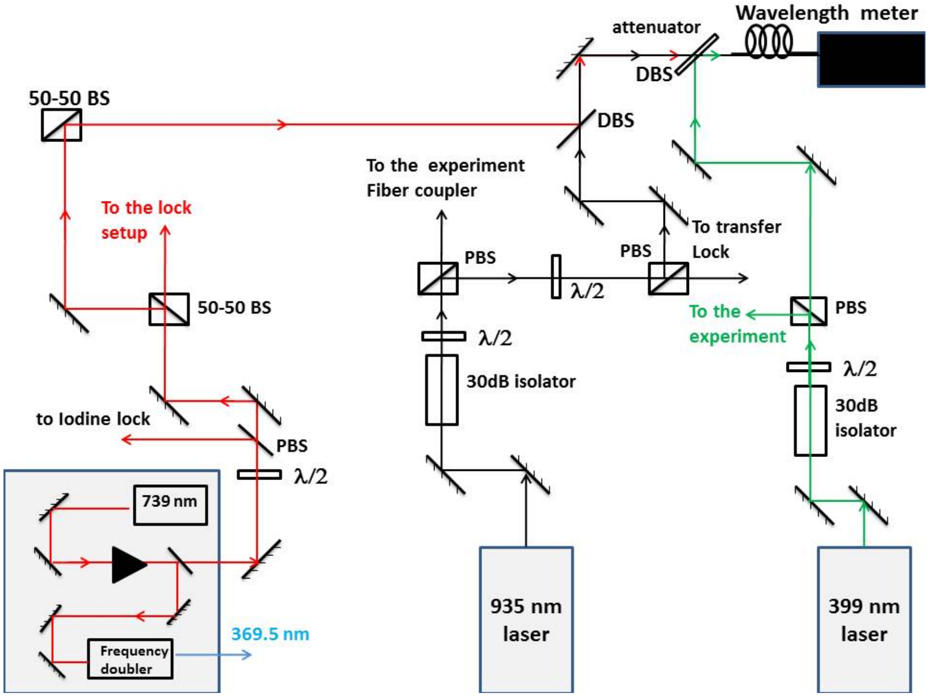

Figure 4.24: The optical paths of the 399nm, 739nm and 935nm beams to the wavemeter.

Ultimately, the 369.5-nm and 935 nm optical resonances of a trapped Yb$^+$ ion make for a better test of the wavelength stability of the lasers than the wavemeter-based tests discussed above. The ion resonance is stable, and the sensitivity to wavelength drifts is higher. We have monitored the lasers' wavelengths relative to their respective ion resonances over a few minutes, and the technique and results will be discussed in detail in the next chapter. In the next section, we conclude with a discussion of the effect of external environmental factors on the transfer-lock, and we use a trapped ion to measure the frequency drifts of the locked 935-nm laser in an attempt to relate the drifts to variations in the laboratory environment.

4.4.4 Stability of the transfer-lock versus environmental parameters

As explained above, the Fabry-Perot transfer cavity transfers the stability of the iodine-stabilized 739-nm laser (master laser) to the 935-nm laser (slave laser). Our Fabry-Perot cavity is not kept in vacuum; hence, the environment influences the performance of the

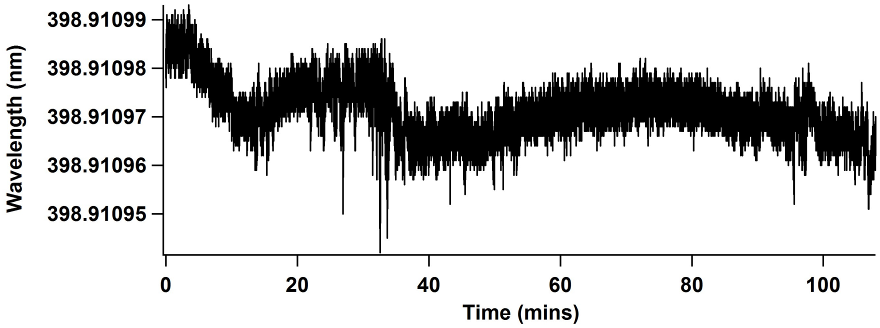

Figure 4.25: Passive stability check for the wavelength of the 399-nm laser, measured by the wavemeter.

lock. Fluctuations in external environmental factors like temperature, pressure and humidity change the index of refraction for air and lead to shifts in the resonances of the cavity. This is the ultimate limitation to the frequency stability of the transfer-lock [57]. If one of the environmental parameters, denoted in general by α changes by $\delta\alpha$, the frequency of the slave laser changes by

$$\delta\nu_s \approx \nu_s \frac{\delta\alpha}{\alpha}(n_m - n_s). \tag{4.5}$$

In the above equation, n_m and n_s are the indices of refraction of air for the master and slave laser. For $^{171}\text{Yb}^+$, for which the wavelengths in the transfer-lock setup are 739.0521 nm and 935.1879 nm, the indices of refraction for the master and slave wavelengths at 20 °C and 1 atm are, respectively, $n_m = 1 + 2.69262 \cdot 10^{-4}$ and $n_s = 1 + 2.70329 \cdot 10^{-4}$ [58]. Using Eq (4.5), the frequency change of the 935-nm laser due to pressure and temperature changes inside the transfer cavity are as follows:

$$\frac{\delta\nu_s}{\delta p} = \frac{342MHz}{760Torr} = 0.45\frac{MHz}{Torr} \tag{4.6}$$

$$\frac{\delta\nu_s}{\delta T} = \frac{342MHz}{293K} = -1.17\frac{MHz}{K} \tag{4.7}$$

According to the above equations, if the temperature changes by 2°C, the frequency of the locked 935-nm laser is expected to drift by $\sim$ 2.4 MHz. We have monitored the 935 nm resonance of single, trapped $^{171}\text{Yb}^+$ ion over a few minutes as a function of the lab temperature, recorded very roughly using the laboratory thermostat. The offset frequency of the 935-nm laser lock required to maintain the laser on resonance with the ion was found

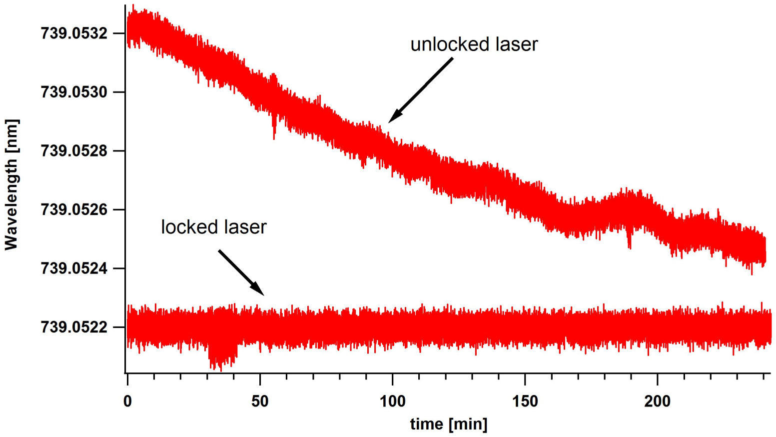

Figure 4.26: Stability check of the wavelength of the 739-nm laser, measured by a wavemeter when the laser is both unlocked and locked to iodine. In both cases, the laser is short-term stabilized to the frequency-doubling cavity.

to change as the room air conditioning cycled on and off. The offset frequency has been plotted as a function of laboratory temperature in Fig 4.28, and a clear linear correlation is apparent with a fit slope of -16 MHz/°C. The sensitivity is not what is expected from Eq. (4.7). Since we do not measure the cavity's temperature directly, it is possible that the fluctuations are larger than recorded using the laboratory thermostat. Further investigation will be undertaken in the future.

On a different day, we performed a similar experiment to monitor the 935-nm laser and the laboratory temperature, except the data was collected over a longer time of several hours. The results are shown in Fig 4.29. In this case, there is no obvious trend between the two plots. The offset frequency changes by 30 MHz over 3.5 hours. The change in frequency is, again, too large to be explained by Eq. (4.7), given the measured temperature variations. Furthermore, we do not expect there to be a pressure variation large enough to account for the drifts in laser frequency. One possible explanation is that there may be water resonances near our wavelengths causing enhanced fluctuations in the refractive index of air, or there may simply be some other technical issues that we have not yet found. In the mean time, we simply correct for the drift by adjusting the 935-nm lock-offset frequency on a regular basis during data runs.

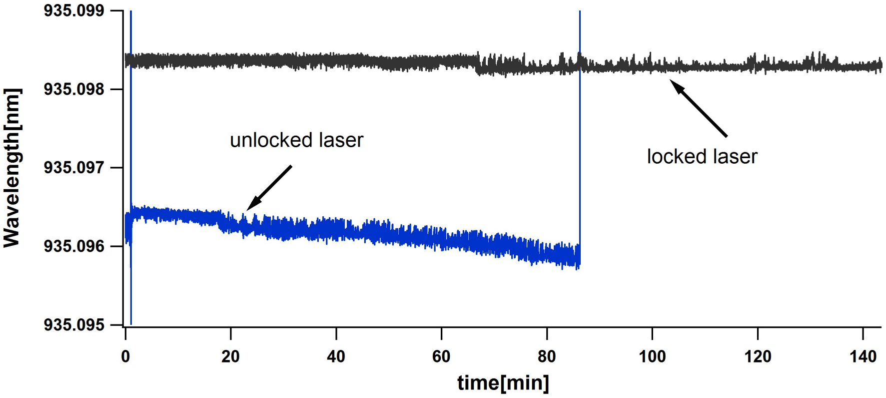

Figure 4.27: Stability check of the 935-nm laser 's wavelength, measured by the wavemeter, for both locked and unlocked cases. The lock consists of stabilization to the transfer cavity which is in turn locked to an iodine-stabilized 739-nm laser.

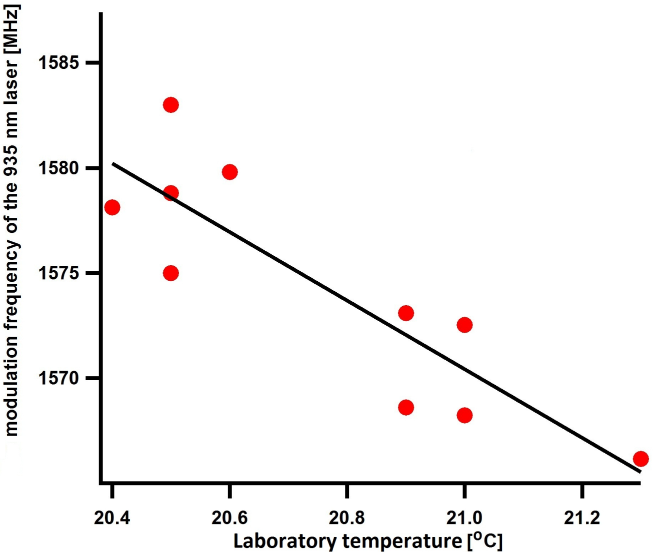

Figure 4.28: Lock-offset frequency for the 935-nm laser versus lab temperature over a few minutes. The lock-offset frequency is determined by comparison to a single trapped $^{171}\mathrm{Yb}^{+}$ ion.

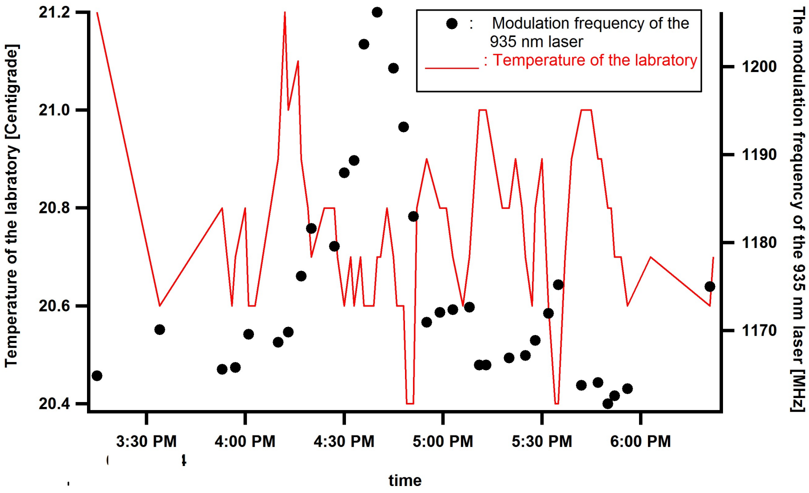

Figure 4.29: Laboratory temperature and the 935-nm laser's lock offset frequency over 3.5 h. The offset frequency is adjusted to maintain resonance with a trapped ^{171}Yb^{+} ion.

Chapter 5

Experimental results

In this chapter, the primary experimental results of this thesis are discussed. We start with the basic experimental procedure for loading single trapped ions with photo-ionization and then laser-cooling and detecting them. We also present some preliminary investigations into the isotopic selectivity of the photo-ionization loading in our setup. Next, as a natural extension of the offline laser-stability tests presented in the previous chapter, the stability of the two primary lasers required for fluorescence is assessed by monitoring the ion fluorescence in different lock situations over a few minutes. Following these technical tests, we proceed to measure the fluorescence of single trapped $^{171}\mathrm{Yb}^+$ and $^{174}\mathrm{Yb}^+$ ions and compare our results to the theory of Chapter 2. The measurements begin with a calibration of the magnetic field at the position of the trapped ion by measuring the induced Zeeman shift of $^{171}\mathrm{Yb}^+$ energy levels. We continue with a calibration of laser detuning and measurements of the linewidths for the UV transition of both $^{174}\mathrm{Yb}^+$ and $^{171}\mathrm{Yb}^+$. Finally, we study the effect of laser polarization, laser power and magnetic field on the fluorescence of both isotopes. The results in this chapter have also been published in [18].

5.1 Experimental procedure and summary of setups

Most of the experimental details have already been summarized in Chapter 3. We present here a brief description of the typical procedure and remind the reader of important essential details of the experiment.

Ytterbium Isotope	^{176}Yb	^{174}Yb	^{172}Yb	^{171}Yb
photo-ionization wavelength (nm)	398.9119	398.9115	398.9113	398.9111
detection-cooling wavelength (nm)	369.5261	369.5243	369.5250	369.5255
D state repump wavelength (nm)	935.1878	935.1874	935.1799	935.1724
F state repump wavelength (nm)	638.6101-638.6151		638.6185	

Table 5.1: Wavelengths of the photo-ionization, cooling, and repump lasers for different Ytterbium isotopes.

5.1.1 Loading, cooling and detecting single trapped Yb$^+$ ions

To load an Ytterbium ion of a given isotope, we first tune the 739-nm, 935-nm and 638-nm lasers to the corresponding wavelengths for that isotope according to Table 5.1 shown below [59]. We also choose the offset frequencies for the 739-nm iodine lock and the 935-nm transfer cavity lock in preparation for laser stabilization (see Table 5.1 and Chapter 4). If it is the start of the day, we will also optimize the 369.5-nm output power of the Toptica frequency doubler, and adjust all of the fibre couplings to maximize the laser power delivered to the experiment. During the loading procedure, we detune the 369.5-nm laser by a few hundred MHz below resonance to obtain a larger velocity capture range for the laser cooling. We also activate both the UV beams from the loading path and the detection path (see Fig 3.8 as well as the description of the paths in Chapter 3). The high power loading beam is counter-aligned with the 399-nm photo-ionization beam to obtain efficient two-color photo-ionization (see Chapter 3) and additional laser-cooling for the ions. In Fig 5.1, the paths of all four laser beams to the trap are shown.

After all the optimizations, we turn on the current to the Ytterbium oven and introduce the photo-ionization beam at full power. The CCD camera is run at maximum frame rate to provide a video-like monitor of the center of the trap. After a few minutes, the oven has warmed up sufficiently and ions will begin to load into the trap. The experiments explained later in this chapter focus on single ions. To load a single ion, we reduce the photo-ionization power to improve isotopic selectivity and to slow down the loading rate. If we are loading an even isotope with no coherent dark state on the UV transition, we can simply wait and look for a single ion to appear on the camera during the loading process. For ^{171}Yb^{+}, coherent population trapping suppresses the fluorescence at high powers; hence, in the simplest procedure, we need to reduce the UV power before checking if an ion has been loaded. (Alternative procedures currently in use will be described in a future thesis). As soon as we see a trapped ion on the CCD readout, we block the photo-ionization beam and turn off the oven to prevent further loading. We also turn off and block the 369.5-nm loading beam. The 369.5 detection and cooling beam is then set to reduced power and tuned close to resonance of the trapped ion. If the offset frequency of the Iodine lock has been correctly set up, the 739-nm fundamental will be simultaneously close to the Iodine absorption feature and can be locked to hold the laser stable. The transfer cavity is then locked to the 739-nm laser, and finally the 935-nm laser is locked to the transfer cavity.

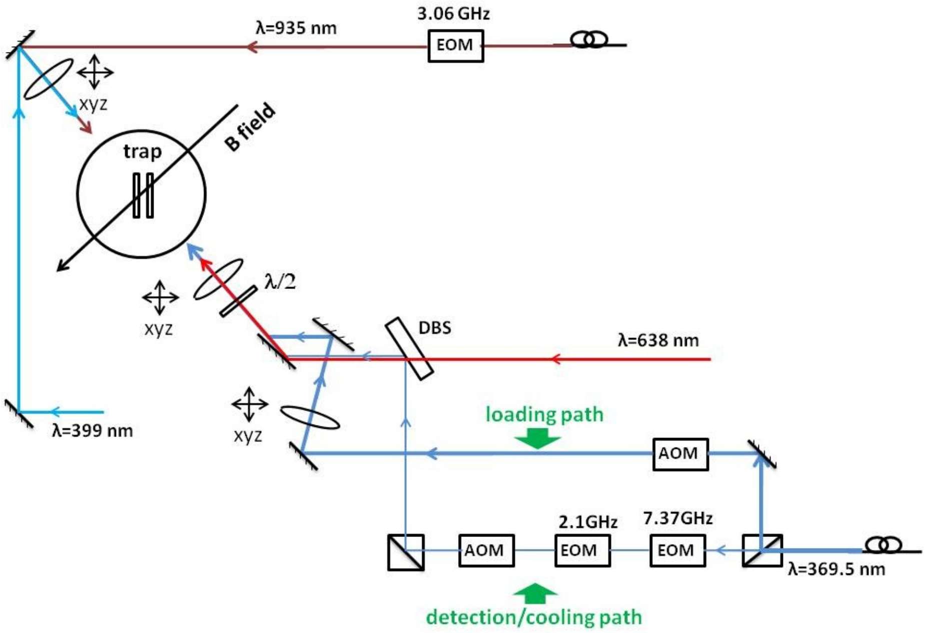

Figure 5.1: Simplified schematic of beam paths for the cooling/detection laser at 369.5-nm, D-state repump laser at 935-nm, and photoionsiation laser at 399 nm (reproduced from Chapter 3). The cooling/detection beam is divided into high power and low power paths. Both are used during loading; only the low power path is used during the experiment.

To load the ion, for each isotope we set the lasers to the corresponding wavelengths for that isotope according to the table shown below. We then optimize all the fibre couplings and laser powers. The next step is locking the bow-tie cavity to the 739-nm laser to get the maximum UV power out of the doubler. Atoms coming out of the oven are hot; hence, we blue detune the 739-nm (or equivalently the 369-nm laser beam) by a few hundred MHz for the loading process to get a more efficient cooling and capture range. We also let the UV beams from the loading path and the detection path reach the trap at the same time. The high power loading beam is counter aligned parallel with the photo-ionization beam to get good loading. In Fig 5.1, the paths of all four laser beams to the trap are shown. After all the optimizations, we turn on the oven and unblock the photo-ionization beam. Ions in the trap are monitored with the CCD camera during loading. All the experiments explained later in this chapter, have been done with single ions. We wait for a single ion to appear. If we are loading an even isotope with no coherent dark state, we can look for the single ion to appear on the camera during the loading process. For $^{171}\mathrm{Yb}^{+}$, CPT suppresses the fluorescence at high powers; hence, we need to reduce the UV power and check if any ion has appeared. As soon as we see the ion, we block the photo-ionization beam and turn off the oven to prevent further loading. We then block the UV beam from the loading path and start to lock the lasers. First the 739-nm laser is locked to the iodine on resonance. We then lock the transfer Fabry-Perot cavity to the locked 739-nm laser, and finally the 935-nm laser is locked to the transfer cavity. After locking the lasers, we make sure that the 369.5-nm and 935-nm beams are aligned properly on the ion by adjusting the focusing lenses (see Fig 5.1).

After locking the lasers, we optimize the alignment of the 369.5-nm and 935-nm beams on the ion by adjusting the focusing lenses mounted on XYZ translation stages (see Fig 5.1). The next step is to suppress the ion's excess micro-motion which broadens the linewidth of the transition [47]. Excess micro-motion arises when stray electric fields offset the ion is offset from the rf trap center. We wait for several minutes after loading to allow the trap and chamber to rethermalize and to allow for any rapid dissipation of surface charging to occur before checking the micro-motion. We use a standard photon-correlation technique to detect its presence of micro-motion [17], and minimize its effect on the cooling laser in real time by biasing the trap rods with dc voltages in the range of 0-100 mV.

5.1.2 After loading

Once trapped, ions are Doppler cooled on the ${}^2S_{1/2}(F=1)-{}^2P_{1/2}(F=0)$ transition by the 369.5-nm detection and cooling laser. The laser system produces about 4 mW of UV power and 2 mW of it is fibre-coupled to the experiment. The majority of the fibre-coupled beam goes to a path used during loading while about 200 μW is directed to the primary beam line used for laser cooling, optical pumping and fluorescence detection of the ions. The primary beam line (Fig 5.2) consists of two resonant electro-optic modulators (EOMs) at 2.1 and 7.37 GHz. The second side-band of the 7.37 GHz EOM is used to repump ${}^{171}\mathrm{Yb}^+$ out of the ${}^2S_{1/2}(F=0)$ to maintain steady-state fluorescence. The first sideband of the 2.1 GHz EOM can be activated to drive the optical pumping transition ${}^2S_{1/2}(F=1)-{}^2P_{1/2}(F=1)$ to initialize the ion to the $|{}^2S_{1/2};F=0,m=0\rangle$ state (see Fig 5.3). An 80 MHz acousto-optic modulator (AOM) provides fast control of the UV laser power incident on the ion. A maximum of roughly 60 μW reaches the trap where the laser beam's waist diameter is 60 μm.

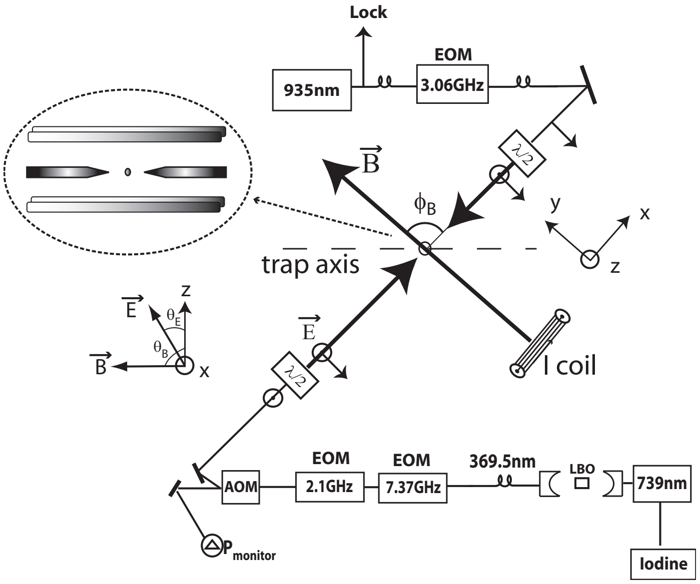

Figure 5.2: Schematic of essential experimental details for Doppler laser-cooling and fluorescence detection of trapped Yb^+ ions.

In order to keep the ion in the cooling and detection cycle, the stabilized external-cavity diode lasers at 935.2 nm and 638.6 nm are used to repump the ion from the metastable ${}^2D_{3/2}$

and $^2F_{7/2}$ states respectively. Roughly 2 mW of 638.6-nm laser power is overlapped with the 369.5-nm cooling beam and sent to the trap. Up to 3 mW of 935.2-nm laser power is delivered through an independent beam path (Fig 5.2) and focused to a beam waist diameter of 200 μm. The 935.2-nm beam is additionally frequency modulated with a broadband fibre modulator at 3.07 GHz to provide hyperfine repumping out of the $^2D_{3/2}(F=2)$ state. The 935.2-nm beam and modulation sidebands are left continuously on during the experiment, as is the 638.6-nm laser.

Additional specific details relevant to the ion fluorescence measurements are highlighted as follows:

Laser detuning control and stability - See Chapter 4. A broadband fibre EOM in the lock paths for both the 739.05-nm and 935.2-nm lasers allows each laser to be frequency tuned while locked.

Laser power control - The 80 MHz AOM in the 369.5-nm primary beam line is used to perform automated scanning of the laser power incident on the ion. Power calibrations of the AOM response using a photodiode power meter are done to limit day-to-day systematic errors in the power dependence of the ion's fluorescence to better than 10 %. The power calibration is made at the entrance to the vacuum chamber with only about 8% reduction at the ion expected due to reflection from the uncoated vacuum ports. The AOM's zeroth order is also used to monitor the UV power during data collection in order to correct for laser power drifts in subsequent analysis.

Polarization control - The polarization of the 369.5-nm and 935.2-nm beams are initially linearly polarized by polarizing beam splitter cubes. Zero-order quartz half-wave plates are used to adjust the polarization of each. The basic behavior of the UV half-wave plate in particular is verified off-line.

Photon collection - Scattered photons from a trapped ion are collected with an anti-reflection-coated UV microscope objective lens with high numerical aperture (NA≈ 0.23) and the image is relayed to a intensified CCD camera for diagnostic purposes, or to a photomultiplier tube (PMT) for measurement of the ion fluorescence by photon-counting. The net photon collection efficiency of the imaging system is about 3×10^{-3}. The PMT's detection efficiency is not spatially uniform. To suppress drifts in photon count rates, we check the position of the ion's image on the CCD camera consistently during the experiment and adjust the imaging system as needed. A pinhole is inserted at an intermediate image plane to suppress background scatter from the trap electrodes. A dichroic mirror is also used in the imaging optical path to suppress all except UV photons from reaching the camera and PMT. The 638.6-nm and 935.2-nm lasers do not appreciably contribute to the PMT background count rate.

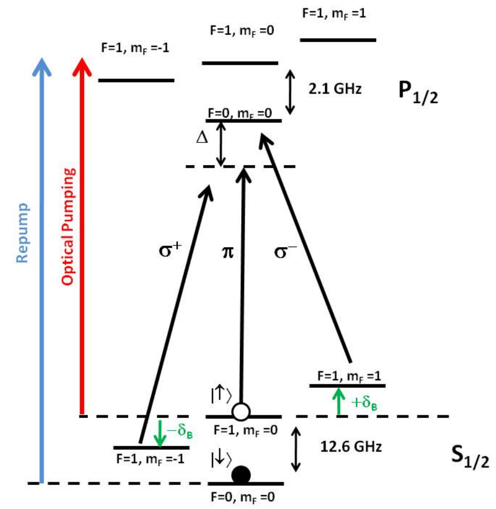

Figure 5.3: Zeeman levels of the $^{171}\mathrm{Yb}^{+}$ $^{2}S_{1/2}$ state. The optical pumping transition used for initializing the ion in the $j \neq i$ state and the repump transition used for maintaining the fluorescence are shown

Magnetic field- The magnetic field in the trap is generated by a single Helmholtz coil. Field homogeneity is not an issue since the trap and ion's position are essentially fixed relative to the coil. The magnetic field is arranged to be nominally along the y direction, orthogonal to the UV laser beam direction (see Fig 5.2).

Microwave transitions - A microwave horn delivers 12.6 GHz radiation to the trapping region in order to drive transitions between arbitrary hyperfine ground-states of $^{171}\mathrm{Yb}^{+}$. A typical Rabi frequency of 10-20 kHz is achieved using a 100 mW amplifier driven by an HP8672 synthesizer. The microwaves are used both for magnetic field calibration and for state preparation of the $|^{2}S_{1/2}; F = 0, m_F = 0\rangle$ qubit state. The latter procedure involves making a microwave π pulse after initialization of the $|^{2}S_{1/2}; F = 0, m = 0\rangle$ state.

Qubit detection - The ion's fluorescence can be used to detect the state of the hyperfine qubit via the standard technique of state-sensitive flurescence (see [60] and references therein.). Although this thesis does not include a detailed study of detection of the ^{171}Yb^{+} hyperfine qubit, the technique is used for the magnetic field calibration described later and so is mentioned here. The $^{2}S_{1/2}(F=0)$ to $^{2}P_{1/2}(F=1)$ transition is used for the detection with the hyperfine repump deactivated (see Fig 5.3). If the ion is initially prepared in the $|^{2}S_{1/2};F=0,m_F=0\rangle$ to $^{2}P_{1/2}(F=1)$; state, according to the selection rules, it is forbidden to go to the $^{2}P_{1/2}(F=0)$ state and it is 14.7 GHz away from the $^{2}P_{1/2}(F=1)$ state; hence, it scatters very few photons. On the other hand, if the ion is prepared in the $|^{2}S_{1/2};F=1,m_F=0\rangle$; state, then it is on resonance with the detection transition and scatters photons. Our group's detection studies of the^{171}Yb^{+} hyperfine qubit are discussed in [18] including limitations on the fidelity. See also [10, 11].

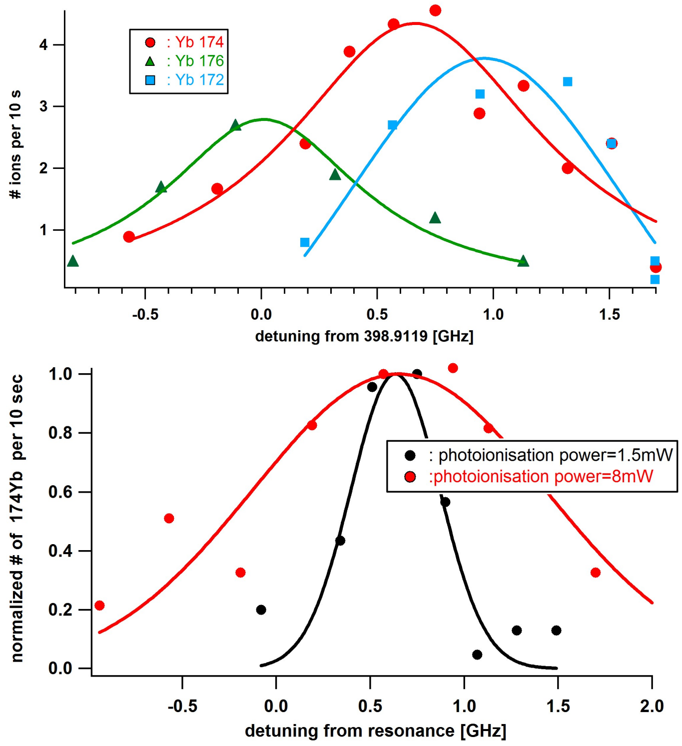

Figure 5.4: Top: photo-ionization resonances for even numbered isotopes of Yb at high photo-ionization intensity ($\sim$ 8 mW) . Bottom: Photo-ionization loading of ^{174}Yb^{+} at two different photo-ionization powers of 8mW and 1.5 mW. The actual rate of photo-ionization at 1.5 mW is slower; therefore, the two datasets have been normalized to their respective peak values. The beam waist in both cases is 60-100 μm.

Experiment pulse sequence - A typical experiment to acquire fluorescence of a trapped ion is run as a pulse sequence controlled by computer, although some of the steady-state fluorescence results presented later in the chapter are performed in stand-by mode. First we apply Doppler cooling for 2.6 ms, followed by a photon counting interval of upto or 10 ms to record the fluorescence. During the photon counting interval, automated control of the laser power permits scans of fluorescence as a function of laser power to be acquired. For each data point, the experiment sequence is repeated several times to average down the Poissonian counting noise. In more complicated experiments such as microwave spectroscopy of $^{171}\mathrm{Yb}^{+}$, the experiment sequence is somewhat different. The Doppler cooling stage is followed by optical pumping to initialize the ion to the $|^2S_{1/2}; F = 0, m = 0\rangle$ state and then a microwave pulse is applied. Finally, during the photon counting interval, a state-sensitive detection sequence is applied as described above.

5.2 Results

5.2.1 Selectivity of photo-ionization loading

During the summer after we had first trapped ions, we made a brief investigation of the photo-ionization selectivity. The first test was done for the even isotopes, ^{172}Yb, ^{174}Yb and ^{176}Yb, at full photo-ionization power of $\sim$8 mW. This provides fast loading but provides little selectivity. For each isotope, the wavelengths of the cooling/detection and repump lasers were set to the appropriate value for that isotope (Table 5.1). The photo-ionization wavelength was adjusted to different values using the wavemeter and, for each value, the number of ions loaded in a 10 s interval was counted using the CCD camera. The results are shown in Fig 5.4, plotted as a function of photo-ionization frequency relative to the neutral ^{176}Yb resonance. It can be seen that there are three overlapping resonances corresponding to the three even isotopes. The separation between peaks is of the order of 0.5 GHz, and match approximately the isotope shifts measured in [10]. The peak widths are about 1 GHz. Given that the photo-ionization beam has a waist size of 60-100 μm at the ion and that the saturation intensity for the $^1S_0$ to $^1P_1$ transition in neutral Ytterbium is 60 mW/cm^2, a photo-ionization power of $\sim$8 mW would give a power-broadened linewidth of 1-2 GHz (versus a natural linewidth of 30 MHz). This is close to the observed linewidths in Fig 5.4.

To study the effect of power broadening on the selectivity of the photo-ionization loading, we have measured the loading efficiency for $^{174}\mathrm{Yb}^{+}$ as a function of photo-ionization frequency at powers of 8 mW and 1.5 mW. The data is shown in Fig 5.4. The width of the loading resonance decreases roughly from 2 GHz to 0.7 GHz when we decrease the 399 nm power by a factor of 4, as might be expected from power broadening. Although decreasing the power reduces the loading rate, the selectivity for loading isotopes improves significantly. In practice, we attenuate the photo-ionization power yet further and use only 100 μW. To maintain a reasonable loading rate, we make use of 2-3 mW of 369.5-nm laser power at the same time to enable a presumed 2-colour loading process (see [10] and the discussion in chapter 3).

We have not studied the photo-ionization loading much beyond what has been presented above; however, it would be interesting to determine the minimum linewidth achievable for the photo-ionization features. Even though the photo-ionization laser crosses the atomic beam emitted by the Ytterbium oven nominally at right angles to minimize Doppler effects, the width of the linewidth is probably limited by Doppler broadening at low laser powers. Finally, it would also be interesting to study the dependence of the photo-ionzation rate on the 399-nm and 369.5-nm laser powers in order to elucidate the two-color photo-ionization process (see chapter 3).

5.2.2 Test of laser-lock stability with ions

To study the general behaviour of the laser and trap setup, we usually use a single $^{174}\mathrm{Yb}^{+}$ ion. It has the highest isotopic abundance and no coherent population trapping on the UV transition, both features making $^{174}\mathrm{Yb}^{+}$ easy to trap and work with. For this reason, we have investigated the stability of the 369.5-nm and 935-nm lasers using $^{174}\mathrm{Yb}^{+}$ ions. The previous chapter described offline studies of the stability using a wavemeter as a reference. The ultimate way, however, to check the stability of the lasers is to compare their frequency to the absorption resonance of a trapped ion. This technique was already used at the end of the previous chapter to study long-term drifts of the 935-nm transfer lock. We now show some additional data here that looks at shorter-term stability between 0.1 s and a few minutes.

We start with the 369.5-nm laser, whose fundamental wavelength at 739 nm is locked

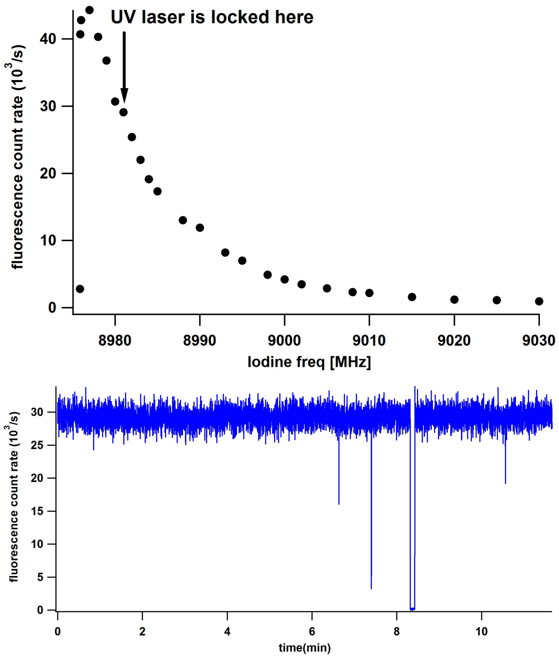

Figure 5.5: Top: PMT fluorescence counts versus iodine offset-lock frequency for the 369.5-nm $^2S_{1/2}$ to $^2P_{1/2}$ detection and cooling transition in a single trapped $^{174}\mathrm{Yb}^+$ ion. The fluorescence counts are acquired in 1 s. Note that a higher lock offset frequency corresponds to a lower laser frequency at the ion. Also note that the horizontal frequency scale should be doubled to obtain actual values at the ion since the 739-nm fundamental is locked to Iodine rather than the doubled 369.5-nm. Bottom: The ion's fluorescence as a function of time when the 369.5-nm laser is locked to the half-way point of the ion's resonance, as indicated in the top figure. The fluorescence counts are acquired in 1 ms, averaged 20 times.

to the Iodine saturation absorption setup. A broadband fibre-EOM in the lock path allows the laser to be frequency-tuned while locked. This is used to record the resonance profile of the $^2S_{1/2}$ to $^2P_{1/2}$ transition of a $^{174}\text{Yb}^+$ ion, as shown in Fig 5.5. The data is taken at a relatively low value of the laser power so as not to broaden the transition too much. We set the laser about halfway down the side of the resonance where the slope makes the fluorescence of the ion more sensitive to changes in the frequency of the laser. The ion is monitored over $\sim$11 min and, as can be seen in Fig 5.5, the fluorescence of the ion is reasonably stable. From the figure, it can be estimated that the 739-nm lock fluctuates less than 0.5 MHz, corresponding to 1 MHz in the UV, over 11 min. This is an upper limit that does not account for fluctuations in the power of the laser or Poissonian noise in the photon counting.

We have also studied the stability of the 935-nm laser using a similar procedure. A broadband fibre EOM in the 935-nm lock path also allows this laser to be frequency-tuned while locked. We first measure the resonance of the $^2D_{3/2} - ^3D[3/2]_{1/2}$ transition at low laser power ($\sim$1-10 μW) by changing the fibre-modulator frequency (see Fig 5.6). The measured full width at half maximum is about 10 MHz. We then lock the laser to the halfway point with the steepest slope and monitor how the fluorescence of the ion changes over $\sim$5 min. Figure 5.6 shows a worst scenario. For comparison, we also lock the laser to the top of resonance and record the fluorescence of the ion for the same time interval. This data is also shown in Fig 5.6. It can clearly be seen that the data on the side of resonance fluctuates much more (on a time scale of a few minutes) compared to the data at the top of resonance; therefore, the observed drift is attributed to frequency noise. Given the relatively quiet resonance measurement shown in Fig 5.6, it appears that the magnitude of the drifts vary over time. We have not yet determined the cause for certain; however, we are not limited by frequency drifts in the 935-nm laser in our fluorescence studies. Firstly, we use 2-3 mW of 935-nm power at the trap during the experiment, which broadens the repump transition and greatly reduces its sensitivity to laser frequency changes. Second, we also monitor the repump resonance every few minutes during data collection and adjust the lock offset frequency as required.

5.3 Studies of single-ion fluorescence

In the following experiments we study the fluorescence behavior of the $^{171}\text{Yb}^+$ and $^{174}\text{Yb}^+$ isotopes as a function of magnetic field, laser power, polarization, and detuning. These parameters are all calibrated *in situ* with the exception of laser power, and at reasonably low error to suppress the effect of parameter correlations in fits to theory. For each section, we start with simpler $^{174}\text{Yb}^+$ isotope, chosen as a "control" ion for comparison since it is free of hyperfine structure and does not have coherent population trapping on its main fluorescence transition. We then proceed to single, trapped $^{171}\text{Yb}^+$ ions, which we intend for use as hyperfine qubits. For each isotope, we compare our results with the theory presented in Chapter 2.

5.3.1 Magnetic field calibration

The magnetic field strength at the trap is calibrated using microwave spectroscopy of the $^{171}\text{Yb}^+$ hyperfine ground-state. Resonances of all three microwave Zeeman transitions $|^2S_{1/2}, F=0, m_F=0\rangle \to |^2S_{1/2}, F=1, m_F=0,\pm1\rangle$ are measured to extract the Zeeman shift between the $F=1$ sub-levels as a function of magnetic bias coil current I_{coil}. The measurement cycle begins with a 2.6 ms period of Doppler cooling, followed by optical pumping for 0.3 ms to prepare the ion in the $|^2S_{1/2}, F=0, m_F=0\rangle$ state. A microwave pulse close to a π pulse is applied, and state-selective fluorescence detection is used to probe the population transfer as a function of microwave frequency. The frequency is scanned in 1 kHz steps to obtain a Rabi lineshape, which is fit for resonance location. The measurement cycle is repeated 50 times to average detection noise. At each bias coil current, UV laser power and detection time (0.4-4 ms) are adjusted to optimize the state detection efficiency.

The Zeeman-shifted resonances obtained for all three hyperfine transitions are plotted as a function of bias coil current in Fig 5.7. The magnetic field dependence of the resonances are fit to the Breit-Rabi theory together with a parametrization of both current-dependent and static-background magnetic fields. Resonance at zero magnetic field is inferred from the fit to be near 12642.81 MHz. We extract a coil-dependent linear Zeeman shift of 3.991(2) MHz/A corresponding to a magnetic field calibration dB/dI=2.851(1) G/A. Although the fit includes the quadratic Zeeman effect, we ignore it in further analysis, which constitutes an error of only 20 kHz at the largest currents considered. A non-zero

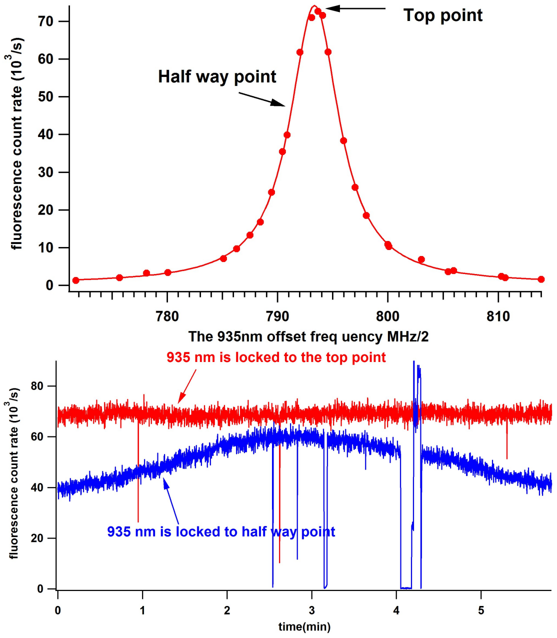

Figure 5.6: Top: PMT fluorescence counts versus iodine offset-lock frequency for the 935-nm $^2D_{3/2}$ to $^3D[3/2]_{1/2}$ repump transition in a single trapped $^{174}\mathrm{Yb}^+$ ion. The fluorescence counts are acquired in 1 s. Note that the actual offset frequency is a factor of 2 larger than the horizontal scale shown, due to an rf doubler used in the setup. Bottom: The ion's fluorescence as a function of time when the 935-nm laser is locked to the top of the repump resonance (red) or to the half-way point (blue). The fluorescence counts are acquired in 1 ms, averaged 20 times.

minimum Zeeman shift of δ_B=0.952(7) MHz occurs at a value of $I_{coil} = -0.343(1)$ A, which indicates a residual static background field of 0.98 G parallel and 0.68 G transverse to the coil. The static background field is due to magnets in optical posts around the trap and earth's magnetic field, and is largely stable over the course of days and longer (better than 100 kHz drift) so we simply incorporate it into our calibration. The majority of the fluorescence data is taken over coil currents in the range 0.8-2.5 A where the coil field dominates and the magnetic field changes only slightly in direction due to the background. Common values of coil current used are {0.805 A, 1.695 A, 2.505 A} corresponding to $\delta_B/2\pi$ ={4.68 MHz, 8.19 MHz, 11.41 MHz}.

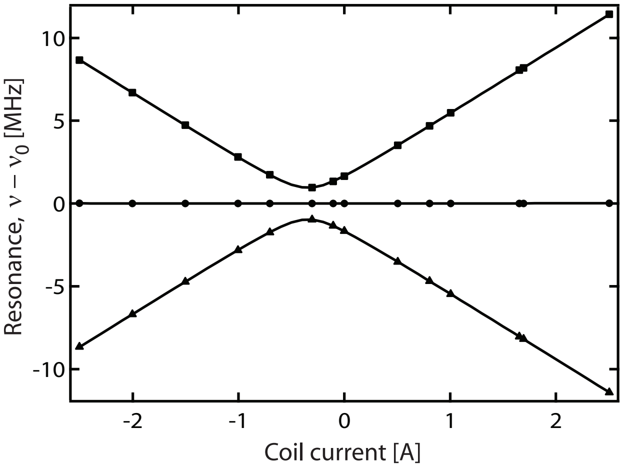

Figure 5.7: Calibration of the magnetic field at the trapped ion's location using microwave spectroscopy of $^{171}\text{Yb}^{+}$. Shown are measured transitions from the ground hyperfine state $|F = 0, m_F = 0\rangle$ to $|F = 1, m_F = -1\rangle$ (triangles), $|F = 1, m_F = 0\rangle$ (circles), and $|F = 1, m_F = +1\rangle$ (squares) as a function of bias coil current I_{coil}. The vertical axis is referenced to the inferred resonance frequency $\nu_0 = 12642.8$ MHz at zero magnetic field. Solid lines are a fit to Breit-Rabi theory with three magnetic-field parameters, (i) current-dependent Zeeman shift 3.991(2) MHz/A corresponding to dB/dI=2.851(1) G/A, (ii) offset current $I_o = -0.344(1)$ A and (iii) minimum Zeeman splitting 0.952(7) MHz. The last two parameters characterize a constant background field of about 1 G. The fit lines match the data to ±10 kHz.

5.3.2 Yb^+ resonance, Linewidth

Modeling the ion's fluorescence behaviour relies on a reasonably accurate calibration of laser detuning. Measuring the resonances for $^{174}\mathrm{Yb}^+$ and $^{171}\mathrm{Yb}^+$ provides the detuning calibration for these two isotopes and allows us to check the linewidth. We start with measuring the $^{174}\mathrm{Yb}^+$ resonance. This isotope is used to study the linewidth carefully in different ways. After that, for $^{171}\mathrm{Yb}^+$, we use only the simplest method primarily determine resonance.

$^{174}\mathrm{Yb}^+$ resonance

The location of the primary 369.5-nm UV transition for $^{174}\mathrm{Yb}^+$ is verified using a Zeeman shift $\delta_B/2\pi$ =8.19 MHz, near-optimal polarization angle $\theta_{BE} = 2.8°$ and a relatively low laser power of 0.83 μW ($s_0 = 0.63$). The frequency-doubled 369.5-nm laser frequency is scanned by tuning the Iodine lock offset frequency of the 739-nm fundamental. The fluorescence counts, recorded in a 10 ms interval and averaged ten times, are plotted as a function of UV laser frequency in Fig 5.8(a). The scan starts below resonance and proceeds up to and past the resonance position. Because of the mechanical effects of the laser scattering, the trapped ion is heated on the high side of resonance, and is effectively Doppler shifted off resonance. This results in a characteristic half-lineshape [61] where the standard procedure is to identify the drop-out as resonance. The background-subtracted data is fit to a Lorentzian lineshape with an exponential suppression above resonance. The fit gives a lock offset frequency on resonance of $\nu_{0,174}$=8975.8(1) MHz, which corresponds to a fundamental wavelength of approximately 739.0499(1) nm as determined by a wavemeter [62]. Besides resonance location, the fit provides a linewidth of 24.6(1) MHz and an inferred natural linewidth of 20.0(1) MHz. This value, which is within 2% of 19.60 MHz, is sensitive to errors in laser power determination and ignores technical broadening such as that due to laser linewidth.

To verify that there is nothing pathological in the half-resonance curve, we have performed a control experiment where a simultaneously trapped $^{172}\mathrm{Yb}^+$ ion is used to sympathetically cool the $^{174}\mathrm{Yb}^+$ ion [63] while its resonance is scanned. The cooling allows the full resonance shape to be obtained [63, 64]. A separate UV laser system is used to provide Doppler cooling of the $^{172}\mathrm{Yb}^+$ isotope, whose resonance is 1.2 GHz blue-detuned

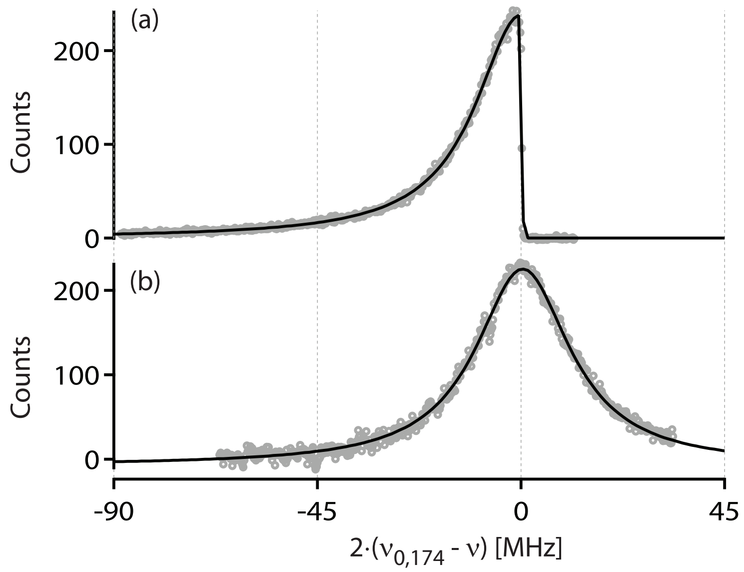

Figure 5.8: (a) Scan of UV laser frequency to locate resonance of a single trapped ^{174}Yb^{+} ion. The frequency-doubled laser is scanned with the fundamental locked to iodine by tuning lock offset-frequency ν. The parameters for the scan are $\delta_B/2\pi = 8.19$ MHz, $\theta_{BE} = 2.8^{\circ}$ and saturation parameter $s_0 = 0.63$. The solid line is a fit to a Lorentzian with exponential suppression above resonance. The fit yields a resonance location $\nu_{0,174}$=8975.8(1) MHz and a linewidth of 24.6(1) MHz including all broadening terms. The horizontal axis is offset and scaled using the fit value of $\nu_{0,171}$ to indicate UV detuning. (b) Scan of UV laser frequency to locate resonance of ^{174}Yb^{+} in presence of sympathetic cooling by a simultaneously trapped ^{172}Yb^{+} ion. The horizontal scale for the scan has been shifted by 2 MHz to account for a measured ac Stark shift from the ^{172}Yb^{+} cooling laser. The other parameters are similar to (a). The fited resonance position is slightly shifted 0.39(5) MHz relative to the resonance in (a), which is attributed to systematic error in ac Stark shift determination. The fited linewidth is 25.5(2) MHz. The fit includes a baseline -7.6(6).

from $^{174}\mathrm{Yb}^{+}$. The additional $^{2}D_{3/2} - {}^{3}D[3/2]_{1/2}$ repump frequency for $^{172}\mathrm{Yb}^{+}$ is easily obtained by adding a modulation sideband of 2.56 GHz to the 935.2-nm laser using the pre-existing fibre modulator. The 638.6-nm laser is continuously scanned at a slow rate to ensure it covers both isotopic resonances. The majority of fluorescence from the $^{172}\mathrm{Yb}^{+}$ ion is blocked from reaching the PMT at an intermediate image plane in the imaging system and the remainder is subtracted as a background from the $^{174}\mathrm{Yb}^{+}$ fluorescence signal of interest.

The resonance scan of $^{174}\mathrm{Yb}^{+}$ in the presence of sympathetic cooling is shown in Fig 5.8(b). The data have been corrected for the residual background. Additionally, an offset of $+2$ MHz is applied to the horizontal frequency scale to account for the ac Stark shift due to the $^{172}\mathrm{Yb}^{+}$ cooling beam. The value of the ac Stark correction was estimated in a separate measurement. The data have been fit to a Lorentzian lineshape, which gives a UV resonance frequency slightly shifted 0.39(5) MHz relative to that of the single ion shown in Fig 5.8(a). The resonance shift is within the bounds of the systematic error of the ac Stark shift estimation. In any case it is at least clear that there is nothing grossly wrong with using the drop-out point of a single trapped ion to determine resonance. The Lorentzian fit also gives a linewidth of 25.5(2) MHz, and an inferred natural linewidth of 20.9(2) MHz.

We do not correct the fluorescence theory for any extra broadening effects outside of the theoretical expressions presented in Eqs. (2.31) and (2.32). The largest correction is probably due to the laser linewidth. The absorption linewidths from all the resonance scans presented have given inferred natural linewidths within 5% of the previously published value of 19.6 MHz [11]; however, the scans are done at fixed magnetic field and laser power and require correction for Zeeman and saturation broadening to reveal any remaining effects. We have done a more careful experiment to remove the saturation broadening and to constrain the size of any systematic effects such as laser linewidth. We perform relatively fast scans of laser power at several values of detuning to extract the resonance profile for the fluorescence. The laser power for each scan is scaled to correct for slow drifts. The laser sidebands required for hyperfine repump of $^{171}\mathrm{Yb}^{+}$ are also kept active. They are far off resonant and have no appreciable effect, but by having them active for $^{174}\mathrm{Yb}^{+}$ studies also, we are able to compare saturation powers directly between the two isotopes without correction. The data is collected at a fixed magnetic field corresponding to $\delta_B/2\pi = 8.19$ MHz and a polarization angle $\theta_{BE} = 2.8^\circ$.

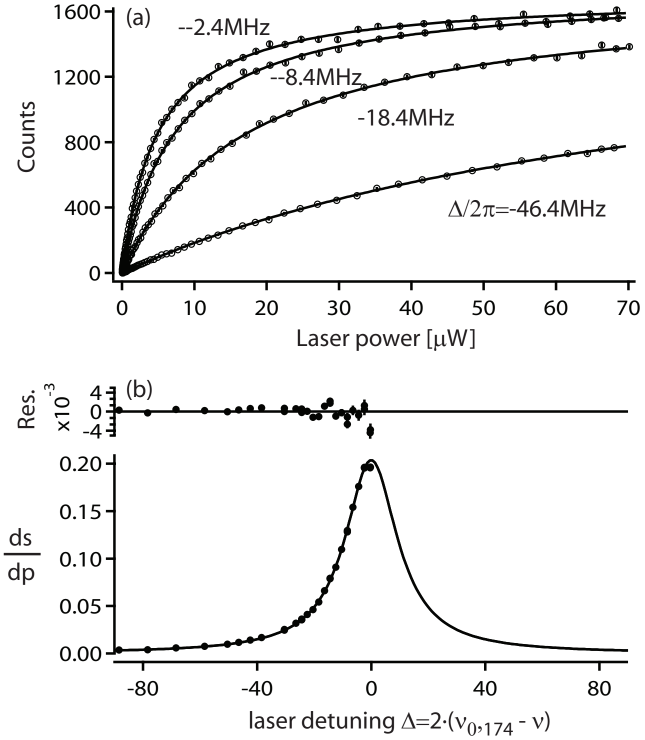

Figure 5.9: ^{174}Yb^{+} resonance extracted from laser power scans at $\delta_B/2\pi = 8.19$ MHz and $\theta_{BE} = 2.8^\circ$. (a) Counts in 10ms, averaged 10 times, are shown as a function of 369.5-nm laser power at the range of detunings indicated. Detunings are determined from the resonance location as shown in Fig 5.8. Each line is a separate weighted fit to a scan at a given detuning. The fit function is a general saturation form (see text) with two fit parameters, amplitude coefficient and saturation-related factor ds/dp. (b) Plot of fit values ds/dp obtained as a function of laser detuning. The line is an unweighted fit to Eq.(2.32) with fixed zero baseline and fixed resonance position. Two points near the peak are excluded (see text). Residuals shown above main plot. The natural linewidth from the fit is $\gamma/2\pi = 19.6(1)$ MHz and saturation power is $p_{sat} = 1.25(1)$ μW.

Laser power scans of ^{174}Yb$^+$ fluorescence, corrected for background, are shown in Fig 5.9(a) for a selection of laser detunings. The fluorescence counts are acquired for 10 ms and averaged 10 times. The analysis makes use of the fact that ^{174}Yb$^+$ data should fit to a general saturation form with repump correction. Each laser power scan at a given detuning is fit to the following equation which includes the 935.2 nm repump factor ξ explicitly:

$$\eta\gamma\mathcal{P}_p = \mathcal{A}\cdot\left(\frac{s}{1+(1+\xi/2)s}\right). \tag{5.1}$$

The free fit parameters are an amplitude coefficient $\mathcal{A}$ and a proportionality constant ds/dp linking the laser power p to the generalized saturation parameter $s = (ds/dp)\cdot p$. The repump factor, estimated from separate measurements, is fixed at a value of 0.1. The general form of the equation should still apply for finite laser linewidth with modification to the linewidth and saturation power [65]. Errors used for fit weighting, determined from repeated measurements, are Poissonian with an additional 2% fractional noise before averaging. Reduced χ^2 for the fits are generally good, on average 1.0(2) for 66 degrees of freedom, except for the two detuning values nearest resonance where the trapped ion becomes motionally unstable at high powers. The fit amplitude coefficients are roughly constant over the range of detunings shown. At larger detunings fitting difficulties and correlations of the fit parameters become significant.

The saturation factors ds/dp obtained from the individual fits are plotted as a function of detuning in Fig 5.9(b). An unweighted fit to the data is made using the following Lorentzian form obtained from Eq.(2.32):

$$\frac{ds}{dp} = \frac{1}{3}\frac{1}{p_{sat}}\frac{\gamma^2}{(\Gamma_{174}(\Omega=0))^2+4\Delta^2}. \tag{5.2}$$

where p_{sat} is a saturation power and the linewidth $\Gamma_{174}(\Omega=0)$ only includes the Zeeman broadening. Although Eq. (2.32) and by extension Eq. (5.2) are derived as an approximation in general at finite magnetic field, the functional form is correct for the special case of π-polarization ($\theta_{BE}\approx 0^\circ$) considered here. The fit uses only two free parameters, p_{sat} and the natural linewidth γ. Resonance location, determined as shown in Fig 5.8, is held fixed. Excluding the two data points closest to resonance that show excess noise in fluorescence scans, the fit provides parameters $p_{sat} = 1.25(1)$ μW and $\gamma/2\pi = 19.6(1)$ MHz. If the points at the peak are included, these values change to 1.28(1) μW and 20.1(2) MHz respectively. The values of the inferred natural linewidth match reasonably well with the previously published value of 19.6 MHz [11] to about the 5% level. Given this level, we simply use the previously published value of the natural linewidth in our analysis and leave any additional broadening effect as a potential systematic error in our results.

^{171}Yb$^+$ resonance

A laser frequency scan to locate the drop-point as the resonance of a single trapped $^{171}\mathrm{Yb}^+$ ion is shown in Fig 5.10, performed in the same way as described for $^{174}\mathrm{Yb}^+$. Scan parameters include a Zeeman shift $\delta_B/2\pi = 8.19$ MHz, optimal polarization angle $\theta_{BE} = 57.5°$, and a relatively low UV laser power. As before, the frequency-doubled 369.5-nm laser is scanned with the fundamental locked to iodine by tuning the lock offset-frequency. The data is fit to a Lorentzian lineshape with an exponential suppression above resonance. The fit resonance location for $^{171}\mathrm{Yb}^+$ is at a lock offset frequency $\nu_{0,171} = 10193.00(5)$ MHz which includes various AOM offsets and corresponds to a fundamental laser wavelength of approximately $739.0520(1)$ nm as determined by a wavemeter [62]. The value of $\nu_{0,171}$ is stable to 0.1 MHz or better over several weeks.

The residuals in Fig 5.10 demonstrate that there is no substantial distortion from a Lorentzian line shape. Micromotion is nulled to a level where the residual effect might only be a slight broadening. Doppler broadening is complicated by variation in the laser's cooling effect with detuning below resonance; however, at our level of precision, the overall correction to the lineshape should amount to a small, if not negligible, increase in the width [61]. The fit linewidth of 24.6(2) MHz combined with calibrations of Zeeman splitting, polarization, and power saturation parameter s_0=1.590(4) gives an inferred natural linewidth, ignoring other broadening effects, of 20.1(2) MHz. The fit linewidth is susceptible to systematics associated with the half-resonance and with points at the peak where the ion begins to decrystallize. A Lorentzian fit to data 1 MHz below resonance with the resonance location fixed gives a slightly lower linewidth 24.3(1) MHz and inferred natural linewidth 19.8(1) MHz. The dominant source of broadening is likely the laser linewidth which, if Lorentzian, would directly add to the 19.6 MHz natural linewidth. A laser linewidth of $\sim$0.5 MHz would not be surprising. We do not correct our theory for the relatively small laser linewidth, but leave it as a systematic error.

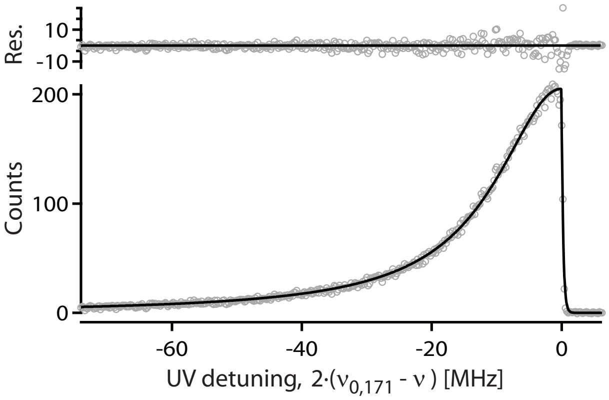

Figure 5.10: Scan of UV laser frequency to locate the resonance of a single trapped ^{171}Yb$^+$. The frequency-doubled laser is scanned with the fundamental locked to iodine by tuning the lock offset frequency ν relative to resonance $\nu_{0,171}$. Data shown is taken at $\delta_B/2\pi$=8.19 MHz, s_0=1.590(4), and θ_{BE}=57.5°. The line is a fit to a Lorentzian with exponential suppression above resonance. Residuals are shown in top panel. Fit parameters are a peak amplitude coefficient, lock offset on resonance $\nu_{0,171}$=10193.00(5) MHz and linewidth 24.6(2) MHz, where errors include sensitivity to initial guesses. The horizontal axis is recalculated using the fit value of $\nu_{0,171}$.

5.3.3 Polarization

In this section we study the polarization dependence of ion fluorescence for both $^{174}\mathrm{Yb}^{+}$ and $^{171}\mathrm{Yb}^{+}$. Measurements are approached differently for the two isotopes. For $^{174}\mathrm{Yb}^{+}$ the dependence of fluorescence on Zeeman splitting is very weak and the primary behavior expected from Eq.(2.31) is a washing out of the polarization dependence at higher laser powers due to saturation; therefore, we focus on measuring the polarization behavior as function of laser power.

For $^{171}\mathrm{Yb}^{+}$, the fluorescence signal strongly depends on the incident 369.5-nm laser's polarization. We take advantage of this sensitivity in our analysis to calibrate the laser polarization with respect to the magnetic field quantization direction as a function of bias coil current. The magnetic field direction changes with the current because of the presence of a residual $\sim$1G background magnetic field. Thus the polarization calibration's primary role is to correct for the magnetic field direction (to within directional symmetries and ambiguities).

Defining the UV laser's polarization to lie in the $x-z$ plane, the angle θ_{BE} between magnetic field and UV polarization can be expressed in terms of angular coordinates θ_B and ϕ_B of the magnetic field and the orientation θ_E of the laser's electric field as

$$\cos\theta_{BE} = \cos\theta_E \cos\theta_B + \sin\theta_E \sin\theta_B \sin\phi_B. \tag{5.3}$$

where the angle $\theta_E = 2\theta_{\frac{\lambda}{2}}$ is controlled by the half-wave plate orientation $\theta_{\lambda/2}$ as defined in Fig 5.1.

$^{174}\mathrm{Yb}^{+}$ Polarization

The polarization dependence of $^{174}\mathrm{Yb}^{+}$ is studied as a function of laser power for the reason described above. The data is susceptible to drifts in laser power. To suppress their effect, we follow a similar procedure to the linewidth analysis and record relatively rapid scans of laser power as a function of half-wave plate angle $\theta_{\lambda/2}$, and correct for slow drifts in laser power between scans.

The complete data set after background and power-drift correction is shown in Fig 5.11. The magnetic bias coil current is fixed at 2.505 A to provide a Zeeman shift of 11.41 MHz. The laser detuning is set to 8.4 MHz below resonance. The variation in fluorescence

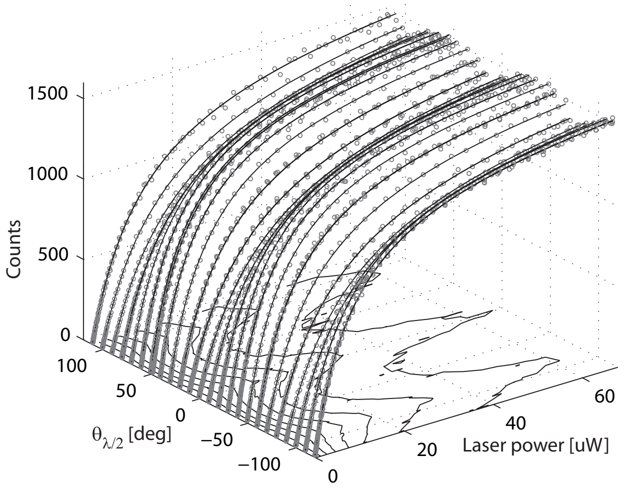

Figure 5.11: ^{174}Yb^{+} fluorescence as a function of 369.5-nm laser power and linear polarization controlled by half-wave plate angle $\theta_{\lambda/2}$. Zeeman shift is $\delta_B/2\pi = 11.4$ MHz ($I_{coil} = 2.5A$). The laser detuning is fixed at $\Delta/2\pi = -8.4$ MHz. The data consists of fifty four 68-point scans of laser power at half-wave plate positions over a 240-degree range. Fluorescence photons are counted by a PMT in a 10 ms integration time, averaged 10 times. Error bars suppressed for clarity. The lines are a global weighted fit to the theory in Eq.(2.31) with two free parameters, an amplitude coefficient 3660(2) related to photon collection efficiency, and saturation power $p_{sat} = 1.247(2)\mu$W. Other parameters are fixed including magnetic field angles as per calibration in Fig 5.13. The reduced χ^2 of 1.39 for 3672 total points, is sufficiently low to give reasonable parameter errors. See text and Fig 5.12 for a detailed quantitative assessment of this data and fit.

is very mild in comparison with $^{171}\text{Yb}^+$ (see below) since there are no polarization dark states. Errors are assumed to be the quadrature sum of Poissonian and 2% fractional noise before averaging. A global weighted fit to the repump-corrected $^{174}\text{Yb}^+$ theory Eqs.(2.33) and (2.31) has been made with two fit parameters, saturation power $1.247(2)$ μW and amplitude coefficient 3660(2). Other parameters in the fit are fixed including the magnetic field coordinates $\{\theta_B, \phi_B\}$ determined from $^{171}\text{Yb}^+$ polarization studies (see below) and repump factor $\xi = 0.1$. The reduced χ^2 of 1.39 for 3672 total points, is sufficiently low to give reasonable parameter errors on par with an unweighted fit. The large χ^2 is attributed to systematic error associated with the approximations made in Eq. (2.31) and excess instabilities and scan-to-scan drifts over the several hours of data collection. Regardless, Fig 5.11 shows that the fit is qualitatively good overall.

Figure 5.12 shows cross-sections of the polarization data at three different laser powers together with the global fit. Each cross-section has been scaled with respect to its peak value to emphasize how the polarization dependence saturates at high laser powers as expected. Unlike $^{171}\text{Yb}^+$, the fluorescence peaks at $\theta_{\lambda/2} = 48.6°$, equivalent to $\theta_{BE} = 0°$ where the effective linewidth (eqn 2.32) reaches a minimum.

To emphasize the analogy with an effective two-level system, we also demonstrate the polarization analysis in an alternative way using the same approach as for laser detuning dependence. The laser power scan at each polarization angle has been fit to the generalized saturation function (Eq.(5.1)) to extract the saturation derivative ds/dp as a function of $\theta_{\lambda/2}$. The fit values are plotted in Fig 5.12(c). An unweighted fit to Eq.(5.2) with a single fit parameter $p_{sat} = 1.247(3)$ μW matches the data well, giving reasonably random residuals. The value for p_{sat} matches the global fit as it should.

$^{171}\text{Yb}^+$ Polarization

We have studied the effect of UV polarization angle on $^{171}\text{Yb}^+$ fluorescence for four different bias coil currents {-0.343 A, 0.805 A, 1.695 A, 2.505 A} corresponding to Zeeman shifts $\delta_B/2\pi = \{0.95$ MHz, 4.67 MHz, 8.17 MHz, 11.39 MHz$\}$. The current -0.343 A is chosen to be close to the minimum Zeeman shift in Fig 5.7 to assess the background magnetic field orthogonal to the field provided by the bias coil. The detuning of the 369.5nm laser is chosen to be $\Delta/2\pi = -8.0$ MHz to maintain good laser cooling during data collection. In preparation for the measurements, the polarization of the 935.2-nm laser is adjusted

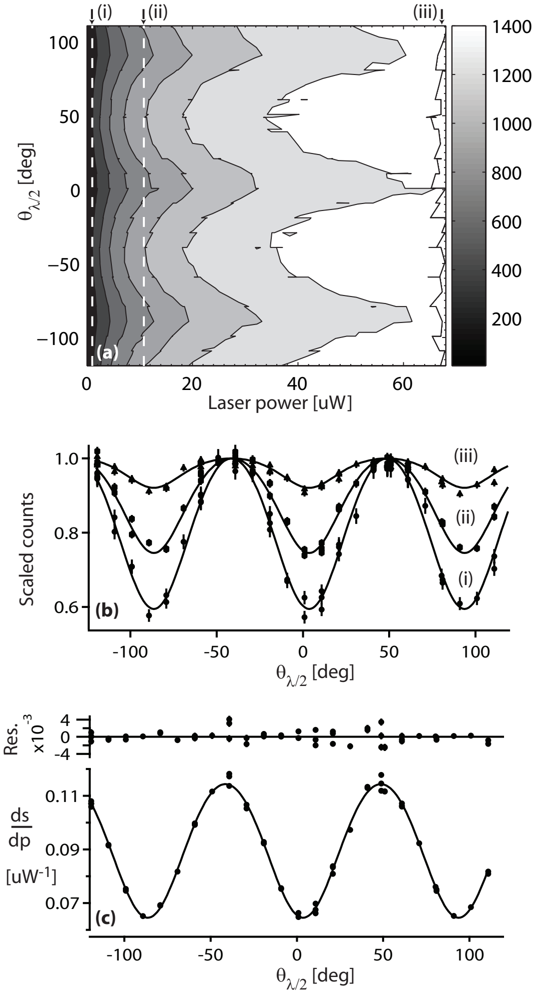

Figure 5.12: (a) Contour plot of data from Fig 5.11 showing location of data cross-sections in (b) at three laser powers (i) 1.1 μW, (ii) 10.5 μW, and (iii) 66.6 μW, corresponding to saturation parameters s_0 of 0.9, 8.4 and 53.4 respectively. (b) Cross-sections of fluorescence-count data as a function of half-wave plate angle $\theta_{\lambda/2}$. The count rates are normalized to the maximum value of the fit model. Solid lines are global fits from Fig 5.11. (c) Alternative analysis technique using separate weighted fits of each laser power scan in Fig 5.11 to a generalized saturation form to extract the amplitude coefficient and saturation-related parameter ds/dp. Fit values of ds/dp are plotted as a function of half-wave angle $\theta_{\lambda/2}$. The solid line is an unweighted fit to the ^{174}Yb^{+} theory given by in Eq.(2.31) plot.

to optimize the repump rate. The 935.2-nm laser power is also adjusted to be large enough to reduce sensitivity to beam pointing and detuning drifts, but not so large that the repump rate is significantly compromised by coherent population trapping. The UV fluorescence is not particularly sensitive to the repump parameters; therefore, the parameters are left fixed for all bias coil currents with the one exception being the value -0.343 A where the low Zeeman splitting of 0.95 MHz requires the 935.2 nm power to be reduced by a factor of roughly ten.

For each coil current, the polarization of the 369.5-nm laser is first set near to its optimal polarization angle, and the laser power is scanned to identify the value where the UV fluorescence peaks (Eq.(2.52)). The laser power is set to this value to reduce sensitivity to power drifts. Values used for -0.342 A, 0.805 A, 1.695 A, and 2.505 A are 1.4 μW, 6.5 μW, 10.1 μW, and 15.6 μW respectively. The polarization of the 369.5-nm laser is then varied by changing the half-wave plate angle $\theta_{\lambda/2}$. For each angle, PMT counts are recorded in three 1s intervals and averaged to obtain the fluorescence signal.

The fluorescence data for the four coil currents are corrected for background and plotted as a function of half-wave plate angle in Fig 5.13(a). The value of the peak fluorescence varies with Zeeman shift δ_B, which is due to coherent population trapping and will be discussed in the following section. That aside, all four plots show common features: a sharp minimum corresponding to $\theta_{BE} = 90^\circ$, and a broad minimum corresponding to $\theta_{BE} = 0^\circ$ or a π-polarized laser field. The fact that the sharp minima show good contrast indicates that the 369.5-nm laser has good linear polarization at the ion. The worst contrast occurs for the case of -0.343 A and is attributed to non-ideal wave-plate behavior near the minimum's location. The change in location of the sharp minimum for different bias coil currents is due to change in the magnetic field direction and is primarily sensitive to the coordinate θ_B.

For an arbitrary magnetic field direction, a sharp minimum will always exist that is fully dark in the ideal case since it is always possible to find a perpendicular laser polarization by rotating the half-wave plate. On the other hand, for the broad minimum, the minimum value of the fluorescence depends on how close the laser field comes to parallel polarization over the range of the half-wave plate, which in turn depends on the magnetic field orientation set by the coordinate ϕ_B. Clearly for all data sets, the broad minimum is quite low so the magnetic field is always approximately in the plane of rotation of the laser polarization vector, that is, $\phi_B \approx 90^\circ$. To fit the data we first parameterize the coil

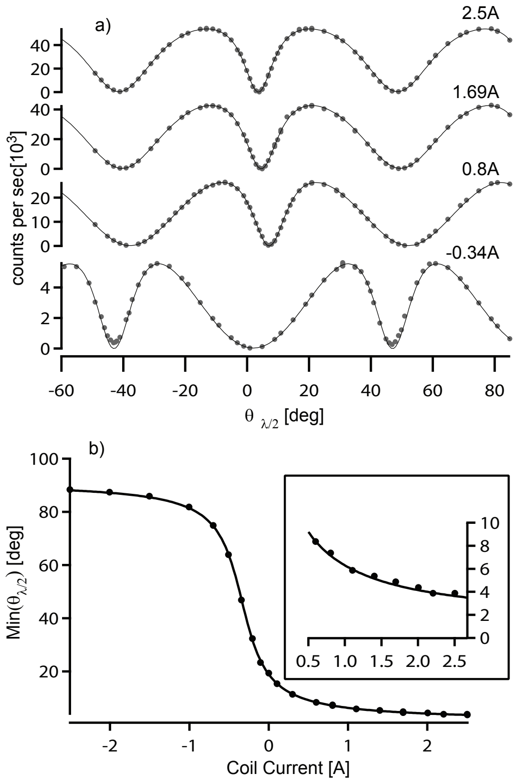

Figure 5.13: (a) Fluorescence counts for $^{171}\text{Yb}^+$ versus 369.5-nm half-wave plate angle $\theta_{\lambda/2}$ at four different magnetic bias coil currents {-0.343, 0.805, 1.695, 2.505}A. Lines show a global weighted fit. (b) Half-wave plate location of the sharp minimum as a function of magnetic bias coil current.

and static-background magnetic vectors in terms of magnitude constraints obtained from the magnetic field calibration and a minimum set of three spherical coordinates. We then perform a weighted global fit of data from all bias coil currents to Eqs.(2.33) and (2.50). The 935.2-nm repump factor is included in the fit function and is calculated as a function of magnetic field based on separate calibration measurements. The correction to the UV fluorescence rate is small, less than 2% maximum, for all magnetic fields considered.

Error bars used for the fit weighting are the quadrature sum of Poissonian error and 0.2° uncertainty in half-wave angle transferred to the vertical axis through slope interpolation. Nevertheless, the fluctuations in the data are completely dominated by various systematic errors. The fit is performed for a selected subset of 206 data points, about 2/3 of the total data, and leads to a reduced χ^2 of 0.97 for eight fit parameters. Excluded points include several outliers, points near the sharp minima of -0.343 A data, and data at angles larger than 35° where the half-wave plate shows a small but noticeable non-ideal behavior. Regardless, it is clear from Fig 5.13 that the fit is qualitatively quite good overall.

As mentioned above, the fit uses eight free fit parameters. The -8.0 MHz laser detuning and appropriate Zeeman shifts are held fixed in the fit. Besides the three angles used to parameterize the magnetic field direction, a small shift of 0.024(1) G accounts for drift in the magnitude of the background field parallel to the coil. Three amplitude coefficients of 367.7(2), 363.0(4) and 349.9(8) for the 1.7 A-2.5 A, 0.8 A and -0.34 A plots respectively allow for variability in the photon collection efficiency η. Finally, the fit imposes a single saturation power 1.262(8) μW for all data. The amplitude coefficients $\mathcal{A} = 10^{-3}\eta\gamma$ in terms of KiloHertz count rates convert to a collection efficiency $\eta \approx 2.9 \cdot 10^{-3}$. For typical currents {0.805 A, 1.695 A, 2.505 A} the *total* magnetic field's angular coordinates evaluated from the global fit are θ_B ={104.25(3)°, 99.15(4)°, 97.26(4)°} and ϕ_B ={87.26(7)°, 87.60(5)°, 87.73(5)°}. The ϕ_B values are ambiguous with $\pi - \phi_B$ but both give the same result for θ_{BE}.

To confirm the calibration of magnetic field direction obtained from the global fit, we have measured the half-wave plate position of the sharp minimum as a function of coil current. As shown in Fig 5.13(b), the prediction obtained from the global fit parameters matches the data very well over a wide range of bias coil current. Furthermore, we identify the range 0.8A-2.5A of magnetic bias coil current as a useful interval where the coil magnetic field dominates the background field and the total magnetic field's direction is reasonably constant (see Fig 5.13(b) inset). This range is the focus of the fluorescence studies as a function of laser power and magnetic field in the following section.

5.3.4 Laser power and magnetic field dependence

With magnetic field, laser detuning and laser polarization calibrated, it is now possible to assess the fluoresence as a function of laser power and magnetic Zeeman shift and compare the fluorescence behaviour of the two isotopes. The magnetic bias coil's current is limited to 0.8-2.5 A or equivalent Zeeman shift of 4.5-11.9 MHz, which provides a factor of 2.5

change in Zeeman shift but this range is small enough that the magnetic field direction remains nearly constant and orthogonal to the laser beam direction. Also the lower limit on Zeeman shift avoids excessive heating and "de-crystallization" of the ion in the trap over the full range of power considered for fluorescence.

^{174}Yb$^+$: Laser power and magnetic field dependence

We first consider power-saturation curves for ^{174}Yb$^+$ as a function of magnetic field strength. Figure 5.14 shows fluorescence versus power for three different Zeeman shifts $\{4.68\,$MHz$,8.19\,$MHz$,11.41\,$MHz$\}$ corresponding to bias coil currents $\{2.505\,$A$,1.695$A$,0.805$ A$\}$. The half-wave plate angle is set to $\theta_{\lambda/2} = 48.9°$, which is near the optimum polarization angle $\theta_{BE} = 0$ relative to magnetic field for all cases within the small residual variation in magnetic field direction and the 369.5-nm laser detuning is fixed at $\Delta/2\pi = -8.4$ MHz

The experimental sequence involves a 2.6 ms Doppler cooling interval followed by a 10 ms fluorescence photon counting interval. We keep all repump beams needed for ^{171}Yb$^+$ on to have similar powers for the two isotopes at the trap and to be able to compare saturation powers easily. The power of the UV laser is scanned and for each power value the fluorescence counts are averaged ten times for a net integration time of 100 ms.

Power scans, following power drift and background count correction as usual, are displayed in Fig 5.14 for all three Zeeman shifts. There is only a small difference between the data since the Zeeman dependence is rather weak. A weighted global fit of the repump-corrected ^{174}Yb$^+$ theory (Eqs. (2.31) and (2.33)) is applied to a set of five power scans including the three curves shown in Fig 5.14. A constant repump factor of $\xi = 0.1$ is used for all magnetic field values. As before, the error model used for weighting is the quadrature sum of Poissonian and 2% fractional noise before averaging. Residuals for the fit are shown in figure's top panel since the differences between curves are slight. An acceptable reduced χ^2 of 1.07 is obtained for this relatively small data set of 304 points and two fit parameters; however, the quality of fits to larger data sets is not as good, compromised by slow drifts of the photon collection efficiency and other effects. The amplitude coefficient from the fit is $\mathcal{A} = 3638(5)$, and the fit saturation power is $p_{sat} = 1.264(4)\mu$W. These values are similar to those obtained from other ^{174}Yb$^+$ data sets shown earlier.

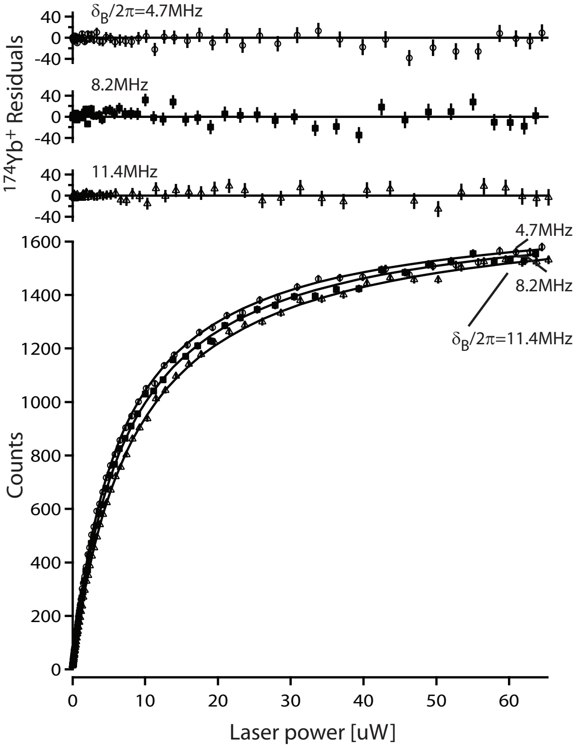

Figure 5.14: ^{174}Yb^{+} fluorescence versus UV laser power at three magnetic fields. Fluorescence counts are collected in 10 ms, averaged ten times. The three Zeeman shifts $\delta_B/2\pi = \{4.68, 8.19, 1.41\}$MHz as indicated correspond to bias coil currents{0.80, 1.69, 2.50}A. Fitted residuals for ^{174}Yb^{+} are shown in top panels.

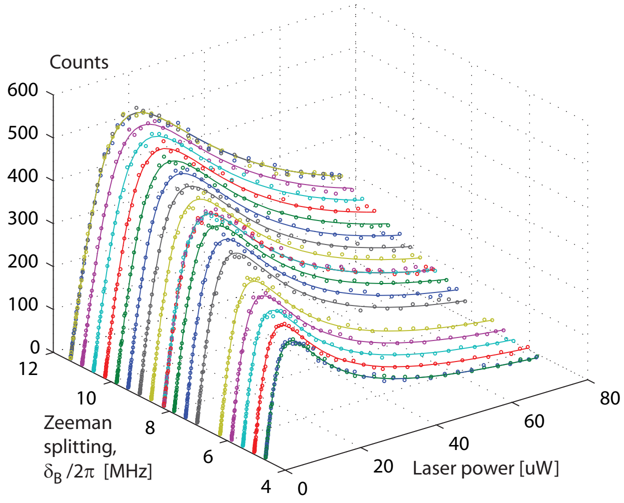

Figure 5.15: ^{171}Yb$^+$ fluorescence versus UV laser power and Zeeman shift δ_B. The data are taken with UV detuning -8.0 MHz and half-wave angle $\theta_{\lambda/2} = 20.9^\circ$, which is near-optimal linear polarization for all data. The lines are a single weighted global fit to all data. Error bars are suppressed for clarity. The reduced χ^2 is 1.05 for 1496 data points. Fit parameters are saturation power 1.226(1), and amplitude coefficient 3645(2). See text and Fig 5.16 for further quantitative assessment of fit.

^{171}Yb$^+$:Laser power and magnetic field dependence

We now consider the power dependence for for ^{171}Yb$^+$ fluorescence as a function of magnetic field. The laser detuning is -8.0 MHz and the half wave angle is set to $\theta_{\lambda/2} = 20.87^\circ$ which is near the peak of the fluorescence across the range of Zeeman splitting. The data collection sequence is the same as previous using a 10 ms fluorescence counting time, repeated and averaged ten times. All repump beams are prior-optimized and are active throughout. The Doppler cooling interval is at fixed power and the level is adjusted to inhibit de-crystallization of the trapped ion at the low end of magnetic fields considered. The ^{171}Yb$^+$ is very sensitive to magnetic field; hence, the scan of UV laser power from approximately 0-70 μW is performed at seventeen values of the Zeeman shift from 4.6 to 11.4 MHz. Each scan of 68 power values takes approximately 30 s while the complete data set is acquired over 1-2 hours. The counts are corrected for background and the laser power for each scan is corrected to account for slow drifts. Figure 5.15 shows the total data set, where the fluorescence reaches a maximum at a power value that increases with Zeeman shift δ_B. The fluorescence value at the peak also increases with increasing Zeeman shift.

Errors in the count values are determined from repeated measurements at $I_{coil} = 1.695$ A and are modeled as the quadrature sum of Poissonian and 2% fractional noise before averaging. A weighted global fit is performed with only two free fit parameters, an amplitude coefficient $\mathcal{A}$ and saturation power p_{sat}. Fixed parameters used are linewidth γ and detuning $\Delta/2\pi = -8.0$ MHz, while Zeeman splitting δ_B, polarization angle θ_{BE}, and the 935.2 nm repump correction are determined as a function of bias coil current from prior calibrations. The reduced χ^2 is an acceptable value of 1.05 for 1496 degrees of freedom (8% significance). The values for the fit parameters are $p_{sat} = 1.226(1)$ μW and amplitude coefficient $\mathcal{A} = 10^{-2} \cdot \eta\gamma = 3645(2)$, giving a photon collection efficiency $\eta = 2.9 \cdot 10^{-3}$.

Figure 5.15 provides an overall impression of the quality of the global fit. Figure 5.16 shows quantitative detail including data slices and global fit residuals at three example Zeeman shifts. The residuals exhibit some instabilities and discrete outliers which exceed Poissonian statistics. Nevertheless, *separate* fits of an individual laser scans are often moderately acceptable with Poissonian error bars alone (reduced χ^2 below 1.3 for 66 degrees of freedom). The global fits are more challenging due to scan-to-scan drifts particularly of the amplitude coefficient (from the ion drifting relative to PMT sensitive position) but agreement is quite good overall with residuals only 2-4% near the peak of fluorescence. Systematic errors due to detuning and linewidth have been explored qualitatively, and reasonable fits can still be obtained for small variations around the values used but with modified fit parameters.

On the contour plot of Fig 5.16(a), the approximate theoretical expression for Ω_{pk} (Eq.(2.52)) is seen to match well with the peak location across the magnetic field range considered. In Fig 5.16(b), the approximate theoretical expression for peak fluorescence value $Max(\mathcal{P}_{p0})$ (Eq.(2.53)) is also seen to match well with the data.

As a final comment, an additional technical issue arises when scanning the power of the 369.5-nm laser. Since the 369.5-nm hyperfine repump is obtained from a modulation sideband of the 369.5-nm laser, the repump power also varies as the laser power is scanned. We have separately verified that the repump sideband power can be reduced by more than

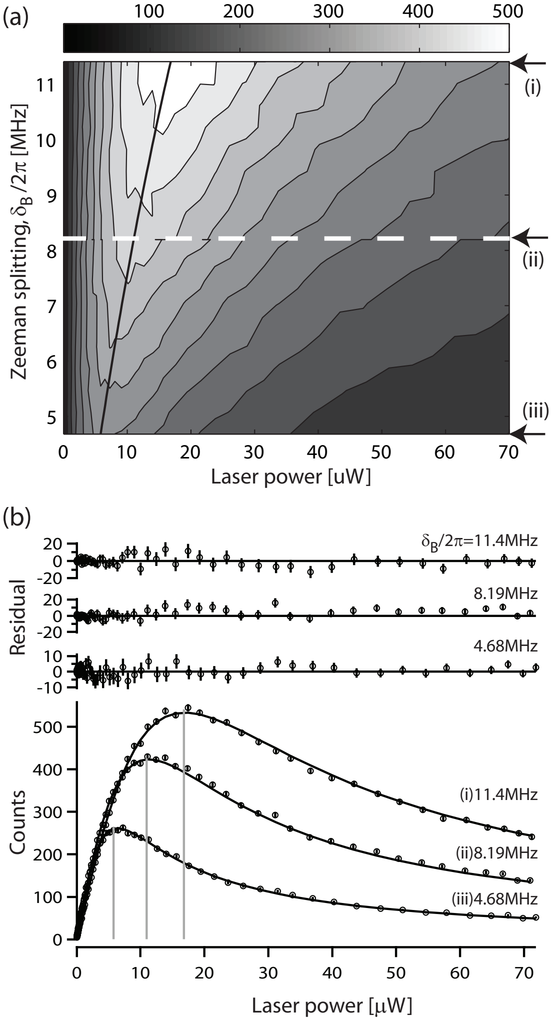

Figure 5.16: (a) Contour plot of ^{171}Yb^{+} fluorescence counts as a function of power and magnetic field (same data set as Fig 5.15). The contour scale is shown at top. The solid line is an approximate expression for the power at peak fluorescence (Eq.(2.52)). Arrows and horizontal dotted line indicate location of cross-sections shown in (b) at three different Zeeman splittings. (b) Counts in 10 ms as a function of laser power at three Zeeman splittings $\delta_B/2\pi = \{11.41, 8.19, 4.68\}$ MHz. Lines are a single weighted global fit as shown in Fig 5.15. Residuals shown for each Zeeman splitting. Drop lines indicate expected peak count rate and location according to Eqs. (2.52) and (2.53) and the values of the global fit parameters.

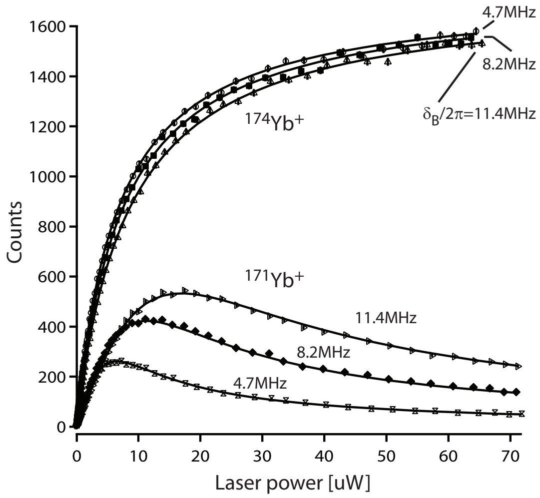

Figure 5.17: ^{174}Yb$^+$ and ^{171}Yb$^+$ fluorescence versus UV laser power at three magnetic fields. The three Zeeman shifts $\delta_B/2\pi = \{4.68, 8.19, 11.41\}$MHz as indicated correspond to bias coil currents{0.80, 1.69, 2.50} A. The three ^{174}Yb$^+$ scans are taken at near-optimal linear polarization $\theta_{\lambda/2} = 48.9°(\theta_{BE} = 2.8°)$ and with laser detuning -8.4 MHz. The three ^{171}Yb$^+$ scans are reproduced from Fig 5.16 and the three ^{174}Yb$^+$ scans are reproduced from Fig 5.14

a factor of two without observable effects on the fluorescence curves.

5.3.5 Comparison between ^{174}Yb$^+$ and ^{171}Yb$^+$ behaviours

For direct comparison, the ^{171}Yb$^+$ data from Fig 5.16(b) and the ^{174}Yb$^+$ data from Fig 5.14 are reproduced in Fig 5.17. It shows the overall reduction in fluorescence due to coherent population trapping. To be specific, the maximum scattering rate in Fig 5.17 reached by ^{174}Yb$^+$ at $\delta_B/2\pi = 8.19$ MHz corresponds to an excited state fraction of about $\mathcal{P}_p = 0.45$, or about 90% of the maximum 0.5. By contrast, at the same magnetic field value, the inferred excited state fraction of ^{171}Yb$^+$ is about 0.15 at its highest point. This is 60% of the absolute maximum 0.25 for ^{171}Yb$^+$, and about 0.3 lower than the value for ^{174}Yb$^+$.

A comparison of the three curves for ^{174}Yb$^+$ alone shows that the fluorescence lags slightly with increasing magnetic field as the effective linewidth is Zeeman broadened and the saturation power increased. All curves; however, approach the same saturated response at high laser powers. The same lag effect is also observable for $^{171}\mathrm{Yb}^+$ at low powers but the dominant observed effect is the increase in peak fluorescence with increasing magnetic field as optical pumping to the coherent dark state is countered.

Figure 5.17 also shows that the low power response of $^{171}\mathrm{Yb}^+$ is significantly slower (by a factor of $\sim$3) than that of $^{174}\mathrm{Yb}^+$. This is not a coherent population trapping effect but rather is due to the fact that the laser power for $^{171}\mathrm{Yb}^+$ must be split over three polarizations ($\theta_{BE} = 54.7^\circ$) to couple to all ground Zeeman states. On the other hand, π polarization alone ($\theta_{BE} = 0^\circ$) suffices in general to provide maximum fluorescence for $^{174}\mathrm{Yb}^+$.

The amplitude coefficients obtained from the $^{174}\mathrm{Yb}^+$ fit ($\mathcal{A} = 3638(5)$) and from the $^{171}\mathrm{Yb}^+$ fit in Fig 5.15 ($\mathcal{A} = 3645(2)$), are close as expected given that the value is a essentially a measurement of the photon collection efficiency of the imaging system. In fact, all the fit shown above yield quite close values for $\mathcal{A}$, and give a collection efficiency of about $\eta = 2.9 \cdot 10^{-3}$. Moreover, the saturation powers obtained from the $^{174}\mathrm{Yb}^+$ fit (1.264(4) μW) and the $^{171}\mathrm{Yb}^+$ fit (1.226(1) μW) are within 5%. There may be a slight high bias for $^{174}\mathrm{Yb}^+$ over all the data sets taken but the small level of disagreement is within the uncertainty of our day-to-day calibration of laser power and is comparable to variations in saturation power seen for a single isotope. Inclusion of the 935.2-nm repump effect was helpful to improve the agreement between isotopes since the effect acts asymmetrically. It reduces the saturation power and increases the amplitude coefficient by about 5% for $^{174}\mathrm{Yb}^+$ but has little effect on $^{171}\mathrm{Yb}^+$.

For a typical value of $p_{sat} = 1.26\mu\mathrm{W}$ and a measured beam waist diameter of 60 μm for the 369.5-nm laser, the saturation intensity is calculated to be 60 mW/cm^2. This value includes a correction of 28% to account for power lost to hyperfine repump sidebands and a correction of 8% to account for power lost from reflection at the uncoated entrance windows to the vacuum system. The value for saturation intensity matches quite well with the expected value of $I_{sat} = 51$ mW/cm^2 using the value of $\gamma/2\pi = 19.6$ MHz as usual. Note again that the values calculated here are defined for a two-level cycling transition and specifically exclude factors related to the multi-level transition.

Figure 5.17 summarizes the fluorescence results. The saturated count rate of $^{174}\mathrm{Yb}^+$ essentially provides a simple, direct measure of the imaging system's photon collection efficiency with minimal theoretical input and largely independent of laser parameters. The simple saturation form of the fluorescence also provides a basic calibration of the saturation intensity at the ion. These two experimental numbers together with the magnetic field and polarization calibration obtained from $^{171}\mathrm{Yb}^{+}$ behaviour are all the experimental inputs required to calculate the expected fluorescence count rate during detection of the hyperfine qubit in $^{171}\mathrm{Yb}^{+}$ ion.

5.4 Conclusion

In conclusion, we have measured the fluorescence of a single trapped $^{171}\mathrm{Yb}^{+}$ ion, which exhibits coherent population trapping in the transitions used for fluorescence detection and cooling, and we have verified a model for suppressing dark-state formation using a magnetic field of sufficient strength. We have also compared the $^{171}\mathrm{Yb}^{+}$ behaviour against a control isotope $^{174}\mathrm{Yb}^{+}$ with simple atomic structure for which coherent population trapping is absent on the primary transition. The fluorescence behavior of the two isotopes and comparison to analytical models provide a useful means to optimize experimental parameters in preparation for quantum information applications (see Ref. [18]). For $^{171}\mathrm{Yb}^{+}$ in particular, measurement of fluorescence as a function of laser power and the identification of the power for peak fluorescence are a critical calibration integrated into daily experiment routine. Although not discussed in this thesis, as an application of our fluorescence studies, we have already studied the fidelity of state-selective detection for the $^{171}\mathrm{Yb}^{+}$ hyperfine qubit [18]. We have obtained reasonable experimental agreement with theoretical models modified for experimental calibrations of parameters, and have obtained a single-shot qubit detection fidelity of 97%, limited currently by technical noise [18].

The next goal in the experiment is to implement stimulated two-photon Raman transitions to couple the spin and motional degrees of freedom of the trapped ion and to cool the ion to near its ground state of motion using Raman sideband cooling [60]. The fluorescence studies presented in this thesis will be useful for optimization of the Doppler cooling in preparation for Raman sideband cooling. A magnetic field of ~ 6 G ($\delta_B/2\pi = 8.2$ MHz), used in many of the results discussed above, is expected to provide a Doppler-cooling limit that is suitable to initiate Raman cooling in a slightly stronger trap than the one used in this thesis. As a final note, at a field of 6 G we have also measured qubit coherence for a single trapped ion that shows negligible decay out to 100 ms. Few-second coherence times have also been demonstrated for $^{171}\mathrm{Yb}^+$ in a similar setup [11]. These coherence times will be more than sufficient for initial quantum gate tests, including two-ion entanglement.

Bibliography

[1] Isaac Chuang Michael Nielsen. *Quantum computation and quantum information*. Cambridge University Press.

[2] R. P. Feynman. Simulating physics with computers. *Int. J. Th. Phys.*, 21(6/7):467–488, 1982.

[3] David. P. DiVincenzo. The physical implementation of quantum computation. *Fortschr. Phys*, 48:771, Apr 2000.

[4] N. Yu and L. Maleki. Lifetime measurements of the $4f^{14}$ 5d metastable states in single ytterbium ions. *Phys. Rev. A*, 61(2):022507, Jan 2000.

[5] Chr. Tamm, D. Engelke, and V. Bühner. Spectroscopy of the electric-quadrupole transition $^2S_{1/2}(F=1)$–$^2D_{3/2}(F=2)$ in trapped $^{171}Yb^+$. *Phys. Rev. A*, 61(5):053405, Apr 2000.

[6] T. Schneider, E. Peik, and Chr. Tamm. Sub-Hertz optical frequency comparisons between two trapped $^{171}Yb^+$ Ions. *Phys. Rev. Lett.*, 94(23):230801, Jun 2005.

[7] K. Hosaka, S. A. Webster, A. Stannard, B. R. Walton, H. S. Margolis, and P. Gill. Frequency measurement of the $^2S_{1/2}$–$^2F_{7/2}$ electric octupole transition in a single $^{171}Yb^+$ ion. *Phys. Rev. A*, 79(3):033403, Mar 2009.

[8] J. I. Cirac and P. Zoller. Quantum computations with cold trapped ions. *Phys. Rev. Lett.*, 74(20):4091–4094, May 1995.

[9] D. J. Wineland, C. Monroe, W. M. Itano, D. Leibfried, B. King, and D. M. Meekhof. Experimental issues in coherent quantum-state manipulation of trapped atomic ions. *J. Res. Nat. Inst. Stand. Tech*, 103(259), 1998.

[10] Chr. Balzer, A. Braun, T. Hannemann, Chr. Paape, M. Ettler, W. Neuhauser, and Chr. Wunderlich. Electrodynamically trapped Yb^{+} ions for quantum information processing. *Phys. Rev. A*, 73(4):041407, Apr 2006.

[11] S. Olmschenk, K. C. Younge, D. L. Moehring, D. N. Matsukevich, P. Maunz, and C. Monroe. Manipulation and detection of a trapped Yb^{+} hyperfine qubit. *Phys. Rev. A*, 76(5):052314, Nov 2007.

[12] Andrew T. Grier, Marko Cetina, Fedja Oručević, and Vladan Vuletić. Observation of cold collisions between trapped ions and trapped atoms. *Phys. Rev. Lett.*, 102(22):223201, Jun 2009.

[13] C. Zipkes, S. Palzer, C. Sias, and M. Kohl. A trapped single ion inside a Bose Einstein condensate. *Nature*, 79(388), Jan 2010.

[14] D. J. Wineland and Wayne M. Itano. Laser cooling of atoms. *Phys. Rev. A*, 20(4):1521–1540, Oct 1979.

[15] M. Acton, K. A. Brickman, P. C. Haljan, P. J. Lee, L. Deslauriers, and C. Mnoroe. Near-perfect simulation measurement of a qubit register. *Quantum Inf. Comp*, 6(6):465, 2006.

[16] B. B. Blinov, D. Leibfried, C. Monroe, and D.J. Wineland. Quantum computing with ion hyperfine qubits. *Quantum Inf.Proc*, 3:45, Nov 2004.

[17] D. J. Berkeland and M. G. Boshier. Destabilization of dark states and optical spectroscopy in zeeman-degenerate atomic systems. *Phys. Rev. A*, 65(3):033413, Feb 2002.

[18] S. Ejtemaee, R. Thomas, and P. C. Haljan. Optimization of Yb^{+} fluorescence and hyperfine-qubit detection. *Phys. Rev. A*, in press.

[19] C. Monroe, D. M. Meekhof, B. E. King, W. M. Itano, and D. J. Wineland. Demonstration of a fundamental quantum logic gate. *Phys. Rev. Lett.*, 75(25):4714–4717, Dec 1995.

[20] R. Blatt, H. Haffner, C. F. Ross, C. Becher, and F. Schmidt-Kaler. Ion trap quantum computing with Ca^+ ions. *Quantum Inf.Proc.*, 3:61, 2004.

[21] J. E. Sansonetti and W. C. Martin. *Handbook of basic atomic spectroscopic data*. National Institute of Standards and Technology, Gaithersburg, MD 20899.

[22] P. T. H. Fisk, M. J. Sellars, M. A. Lawn, and G. Coles. Accurate measurement of the $12.6GHz$ clock transition in trapped $^{171}\mathrm{Yb}^+$ ions. *IEEE Trans. Ultrason. Ferroelectr. Freq. Control*, 44:344.

[23] S. Olmschenk, D. Hayes, D. N. Matsukevich, P. Maunz, D. L. Moehring, K. C. Younge, and C. Monroe. Measurement of the lifetime of the $6p\,^2p^o_{1/2}$ level of Yb^+. *Phys. Rev. A*, 80(2):022502, Aug 2009.

[24] E. H. Pinnington, G. Rieger, and J. A. Kernahan. Beam-laser measurements of the lifetimes of the 6p levels in Yb II. *Phys. Rev. A*, 56(3):2421–2423, Sep 1997.

[25] R. W. Berends, E. H. Pinnington, B. Guo, and Q. Ji. Beam-laser lifetime measurements for four resonance levels of Yb II. *J. Phys. B: At. Mol. Opt. Phys.*, 26(20):L701, 1993.

[26] E. Biemont, J-F. Dutrieux, I. Martin, and P. Quinet. Lifetime calculations in Yb II. *J. Phys. B: At. Mol. Opt. Phys*, 31(15):3321, 1998.

[27] H. Lehmitz, J. Hattendorf-Ledwoch, R. Blatt, and H. Harde. Population trapping in excited Yb^+ ions. *Phys. Rev. Lett.*, 62(18):2108–2111, May 1989.

[28] A. Bauch, D. Schnier, and Chr. Tamm. Collisional population trapping and optical deexcitation of ytterbium ions in a radiofrequency trap. *J. Mod. Opt.*, 39(2):0950–0340, Aug 1992.

[29] M. M. Schauer, J. R. Danielson, A.-T. Nguyen, L.-B. Wang, X. Zhao, and J. R. Torgerson. Collisional population transfer in trapped Yb^+ ions. *Phys. Rev. A*, 79(6):062705, Jun 2009.

[30] E. Arimondo and G. Orriols. Nonabsorbing atomic coherences by coherent two-photon transitions in a three-level optical pumping. *Lettere Al Nuovo Cimento*, 17:333–338, 1976.

[31] H. R. Gray, R. M. Whitley, and C. R. Stroud. Coherent trapping of atomic populations. *Opt. Lett*, 3(6):218, Dec 1978.

[32] K.-J. Boller, A. Imamoglu, and S. E. Harris. Observation of electromagnetically induced transparency. *Phys. Rev. Lett.*, 66(20):2593–2596, May 1991.

[33] A. Aspect, E. Arimondo, R. Kaiser, N. Vansteenkiste, and C. Cohen-Tannoudji. Laser cooling below the one-photon recoil energy by velocity-selective coherent population trapping. *Phys. Rev. Lett.*, 61(7):826–829, Aug 1988.

[34] C. F. Roos, D. Leibfried, A. Mundt, F. Schmidt-Kaler, J. Eschner, and R. Blatt. Experimental demonstration of ground state laser cooling with electromagnetically induced transparency. *Phys. Rev. Lett.*, 85(26):5547–5550, Dec 2000.

[35] G. P. Barwood, P. Gill, G. Huang, H. A. Klein, and W. R. C. Rowley. Sub-kHz "clock" transition linewidths in a cold trapped $^{88}\mathrm{Sr}^+$ ion in low magnetic fields using 1092-nm polarisation switching. *Optics Communications*, 151(1-3):50 – 55, 1998.

[36] D. J. Berkeland, J. D. Miller, J. C. Bergquist, W. M. Itano, and D. J. Wineland. Laser-cooled mercury ion frequency standard. *Phys. Rev. Lett.*, 80(10):2089–2092, Mar 1998.

[37] G. Janik, W. Nagourney, and H. Dehmelt. Doppler-free optical spectroscopy on the Ba+ mono-ion oscillator. *J. Opt. Soc. Am. B*, 2(8):1251–1257, 1985.

[38] A. A. Madej and J. D. Sankey. Single, trapped Sr^+ atom: laser cooling and quantum jumps by means of the $4d^2\mathrm{D}_{5/2}$ –$5s^2\mathrm{S}_{1/2}$ transition. *Opt. Lett.*, 15(11):634–635, 1990.

[39] G. P. Barwood, P. Gill, G. Huang, H. A. Klein, and W. R. C. Rowley. Studies of trapped strontium ions in low magnetic fields. *Appl. Phys. B*, 61(4):385–390, Oct 1995.

[40] J. J Sakurai. *Modern Quantum Mechanics*. Addison-Wesley, 2005.

[41] Harold J. Metcalf and Peter van der Straten. *Laser cooling and trapping*. Springer, 1999.

[42] S. Chang and V. Minogin. Density-matrix approach to dynamics of multilevel atoms in laser fields. *Physics Reports*, 365:65, 2002.

[43] S. G Rautian and A. M Shalagin. *Kinetic problems of non-linear spectroscopy*. North-Holland.

[44] D. J Griffiths. *Introduction to Electrodynamics*. Prentice Hall, 3rd edition, 1999.

[45] R. P Ghosh. *Ion Traps*. Oxford Science, 1995.

[46] M. G. Raizen, J. M. Gilligan, J. C. Bergquist, W. M. Itano, and D. J. Wineland. Ionic crystals in a linear Paul trap. *Phys. Rev. A*, 45(9):6493–6501, May 1992.

[47] D. J. Berklnad, J. D. Miller, J. C. Bergquist, W. M. Itano, and D. J. Wineland. Minimization of ion micromotion in a Paul trap. *J. Appl. Phys*, 83(10):5025, May 1998.

[48] Kazuhiko Sugiyama and Jun Yoda. Production of YbH^+ by chemical reaction of Yb^+ in excited states with H_2 gas. *Phys. Rev. A*, 55(1):R10–R13, Jan 1997.

[49] D. M. Lucas, A. Ramos, J. P. Home, M. J. McDonnell, S. Nakayama, J.-P. Stacey, S. C. Webster, D. N. Stacey, and A. M. Steane. Isotope-selective photoionization for calcium ion trapping. *Phys. Rev. A*, 69(1):012711, Jan 2004.

[50] S. Gulde, D. Rotter, P. Barton, F. Schmidt-Kaler, R. Blatt, and W. Hogervorst. Simple and efficient photo-ionization loading of ions for precision ion-trapping experiments. *Appl. Phys. B: Lasers Opt*, 73(18):861, 2001.

[51] L. Deslauriers, M. Acton, B. B. Blinov, K.-A. Brickman, P. C. Haljan, W. K. Hensinger, D. Hucul, S. Katnik, R. N. Kohn, P. J. Lee, M. J. Madsen, P. Maunz, S. Olmschenk, D. L. Moehring, D. Stick, J. Sterk, M. Yeo, K. C. Younge, and C. Monroe. Efficient photoionization loading of trapped ions with ultrafast pulses. *Phys. Rev. A*, 74(6):063421, Dec 2006.

[52] S. Gerstenkorn, J. Verges, and J. Chevillard. Atlas du spectre d'absorption de la molecule d'iode,11000-14000cm^{-1}. *(Laboratoire Aime-Cotton, CNRS II, 91405 Orsay, France, 1982)*, 1982.

[53] P. Dube' and M. Trinczek. Hyperfine-structure splittings and absorption strengths of molecular-iodine transitions near the trapping frequencies of francium. *J. Opt. Soc. Am. B*, 21:1113, 2004.

[54] J. J. Snyder, R. K. Raj, D. Bloch, and M. Ducloy. High sensitivity nonlinear spectroscopy using a frequency -offset pump. *Opt. Lett*, 5:163, 2004.

[55] Anthony E.Siegman. *Lasers*. University Science Books, Sausalito, California, University Science Books,2006.

[56] S. Moriwaki, H. Sakaida, T. Yuzawa, and N. Mio. Measurement of the residual birefringence of interferential mirrors using Fabry-Perot cavity. *Appl. Phys. B*, 65:347.

[57] E. Riedle, S. H. Ashworth, J.T. Farrell, and D. J. Nesbitt. Stabilization and precise calibration of a continuous-wave difference frequency spectrometer by use of a simple transfer cavity. *Rev. Sci. Instrum*, 65(1):42, Jan 1994.

[58] http://emtoolbox.nist.gov/wavelength/ciddor.asp.

[59] D. L Moehring. *Remote entanglement of trapped atomic ions*. PhD thesis, 2007.

[60] D. Leibfried, R. Blatt, C. Monroe, and Wineland. D. Quantum dynamics of single trapped ions. *Rev. Mod. Phys.*, 75:281, 2003.

[61] W. Nagourney, G. Janik, and H. Dehmelt. Linewidth of single laser-cooled ^{24}Mg^{+} ion in radiofrequency trap. *Proc. Natl. Acad. Sci. U.S.A.*, 80(2):643–646, 1983.

[62] The lock offset frequency includes a 80MHz/2 shift from the saturation setup. The wavelength quoted is corrected for an 80MHz AOM shift in the UV.

[63] D. J. Larson, J. C. Bergquist, J. J. Bollinger, Wayne M. Itano, and D. J. Wineland. Sympathetic cooling of trapped ions: A laser-cooled two-species nonneutral ion plasma. *Phys. Rev. Lett.*, 57(1):70–73, Jul 1986.

[64] B. B. Blinov, L. Deslauriers, P. Lee, M. J. Madsen, R. Miller, and C. Monroe. Sympathetic cooling of trapped Cd^+ isotopes. *Phys. Rev. A*, 65(4):040304, Apr 2002.

[65] Th. Haslwanter, H. Ritsch, J. Cooper, and P. Zoller. Laser-noise-induced population fluctuations in two- and three-level systems. *Phys. Rev. A*, 38(11):5652–5659, Dec 1988.